Examination of Physiology and Pathophysiology of the Human Visual Cortex using Functional Magnetic Resonance Imaging

Dissertation

zur Erlangung des akademischen Grades
doctor rerum naturalium
(Dr. rer. nat.)

genehmigt durch die Fakultät für Naturwissenschaften der
Otto-von-Guericke-Universität Magdeburg

von Dipl.-Neurowiss. Falko R. Kaule

geb. am 1.3.1985 in Berlin

Gutachter: apl. Prof. Dr. rer. nat. Michael Hoffmann
Prof. Dr. rer. nat. Mark Greenlee

eingereicht am: 14. März 2017
verteidigt am: 7. November 2017

Contents

Chapter 1

Motivation - The What and the Why

1.1   Major Questions

The human visual cortex is governed by a number of organization principles, *i.e.*, dominance of contralateral visual field representations and retinotopic representation. (Congenital) Deviations from this scheme challenge these organization principles and can therefore serve as model to understand developmental and plastic mechanisms in the human brain. To evaluate cortical plasticity in humans, I quantified adaptation in the visual cortex to innate misrouting of the optic nerves. Additionally I improved a method for objective plasticity evaluation, "hyperalignment". Therefore two major questions arise:

1. How is congenital chiasma malformation influencing the visual field representation in the visual cortex? Investigating visual system alterations is hampered by their impact on visual function which has an impact on controlled visual stimulation. Thus, what kind of method would be most suitable to gather insights in cortical adaptations in vivo? Ideally it should be suitable to use with patients. Which leads to the following question:

2. How can these methods be improved to deal with the special circumstances of the examined participant groups (*i.e.*, low visual acuity, nystagmus, and visual field defects)? It would be useful to have an easier method to acquire the cortical visual field representations that is not impaired by the changes of the visual system: A method not demanding high attention, good fixation abilities, nor good visual acuity would be ideal.

The method of choice would be a non-visual stimulus, or at very least an interesting and easy-to-follow visual stimulus, that is as well usable by elderly or visual impaired. All this could be done with the help of an audio-movie [Hanke et al., 2014] and Hyperalignment [Haxby, 2012].

To answer all of these questions, the following sections will initially provide an overview about the visual system (see 2.1.1, p.3). This way it is possible to understand which changes in the visual system lead to which kind of cortical differences/adaptations. Introducing the two different kind of misrouting examined in this thesis, namely Albinism and Achiasma (see 2.1.2.3, p.6), the reader will get an brief overview about the style of misrouting itself. The focus will be on enhanced and reduced misrouting in Albinism and Achiasma, respectively. Insights about the basic consequences to the visual cortex will be given, too.

1.2   The Methods: Retinotopic Mapping & Hyperalignment

Mainly two methods have been used for this thesis. These two, Traveling wave based retinotopic mapping [Wandell et al., 2007; Sereno et al., 1995; DeYoe et al., 1996; Engel et al., 1997] and "whole brain activation by complex stimuli" [Hanke et al., 2014] are described in Section *Background* (see 3.2, p.33). Looking at the two different conditions of optic nerve routing the question arises how the visual input, thus the cortical representation of the hemifields, changes/adopts - what stays similar to controls, and what changes? To investigate such changes a non-invasive method with proper spatial resolution is needed. The examined participant should not be affected at all, too. Because of that the first choice of mapping the retinotopic representation is traveling wave based retinotopic mapping via fMRI (see 2.1.5, p.13). Which gives a reliable map of retinal representations. To circumvent the special circumstances measuring participants with visual impairment a kind of functional Alignment, namely "Hyperalignment" Haxby et al. [2011] is introduced and the improvement undertaken by me using the Connectome-Hyperalignment approach is shown.

Hyperalignment allows projecting datasets from one subject to another, as long as one similar/same dataset is present for both subjects. This makes it possible to project the retinotopic maps of one healthy subject onto another subject as a form of map transfer. The second subject, *e.g.*, . patient, does not need to undergo the mapping procedure.

Chapter 2

Visual Pathway Abnormality

2.1 Background

2.1.1 The Visual System in General

The visual system is easy to stimulate under controlled conditions and has a predictable activity regarding retinal representations in the (primary) visual cortex. This makes it possible to compare different retinal representations under different conditions of input. Since it is relatively easy to compare expected- with elicited-output, it can be used to validate more complex methods such as Hyperalignment (further details in the later *Functional Alignment: Hyperalignment* (see 3, p.31)).
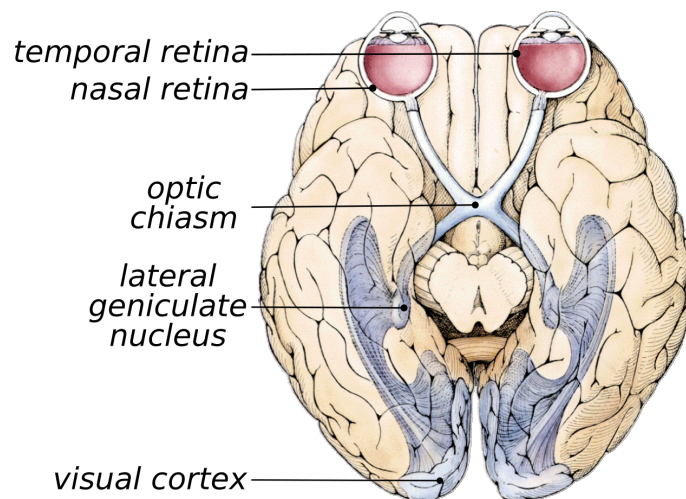
Figure 2.1: Scheme of visual stream: From the eye to the visual cortex (adapted from Hubel [1989])

As light enters the eye, it activates the photo receptor cells in the retina. The activation of the photo receptor cells is mediated through the bipolar cells to the retinal ganglion cells. The retinal ganglion cells axons project the activation via the optic nerve to the Lateral Geniculate Nucleus (LGN). Before terminating at the LGN, the optic nerve crosses partially at the Optic Chiasm (OC) to the contralateral hemisphere (see Figure 2.1).

The OC optic nerve fibers projecting information from the nasal retina do not cross and therefore get projected ipsilaterally. Fibers projecting from the nasal retina cross to the contralateral hemisphere (see Figure *Functional Alignment: Hyperalignment* (see 3, p.31)).

2.1.2   Visual Areas

In many visual areas, the visual field is represented retinotopically. This means that places which are next to each other in the visual field, and therefore on the retina, are also represented next to each other on the visual cortex, especially the primary visual cortex (V1-3). As higher processing steps include wider Receptive Fields (RF), the retinotopic representation is smeared and appears less distinguished [Wandell and Winawer, 2015]. Each visual area represents a complete visual field and its boundaries are based on the polar angle representations of the meridians and eccentricities. Higher visual areas demand bigger receptive fields and as a result of this, visual field positions are less distinguishable. Visual areas are quite consistent across control subjects (V1-3: Dougherty et al. [2003]; Benson et al. [2014]) and can be predicted from anatomy as well [Benson et al., 2014].

2.1.2.1   Definition of Visual Areas

"Because maps are ubiquitous in the human brain, they appear as a requirement for normal perception and behavior" [Hoffmann and Dumoulin, 2015]. Visual areas can be defined anatomically by taking the anatomical landmarks to define the borders [Benson et al., 2012, 2014], or they can be defined functionally to obtain the representation of the vertical and horizontal meridians to delineate the visual area boundaries [Wandell and Winawer, 2015; Sereno et al., 1995; Engel et al., 1997]. The boundaries of visual areas are defined by the edges of the visual field representations. One cornerstone is the expansion along the eccentricity, meaning how far from the fovea one object is represented in the cortex. The second limit is given by the polar angle representations. It describes in which plane the object is represented, meaning more at the lower vertical meridian, the horizontal meridian or more at the upper vertical meridian. In general, the reversal of polar angle representation indicates the beginning of another visual area. Functional definition can be done via different kinds of retinotopic mapping *i.e.*, traveling wave based [Engel et al., 1997], multi-focal stimulus based [Henriksson et al., 2012], population Receptive Field (pRF) based [Dumoulin and Wandell, 2008], or combinations with attention [Arcaro et al., 2009; Bressler and Silver, 2010; Sheremata and Silver, 2015] and movement [Sheremata and Silver, 2015]. It is important to keep in mind that there are different kind of mapping methods, as stated in Wang et al. [2014]:

"For example, although all retinotopically defined regions reflect a similar underlying spatial organization, different regions may be best-identified using different stimuli and experiential parameters. Early visual areas are typically mapped with passively viewed "wedge and ring"stimuli [Sereno et al., 1995; DeYoe et al., 1996; Engel et al., 1997] with relatively short stimulus cycles of 24 or 32 dimensions (the length between stimulus position repetitions) and relatively thick wedges (90°), and can be identified in a short scan session. Higher order regions with larger receptive fields, such as TO1/2, VO1/2, and PHC1/2, are better identified using a longer stimulus cycle (40 or 64 s), thinner wedges (45°), and typically require a longer scan session [Wandell et al., 2007; Kolster et al., 2010]. Topographic regions of the parietal and frontal cortices are often identified using a completely different memory-guided saccade mapping procedure [Sereno et al., 2001], which incorporates covert attention, spatial memory, and overt saccades in a traveling-wave paradigm. [..] Finally, many visual areas appear to benefit from combining aspects of the two methods by employing a concurrent covert attention-monitoring task with a traditional wedge stimulus [Arcaro et al., 2009; Bressler and Silver, 2010]. In total, identifying all of the currently known topographic regions of the human visual system requires multiple scanning sessions. Given the expense and availability of fMRI, this is not always practical."

There are likewise approaches of resting state mapping [Raemaekers et al., 2014; Arcaro et al., 2015] and mapping via activation during complex stimulation [Arcaro et al., 2015], but these cannot, at present, fully replace the original retinotopic mapping approaches. Why this is the case will be explained in Chapter *Functional Alignment: Hyperalignment* (see 3, p.31).

2.1.2.2 Ventral Areas

The ventral visual pathway is an integral part of the networks concerned with the processing of object quality [Kravitz et al., 2013]. For a substantial portion of this highly specialized part of the human visual system, retinotopic representations of the contralateral visual hemifield have been demonstrated [Arcaro et al., 2009; Brewer et al., 2005], similar to those of other visual processing stages [Wandell et al., 2007]. Specifically, two adjacent visual field map clusters anterior to Visual Area 4 (V4) were identified that are involved in color, scene, and/or object processing [Arcaro et al., 2009; Brewer et al., 2005]. These reside in the Ventral Occipital (VO) and Para-Hippocampal Cortex (PHC). Each of these clusters comprises two retinotopic maps, *i.e.*, the visual areas VO1 and VO2, and PHC1 and PHC2 [Arcaro et al., 2009].

Retinotopic vs. Functional Definition

The ventral visual cortex has been subdivided into the areas of VO1&2 [Brewer et al., 2005] and PHC1&2[Arcaro et al., 2009] by retinotopic mapping. Because of this it is based

on polar angle and eccentricity — and therefore visual field representations. In the same region Fusiform Face Area (FFA) [Kanwisher et al., 1997], Parahippocampal Place Area (PPA) [Epstein and Kanwisher, 1998], Extrastriate Body Area (EBA) [Downing et al., 2001], and Fusiform Body Area (FBA) [Peelen and Downing, 2005] are localized . These areas are defined by their functional representation of faces, bodies, or places, and not by their visual field representations. The focus in this thesis will be on the retinotopy of the visual areas and not on their object preference. This gives the advantage of being able to use one stimulus to map several areas instead of having multiple, different localizers for all known kinds of functional areas: *e.g.*, different object categories, movement, colors. As a result it is important to mention that mapping based on "simple", traveling wave based retinotopic mapping is not well suited for the mapping of higher areas. The receptive fields become too big, and are hence smeared, to depict specific boarders. Therefore functional localizers are used to give the area outlines based on the template preference rather than on retinotopy.

2.1.2.3   Misrouting

Usually the temporal retina projects to the ipsilateral hemisphere and the nasal retina projects to the contralateral hemisphere. This way each hemisphere gets the information of both hemifields with viewing angles from both eyes. The result is the visual field representation in the visual cortex, whereas the left hemifield is represented on the right hemisphere and vice versa. Both hemifields are merged using the information from both eyes: the ipsilateral temporal retina and the contralateral nasal retina.

The two atypical conditions of optic nerve crossing investigated in this thesis are albinism and achiasma. In the examined participant groups (albinism and achiasma), the projection pattern from the eyes to the LGN is different and leads to different projection patterns to the visual cortex. By comparing the visual field representations to the controls, it is possible to quantify the degree of misrouting and pinpoint it to specific retinal areas. The focus here is the visual cortex because it is well examined, even if other parts of the visual system are affected by misrouting of the optic nerves, too.

The misrouting in albinism and achiasma leads to superimposed instead of opposed hemifield maps. For achiasma, the receptive field sizes stay normal as do the bilateral receptive field along the vertical meridian. The same is expected for albinism, but there are no data available. Misrouting can also be found in congenital stationary night blindness and foveal hypoplasia, optic nerve decaussation defects, and anterior segment dysgenesis (FHONDA: Al-Araimi et al. [2013]; Creel et al. [1995]). As hemifield dominance columns and ocular dominance columns follow the same pattern, there is no large-scale reorganization in geniculo-striate projection by changed genicular input as with albinism or achiasma.
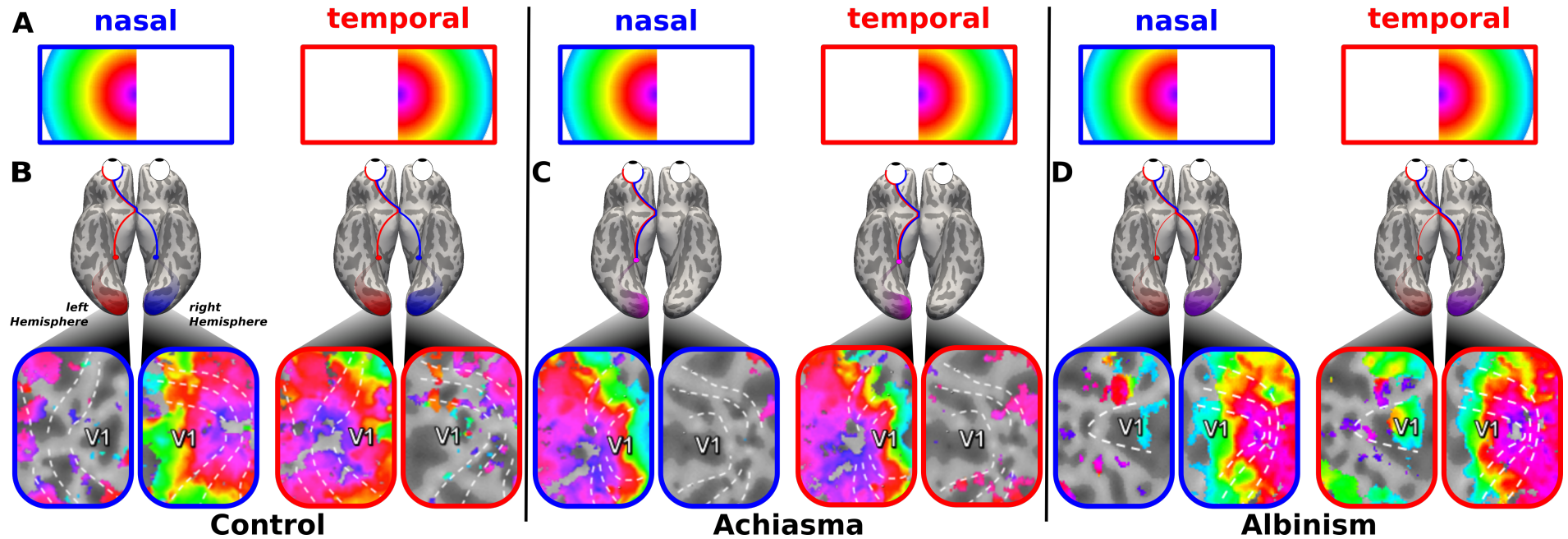
Figure 2.2: Visual pathway abnormalities in albinism or achiasmia. (A) Schematic display of visual hemifield representations, by viewing with the left eye. The colorcoded visual field positions depict the eccentric areas of the visual field. They show the local representation of the hemifields on the hemispheres. Visual field representations are shown on a flattened part of the primary visual cortex V1. The left and right hemifield, here nasal and temporal retina, are hemmed blue and red, respectively. Typically the visual hemifield is represented at the contralateral hemisphere by projecting from the nasal retina to the contralateral hemisphere, and from the ipsilateral retina to the contralateral hemisphere, as seen for Controls (B). As a result the hemifield representation in the blue and red boxes show their full color spectrum only on the contralateral hemisphere, *i.e.*, left hemifield (here nasal retina) at the right hemisphere and right hemifield (here temporal retina) at the left hemisphere. The fusion of the input of the ipsilateral temporal and the contralateral nasal retina leads to a binocular stereotopic visual impression ∕ vision. (C) The hemifields in Achiasma are represented on the hemisphere ipsilateral to the viewing eye. Both retinae of one eye project to the ipsilateral hemisphere. Thereby both hemifields are represented ipsilaterally to the stimulated eye, leading to a superposition of the left and right hemifield on the ipsilateral hemisphere. (D) The hemifields in Albinism are mostly represented on the hemisphere contralateral to the viewing eye. Enhanced crossing of the optic nerve leads to a atypical projection of the temporal retina to the contralateral hemisphere, resulting in a atypical contralateral representation of the temporal retina with only some residual representation on the ipsilateral hemisphere. Additionally, the nasal retina projects typically to the contralateral hemisphere. This leads to a superposition of the left and right hemifield in this contralateral hemisphere, here shown by representation of the left and right hemifield at the right hemisphere while stimulating the left eye. (data adapted from **Kaule** et al. [2014]; Hoffmann et al. [2012], for achiasma data is flipped left-right to fit the scheme layout)

2.1.3   The Visual System in Albinism and Achiasma

As depicted in Figure 2.2: While the temporal and nasal retinae normally project to the ipsilateral and contralateral hemisphere, respectively, this projection scheme is altered in conditions with congenital malformations of the OC as seen in albinism and achiasma. In albinism, part of the projection of the temporal retina crosses the midline separating the two hemispheres and as a result projects abnormally to the contralateral hemisphere [Apkarian et al., 1983; Hoffmann et al., 2005; Von Dem Hagen et al., 2007]. In achiasma, the nasal retina fails to cross the midline and thus projects to the ipsilateral hemisphere [Apkarian et al., 1994, 1995; Prakash et al., 2010]. In both conditions, the primary visual cortex (V1) receives substantial abnormal input from the ipsilateral visual field in addition to the normal input from the contralateral visual field. Specifically, a retinotopic map of the ipsilateral visual field is overlaid onto the normal map of the contralateral visual field [Davies-Thompson et al., 2013; Hoffmann et al., 2003, 2012; Muckli et al., 2009]. This organization of the primary visual cortex is likely to due to unaltered geniculo-striate connections, *i.e.*, connections that follow the projection scheme also observed in participants with a normal OC [Guillery, 1986].

Retinotopic maps in the visual cortex are influenced by differences in the visual stream. Changes of the OC, as happen in albinism and achiasmia, influence the representation pattern and implicate that the degree of misrouting can be quantified by the degree of changes. Changes in representation of the visual field in the visual cortex can be taken as indicators for misrouting and changed projection pattern.

2.1.3.1   Albinism

Albinism leads to an enhanced crossing of optic nerve fibers at the OC, and achiasmia leads to a reduced or non crossing. "Thus, the optic chiasm is a key connection between the eye and brain and essential for preservation of visual field maps. Acquired damage causes visual field loss in affected areas" [Hoffmann and Dumoulin, 2015]. Congenital changes of OC mostly do not lead to visual field defects but changes in visual field maps, as interleaved/non-interleaved patterns. Topographical visual field representations rely on "interplay of preprogrammed mechanisms, for example, chemoaffinity gradients, molecular midline markers, spontaneous neural activity waves, and experience dependent mechanism during early development" [Hoffmann and Dumoulin, 2015]. Sizable reorganization are questioned but fine-scale reorganization of response properties of primary visual cortex seem to be induces as receptive field properties as position, size, and response amplitude change.

Albinism is characterized primary by low vision due to foveal underdevelopment, fovea hypoplasia, or the less pronounced development of the foveal pit. According Hoffmann and Dumoulin [2015]: The prevalence is 1:17,000. Between 2 and 15° of the temporal retina project atypically to the contralateral hemisphere. Also, there are "small subtle changes in cortical thickness and convolution of the visual cortex" in albinism [Bridge et al., 2014];

it is likely that this is due to fovea hypoplasia and reduced visual acuity. Normally 55% of the optic nerve fibers cross, but for albinism maximally 75-88% cross. The amount of crossing depends on the degree of albinism [Levin and Stroh, 2011]. The enhanced crossing of the temporal retina especially leads to an overlay of both hemifield representations in the visual cortex [Hoffmann et al., 2003; Hoffmann and Dumoulin, 2015]. According to Von Dem Hagen et al. [2007], neither the pigmentation level nor the extent of the misrouting are predictors for the visual acuity or nystagmus amplitude; but nystagmus and visual acuity correlate significantly. The lateralization of the retinal projections is normally tested by Visual Evoked Potentials (VEP) [Apkarian et al., 1983], but it can as well be done using fMRI with a hemifield stimulus [von dem Hagen et al., 2008]. This way it is possible to get the exact locations which a represented atypically via localization of retinal representations [Hoffmann et al., 2003]. The visual field representation in albinism and achiasma can be organized in mainly three different ways, as reviewed in Guillery [1986]; Hoffmann et al. [2003, 2012] and summarized lately in Hoffmann and Dumoulin [2015] (see also Figure 2.3):

> "**Interleaved Representation** (formerly True Albino Pattern): V1 receives input from opposing visual hemifields, which is organized as interleaved maps from the contralateral and ipsilateral visual hemifield. This pattern is expected, if the LGN projects, despite abnormal input due to enhanced or reduced optic nerve crossing at the chiasm, in an unaltered manner to V1. It therefore indicates conservative geniculostriate connections. Intracortical plasticity is required to resolve a potential sensory conflict, that is, crosstalk of information across opposing hemifields.
>
> **Interleaved Suppressed Representation** (formerly Midwestern Pattern): geniculostriate projection as for the 'Interleaved Representation', but the ipsilateral visual field fails to activate V1. In conclusion, conservative geniculostriate connections appear complemented by a suppression of the abnormal additional V1 input. As a consequence, hemianopia for the ipsilateral visual hemifield is expected.
>
> **Contiguous Representation** (formerly Boston Pattern): V1 comprises a contiguous map spanning both the contralateral and ipsilateral visual field. In contrast to the 'Interleaved (Suppressed) Representation', this pattern requires altered geniculostriate connections and demonstrates precortical plasticity."

Figure 2.3: "Schematic of visual field representations in the visual cortex in **(A)** control, **(B)** albinism, and **(C)** achiasma as inferred from investigations at the mesoscopic and microscopic scale. (A) Control. The binocular input to the right lateral geniculate nucleus (LGN) is organized in retinotopic maps of the left visual field (color coded blue; positive numbers) that are separate for each eye (fields with positive numbers, subscript indicates L − left, R − right eye input; the LGN is schematized as only two LGN layers with input from either eye). The geniculostriate projection (unbroken lines for left, broken lines for right eye input) results in interleaved registered retinotopic representations of the two eyes in V1. (B) Albinism. For the central visual field, the right LGN receives monocular input from the nasal (*i.e.*, left hemifield, color coded blue) and the temporal hemiretina (*i.e.*, right hemifield, color coded red) of the contralateral, that is, left, eye (indicated by the subscript L). Consequently, there is in addition to the normal input from the contralateral visual field (positive numbers) input from the ipsilateral visual field (negative numbers). Three different projections from the LGN to V1 were inferred from animal models of albinism: **'Contiguous Representation'** (former 'Boston Pattern'; geniculostriate projection depicted superior to the LGN schematic) requires a reordering of the geniculostriate projection (note the inversion of the geniculostriate projection for the additional input of the ipsilateral hemifield, *i.e.*, broken light red lines; unbroken blue lines indicate the projection of the normal input of the contralateral hemifield). **'Interleaved Representation'** (former 'True Albino Pattern'; geniculostriate projection depicted below the LGN schematic) indicates geniculostriate projections that are equivalent to those found in controls, although they operate on partially abnormal input, that is, the representation of the ipsilateral visual field (broken red lines). This cortical organization therefore indicates the conservation of the normal geniculostriate projection scheme despite abnormal LGN input. It is supported by the cortical data obtained in non-human and human primates with albinism. The same conservative geniculostriate projection is inferred for the **'Interleaved Suppressed Representation'** (former 'Midwestern Pattern'; cortical organization depicted below Interleaved Representation), except that the abnormal representation of the ipsilateral visual field is suppressed (indicated by dark gray fields with negative numbers). A consequence is hemianopia for the ipsilateral visual hemifield. (C) Achiasma. The right LGN receives monocular input from the nasal and from the temporal hemiretina of the ipsilateral, that is, right, eye (indicated by the subscript R). Consequently, there is in addition to the normal input from the contralateral visual field (blue fields with positive numbers) input from the ipsilateral visual field (red fields with negative numbers). Data on the resulting V1 representation are only available for achiasma in humans; these macroscopic imaging data support the 'Interleaved Representation' in V1, which is also found in primates with albinism. Color coding of visual field/visual field representations: blue and red shading indicate left and right hemifields, respectively, bright and dark indicate center and periphery, respectively." [Hoffmann and Dumoulin, 2015]
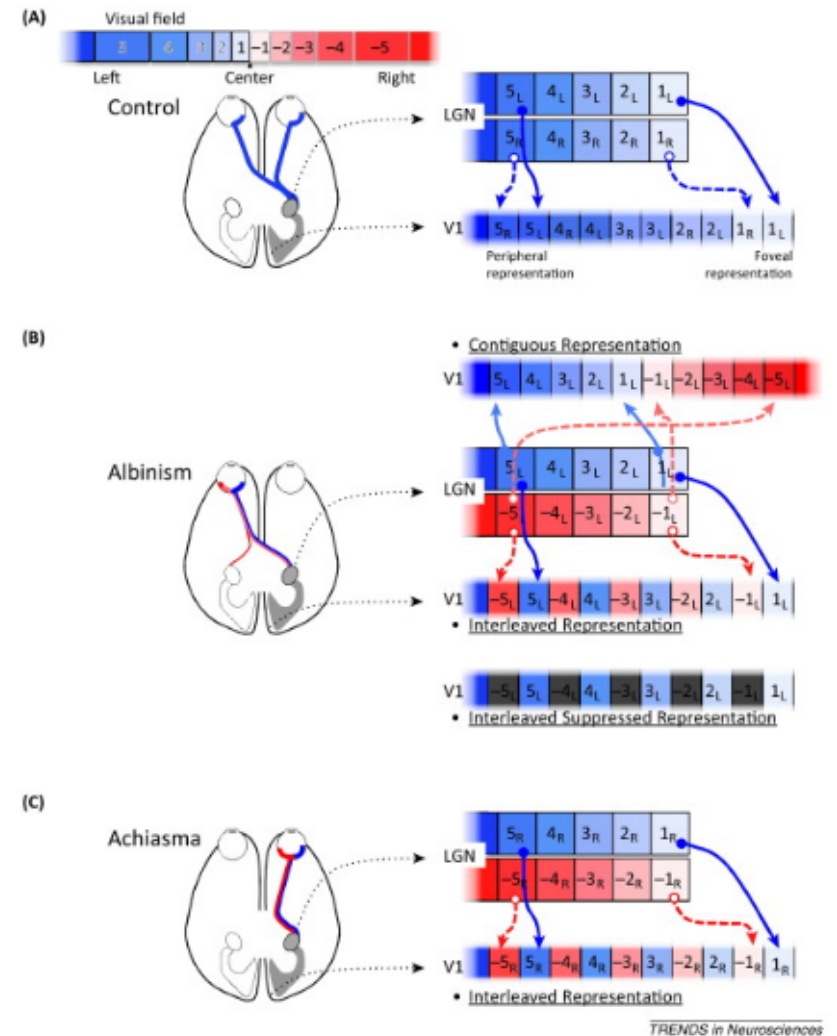
2.1.3.2 Achiasma

A cornerstone of achiasma is decreased or virtually no crossing of the optic nerves at the OC. The reduced crossing of the nasal retinal fibers [Apkarian et al., 1995] especially lead to an superimposed visual field representation in the visual cortex areas (V1-4, 3ab) [Hoffmann et al., 2012]. According to Hoffmann and Dumoulin [2015], fewer than 50 cases are published worldwide. DTI showed no difference in properties or size of fiber bundles in achiasma, too. The same is expected for albinism, but no data are available. Williams et al. [1994] showed the resulting changes in the LGN of affected Belgian sheepdogs. They described the changes of the visual stream from the OC to the LGN, resulting in a complete ipsilateral visual field representation.

As optic nerve misrouting is diagnosed with VEP [Apkarian et al., 1983, 1994], VEP tests are also used to diagnose achiasma. As albinism and achiasma are primary defined by optic nerve misroutings, the same diagnosis method is used for both: *e.g.*, misrouting-VEP. Next to the functional diagnosis, it can be validated with anatomical MRI identifying the anatomical structure of the OC [Jansonius et al., 2001; Sami et al., 2005; Pomeranz et al., 2006; Korff et al., 2003; Apkarian et al., 1994; Hertle et al., 2001]. Testing for stereo vision is often performed [Sami et al., 2005], too. Hertle et al. [2001] demand as well that Sew-Saw-nystagmus (SSN), congenital nystagmus, and optic nerve abnormalities indicate for achiasma. Here it is important to note that the achiasmic participant in Jansonius et al. [2001] had nystagmus but no see-saw-nystagmus — or at least they claim that there was only a little when tilting the horizontal plane "just a bit".

Achiasma is also associated with nystagmus [Pomeranz et al., 2006; Hoffmann et al., 2012; Apkarian et al., 1994]. The color perception is normal, too. Right-left decisions seem to be normal, as in our achiasmic participant as well [Hoffmann et al., 2012]. The participants in the study of Victor et al. [2000] also had head shudder, estropia, nystagmus, and torticollis; the same too for Sami et al. [2005]. The achiasmic participant in Jansonius et al. [2001] showed no ocular nor neurologic abnormalities and was otherwise healthy; the same too for Pomeranz et al. [2006].

2.1.4 Functional Magnetic Resonance Imaging

All functional datasets used in this thesis were collected using fMRI [Ogawa et al., 1990, 1992; Kwong et al., 1992]. fMRI uses the BOLD (Blood Oxygen Level Dependent) contrast to show brain activity. "As its name suggests, the BOLD contrast mechanism alters the T2∗ parameter mainly through neural activity-dependent changes in the relative concentration of oxygenated and deoxygenated blood. Deoxyhemoglobin (dHb) is paramagnetic and influences the MR signal unlike oxygenated Hb" [Logothetis and Wandell, 2004].

"FMRI takes advantage of changes in blood oxygenation levels, and is exploited as a physiological marker of brain activity. The blood oxygenation level dependent (BOLD) contrast is used to measure the relative amounts of oxygenated and deoxygenated haemoglobin that will vary across the brain depending on the amount of neuronal activity within local regions. This difference in signal in the brain can be measured by acquiring T2*-weighted images. T2*-weighting is related to T2-weighting, but incorporates the additional dephasing effect of the external environment on T2 relaxation times. In sum, an increase in neural activity in a brain region results in a local change in oxygenated haemoglobin, followed by an increase in blood flow to the region, resulting in a local increase in BOLD signal. Visually, this creates an MR image that is brighter in active regions." [Brown et al., 2016]

"The first simultaneous fMRI and electrophysiological recordings clearly confirmed a longstanding assumption, *i.e.*, the BOLD contrast mechanism reflects aspects of the neural responses elicited by a stimulus. The hemodynamic response primarily reflects the neuronal input to the relevant area of the brain and its processing there rather than the long-range signals transmitted by action potentials to other regions of the brain." [Logothetis and Wandell, 2004]

"However, fMRI signals are not direct measures of neuronal activity such as spikes or dendritic potentials. Instead, fMRI is used to infer changes in neuronal activity based on local metabolic and blood-based (hemodynamic) responses via intermediary processes such as neurovascular coupling and MRI contrast. [..] Although the exact relationship between the fMRI blood oxygenation level-dependent (BOLD) signal and local neural activity remains a topic of ongoing research [..]." [Uludağ et al., 2015]

"A decrease in the hemodynamic signal - the negative BOLD effect is a prominent example - is based on a neuronal deactivation, caused either by a balanced decrease in the excitatory and inhibitory activities or by a net inhibition (Shmuel et al. 2002, 2006; Stefanovic et al. 2004; Devor et al. 2007a, b; Boorman et al. 2010)." [Uludağ et al., 2015]

"Considering the specific example of responses to a visual stimulus in the primary visual cortex (V1), for example, the onset of neuronal activity is within 20 - 50 ms, while a peak response takes place within 30 - 70 ms following the onset of the visual stimulus (Maunsell and Gibson 1992). The onset of the resulting vascular response lags 1.5 - 2.5 s behind the neuronal response. The measured onset of the corresponding BOLD response depends on the paradigm, the signal-to-noise ratio (SNR), the response magnitude, and the analysis parameters. Characteristically, peak blood flow and BOLD response are not achieved until 5 - 6 s after the exposure to the stimulus." [Uludağ et al., 2015]

2.1.5 Retinotopic Mapping

"In the traveling wave method, also known as phase-encoded mapping, participants view two types of flickering checkerboard stimuli: an expanding ring which measures eccentricity (degrees from central fixation), and a rotating wedge which measures polar angle, the dimension that runs orthogonal to that of eccentricity. Each stimulus is presented in multiple cycles to cover a portion of the visual field and scans are averaged for wedge and ring stimuli in order to increase BOLD signal-to-noise ratio. As ring stimuli expand and eccentricity increases, activity travels posterior to anterior in the occipital lobes; representations of central vision reside in the occipital pole whereas the periphery is represented in anterior visual cortex. Boundaries between each early visual area (separate retinotopic maps) are identified using reversals in polar angle representations. Retinotopic maps are consistently identified across participants, but can vary in size and anatomical location across individuals." [Brown et al., 2016]

2.2 Introduction to the Experiment

Research Questions

In the present study, I address whether this organization scheme is imperative for the primary visual areas. To access this, the following steps were undertaken:

1. Measured participants with misrouting of the optic nerves at the optic chiasm (with albinism and achiasma) to gather their visual field representation (retinotopic maps) in the ventral visual cortex.

2. Compared the retinotopic maps and its parameters between controls, albinism, and achiasma to determine which organization principles stay the same and which are influenced by the misrouting.

These findings are already published as **Kaule** et al. [2014], and an adapted version of the publication is the basis of the following description of the experiment, its results, and discussion. The major finding was also presented at the ECVP2012 [**Kaule** et al., 2012].

Contributions by Collaborators

As most scientific projects, the Chapter *Visual Pathway Abnormality* was done with the contribution of others and would not been possible without them:

- Falko Kaule: adapted the stimulus to work at the 7T MRI system and with hemifield stimulation, acquired the data, wrote additional analysis tools, and analyzed the data; wrote the manuscript.

- Ramona Grzeschik: original stimulus and contributed to the manuscript.

- Barbara Wolynski: initial introduction into retinotopic mapping and analysis and contributed to the manuscript.

- Juliane Reupsch, Anita Heinecke, Synke Meltendorf: opthalmologic status of the participants.

- Jörg Stadler, Martin Kanowski, and Oliver Speck: MRI setup and data acquisition and contributed to the manuscript.

- Irene Gottlob: participant acquisition support and contributed to the manuscript.

- Michael Hoffmann: general support with analysis; wrote the manuscript.

Introduction

It is not known how the highly atypical monocular visual field representation in the early visual cortex is propagated to specialized higher tier processing stages in order to support visual pattern perception in albinism and achiasma (albinism: Wolynski et al. [2010]; Klemen et al. [2012]; achiasma: Victor et al. [2000]). Main elements of the relevant processing reside in the ventral visual cortex. Notably, the convolution of the ventral visual cortex is altered in albinism compared to controls [Bridge et al., 2014]. A potential cause of this altered cortical morphology might be the adaptation of the respective cortico-cortical connectivity in response to the abnormal representations of lower tier cortical input stages. For example, a rearrangement of the overlaid retinotopic maps of earlier visual areas could yield a contiguous retinotopic map that comprises both visual hemifields, an arrangement evident in some animal models of optic nerve misrouting [Guillery, 1986]. Such an adapted cortico-cortical connectivity would require a substantial scope of developmental plasticity in higher tier visual cortex. In contrast, the absence of rearranged maps would indicate unaltered cortico-cortical connectivity and thus an absence of such large scale plasticity of the underlying brain connectivity. Importantly, it is not imperative that the representation abnormalities are organized in the same way in lower and higher visual areas. In animal models of albinism, different organization patterns were reported in striate and extrastriate cortex. Specifically, albinotic cats appear to display different visuotopic representations in striate and extrastriate cortex [Leventhal and Creel, 1985; Schmolesky et al., 2000] or even within striate cortex [Cooper and Blasdel, 1980]. To identify the scope of developmental plasticity that guides visual map formation in the human ventral processing stream, we examined fMRI-based retinotopic maps of the VO and the posterior PHC in participants with congenital misrouting of the optic nerves. To obtain generalizable conclusions, we included participants with two different types of optic chiasm malformations, *i.e.*, with enhanced and with reduced crossing of the optic nerves, in an albinotic group, and an achiasmic individual, respectively.

2.3 Methods

2.3.1 Participants

Five controls [C1–5: normal decimal visual acuity (~ 1.0); aged 24–42 (median 27); 1 female], five participants with albinism [A1–5: aged 27–44 (median 37); 3 female; 4 with oculocutaneous and one with ocular albinism (A3)] and one achiasmic participant (Ach1, aged 22, male) were examined. A1-5 had typical symptoms of albinism based on an ophthalmological examination (iris translucency and foveal hypoplasia) and albinotic VEP lateralization indicative of misrouted optic nerves [Apkarian et al., 1983; Hoffmann et al., 2007a, 2011; Von Dem Hagen et al., 2007]. Ach1, previously described in detail [Hoffmann et al., 2012], was scanned at higher spatial resolution (2 mm isotropic voxels) for the present study. He had typical symptoms of achiasma (MRI confirmation of hypoplastic chiasma; see-saw nystagmus and achiasmic VEP lateralization Apkarian et al. [1994]) and no indications of albinism. The decimal visual acuity of the tested eye was 0.15, 0.25, 0.5, 0.13, and 0.2, for A1–5, respectively, and 0.5 for Ach1 (refractive errors were corrected for the viewing distance in the MRI scanner with custom made frames or contact lenses). The horizontal nystagmus amplitude of the tested eye was 5.9°, 3.0°, $< 0.3°$, 6.0°, and 6.0° for A1-5, respectively, and 3.5° for Ach1. No ophthalmological or neurological abnormalities apart from the ones detailed above were evident in the participants. All participants gave their informed written consent. The study was approved by the Ethics Committee of the University of Magdeburg and followed the tenets of the Declaration of Helsinki.

2.3.2 Stimulus

All participants were stimulated monocularly, *i.e.*, the left eye in controls and albinotic participants, the right eye in the achiasmic individual. As a consequence of this monocular stimulation scheme, the abnormal representation of the ipsilateral visual hemifield resides in all participants with misrouting on the right hemisphere. Conventional retinotopic hemifield mapping [Hoffmann et al., 2012] was performed. Two repetitions of polar angle mapping and of eccentricity mapping were obtained per hemifield, *i.e.*, 8 scans ($2 \times 2 \times 2 scans$) in all participants, but A5 (only 5 out of 8 scans could be acquired, *i.e.*, only condition rings in the right hemifield was repeated) and A3 (only 7 out of 8 scans were retained, as one scan [repetition of condition rings in the right hemifield] had to be discarded due to excessive head motion). For retinotopic hemifield mapping [DeYoe et al., 1996; Engel et al., 1994, 1997; Sereno et al., 1995] at 7T magnetic field strength, a section of a contrast reversing circular checkerboard stimulus (6 reversals/s, 90 cd/m^2 mean luminance) was presented in a rectangular mask (30° wide and 15° high). The stimulus contrast was set to 97% in the hemifield to be mapped and to 0% in the opposing hemifield, *i.e.*, the leading edge of the wedge disappeared when moving into the opposing hemifield and reappeared again in the mapped hemifield later after 50% of the stimulus cycle. As a consequence, the phase

range of the responses is expected to cover only 180 degrees plus some phase jitter. Seven 36 s cycles of the stimulus were projected (DLA-G150CL, JVC Ltd.) on a screen using Presentation (NeuroBehavioral Systems). The stimulus stepped either as a rotating wedge through the polar angles for polar angle mapping (clockwise and counterclockwise for the left and right hemifield, respectively; wedge width: 90°) or as a contracting ring through the eccentricities for eccentricity mapping (ring was off-screen entirely for 7 s of the 36 s stimulus cycle before reappearing in the periphery; ring width: 0.82°). The participants were instructed to maintain fixation during stimulation and to report color changes of the central target (diameter: 0.25°) via button press. Fixation was monitored during the scans with an MR-compatible eye tracker [Kanowski et al., 2007]. Because of scanner availability, participants A4 and A5 were scanned at 3T magnetic field strength. The same projector type as for the 7T scans was used while the stimulus size exceeded that of the 7T stimulus (48° wide and 24° high; ring width: 1.3°; central target diameter: 0.4° diameter). The mean luminance was set to 25 cd/m^2 and the pattern contrast to 97%. In the analyses, all relevant measures are related to participants internal reference values to take into account differences of stimulus size and luminance for 7T and 3T scanning.

2.3.3 Data Acquisition

The MRI data were acquired at either 7T (Siemens Magnetom 7T) or 3T magnetic field strength (Siemens Verio). A previous comparative study demonstrated equivalent visual area borders for fMRI-based retinotopic mapping with both magnetic field strengths [Hoffmann et al., 2009]. At the 7T MRI system, a 24-channel coil (CP transmit coil and 24 elements receive; Nova Medical, MA) was used. fMRI data were acquired using a multi-slice 2D gradient echo EPI sequence [Hoffmann et al., 2009] at either 2 mm (Ach1: TR: 2.4 s; TE: 22 ms; flip angle (FA): 80° ; 44 axial slices; matrix size: (106 × 3 × 106 scans); interleaved slice order without gap; Field Of View (FOV) (212 × 3 × 212 mm) or 2.5 mm isotropic resolution (C1-5, A1-3 TR: 2.4 s; TE: 21 ms, FA: 80° ; 42 axial slices: matrix size: (80 × 3 × 80); interleaved slice order without gap; FOV: (200 × 3 × 200) mm). At the 3T MRI system, the lower part of a 32-channel-coil, comprising 20 elements, was used to guarantee an unobstructed view of the stimulus and fMRI data were acquired at 2.5 mm isotropic resolution (A4-5; TR 2.4 s; TE 30 ms; FA 80° ; 38 axial 2.5 mm slices; matrix size: (80 × 3 × 80); interleaved slice order without gap; FOV (200 × 3 × 200) mm). Foam padding was used to minimize head motion. For each functional scan, 110 volumes were acquired at a sampling interval of 2.4 s (duration: 4:24 MM:SS, *i.e.*, 7 1/3 stimulus cycles a 36 s). At 7T online distortion correction was applied [Zaitsev et al., 2004]. Further, T1 weighted, for 7T inhomogeneity corrected [Van de Moortele et al., 2009], MPRAGE MR images were acquired at 1 mm isotropic resolution (7T: TR 2000 ms; TE 5.24 ms, TI 1050 ms; 3T: TR 2500 ms; TE 4.82 ms; TI 1100 ms) to create a flattened representation of the cortical gray matter. Gray and white matter was segmented from the anatomical MRI scan using custom

software [ITK Gray, 1.6.0.1. and MrGray (VISTA)] and hand-edited to minimize segmentation errors. Special care was taken to avoid cross talk between the gray matter of opposing hemispheres [Teo et al., 1997; Wandell et al., 2000].

2.3.4 fMRI Data Processing and Analysis

Preprocessing of the fMRI data comprised slice time correction and realignment to compensate for head motion [SPM5 (`http://www.fil.ion.ucl.ac.uk/spm/`) running with MATLAB 2009b]. Each voxel's Time-Series (TS) underwent the following analysis [MATLAB 2009b with Stanford VISTA-tools Repository 3435 [Dougherty, 2010]: (1) five temporal samples were discarded from the TS to avoid transient onset artifacts, (2) the TS were divided by the voxel's mean intensity, (3) the TS were filtered with a high-pass cut-off of 4 cycles/scan, (4) the TS of repeated experiments were averaged, (5) Fourier analysis was applied to the TS to obtain the amplitude and phase for each frequency, and (6) the coherence with a sinusoid with a frequency equal to that of the visual stimulation (1/36 Hz), was calculated [Engel et al., 1997]. After registration of the T1 weighted images to the T2* weighted images' coordinate frame, the results of the coherence analysis were projected onto the flattened representation of the cortical surface (flatmap) [Engel et al., 1997]. Subsequently, the coherence and phase values were blurred by convolving a Gaussian kernel (1.7 mm full width at half maximum) with the complex vector representation. A coherence threshold of 0.26, *i.e.*, corresponding to a significance threshold of P < 0.005, [Silver et al., 2005] was applied to retain the stimulus driven responses. Further, a phase window was applied to the polar angle mapping data, which exceeded the stimulation epoch of the stimulus cycle, *i.e.*, 180°, by ±15%, *i.e.*, 27°, to account for phase jitter. Dedicated functions available in VISTA-tools were used to determine the activated surface area. Further calculations were performed in IGOR Pro 6.22A (WaveMetrics, Lake Oswego, OR).

2.3.5 Statistics - Ventral Areas

Two-way ANOVAs (factors: participant group and visual areas) were performed with SPSS 21 (IBM, NY) to assess (i) surface areas, (ii) phase maps, and (iii) response amplitudes. To reduce the degrees of freedom of the statistical models, we collapsed the visual areas into two groups of visual areas: early visual areas *i.e.*, covering V1, V2, and V3 (termed V1/2/3) and higher areas of the ventral pathway, *i.e.*, covering VO1, VO2, PHC1, and PHC2 (termed VO/PHC). The similarity of the phase maps was assessed by correlating pairs of the obtained phase maps with each other using circular statistics implemented in MATLAB [Berens, 2009] to take the circular nature of the phase data into account. The resulting correlation coefficients were z-transformed prior to statistics. The sphericity assumption was met for phase maps and response amplitudes.

2.3.6   Definition of Visual Areas

Diverging delineations and nomenclatures of the ventral human visual areas have been proposed in the past. These are likely due to inter-individual differences in the vasculature of this brain region [Winawer et al., 2010] and related to differences of the cortical organization in humans and macaque monkeys [Gattass et al., 1988]. We adhere to the nomenclature reviewed in Wandell et al. [2007] and Silver and Kastner [2009]. According to this work, the previously described retinotopically organized areas of the ventral visual processing stream, *i.e.*, V4, VO1, VO2, PHC1, and PHC2, comprise representations of the entire contralateral visual hemifield [Arcaro et al., 2009]. In the present study, these visual areas were delineated in each individual on the basis of the respective eccentricity and polar angle maps obtained with the above procedures following Brewer et al. [2005] and Arcaro et al. [2009]. Specifically, V4 is identified as a hemifield representation adjacent to the dorsal portion of ventral V3 (in contrast, in macaques V4 has a ventral and dorsal portion that comprise the upper and lower quadrant of the contralateral visual hemifield, respectively [Gattass et al., 1988]). The foveal representation of V4 resides at the occipital pole and is part of the eccentricity map also comprising V1, V2, and V3 [Wade et al., 2002]. V4's polar angle map is parallel to that of V3. The visual field clusters VO1/2 and PHC1/PHC2 are located anterior to V4. The polar angle maps and consequently the area borders of VO1, VO2, PHC1, and PHC2 are arranged perpendicular to the representation of the upper vertical meridian in V3, *i.e.*, to the ventral border of ventral V3.

The recognition of the representation of the upper vertical meridian in the polar angle maps allows for the identification of the VO1/VO2 and the PHC1/PHC2 border. The recognition of the representation of the lower vertical meridian allows for the identification of the VO2/PHC1 border. Furthermore, while the more peripheral visual field representations reach the ventral V3 border, the central representations are located more ventrally. Thus the identification of the local minima of the eccentricity maps ventral to V3 allows for the confirmation of the location of the foveal confluence of the VO1/VO2 cluster and of the PHC1/PHC2 cluster.

2.4   Results

2.4.1   Cortical Representations of Polar Angles and Eccentricities

For a qualitative assessment of the polar angle and eccentricity mapping data, we projected the phase values of suprathreshold voxels onto the flattened representation of the right occipital lobe (Figure 2.4 for a representative example of controls, albinism, and achiasma). For all conditions, *i.e.*, controls, albinism, and achiasma, extensive significant BOLD-responses were evident in the visual cortex for stimulation in the contralateral visual hemifield. The responses covered the early visual cortex and large parts of the ventral visual cortex. The respective phase signatures were in accordance with those previously described [Wandell

et al., 2007], which allowed for the delineation of the early visual areas and of the ventral visual areas V4, VO1, VO2, PHC1, and PHC2. These areas have previously been described to comprise representations of the contralateral hemifield with characteristic eccentricity and polar angle maps [Arcaro et al., 2009; Brewer et al., 2005]. While V4 is part of the eccentricity map that also comprises the early extrastriate cortex with a foveal representation at the occipital pole, the eccentricity maps of VO1/2 and PHC1/2 border ventral V3. Their peripheral visual field representations reach the ventral V3 border, the central representations are located more ventrally. As detailed in Methods, VO1/2 and PHC1/2 can generally be delineated from each other along the representations of the vertical meridian from polar angle maps, and the foveal confluence of the VO1/VO2 and of the PHC1/PHC2 cluster can be confirmed from eccentricity maps.

Within the limits of their interindividual variability [Arcaro et al., 2009; Brewer et al., 2005], the above characteristics of the phase signatures of the ventral areas were evident in the participants of the present study. In contrast to the areas of the ventral stream, the areas dorsal to the early visual areas, could, apart from V3A/B, not be delineated reliably in most of the participants and were therefore not assessed in the present study. In contrast to the passive viewing hemifield mapping applied in the present study, task engaging mapping might be required to obtain sufficient hemifield maps of the intraparietal sulcus [*e.g.*, , [Konen and Kastner, 2008]]. For stimulation in the ipsilateral visual hemifield, we obtained sparse responses for the controls. These were, in accordance with previous reports [Hoffmann et al., 2003; Tootell et al., 1998], mostly confined to the representations of the central visual field and of the vertical meridian — and to some intrusions of negative BOLD responses [Shmuel et al., 2006; Smith et al., 2000, 2004]. For albinism and achiasma, however, we observed extensive responses to stimulation in the ipsilateral visual hemifield in great expanses of the visual cortex. This is not only evident from the phase maps depicted in Figure 2.4, but also from the average time courses of the BOLD responses during polar angle mapping depicted in Figure 2.5.
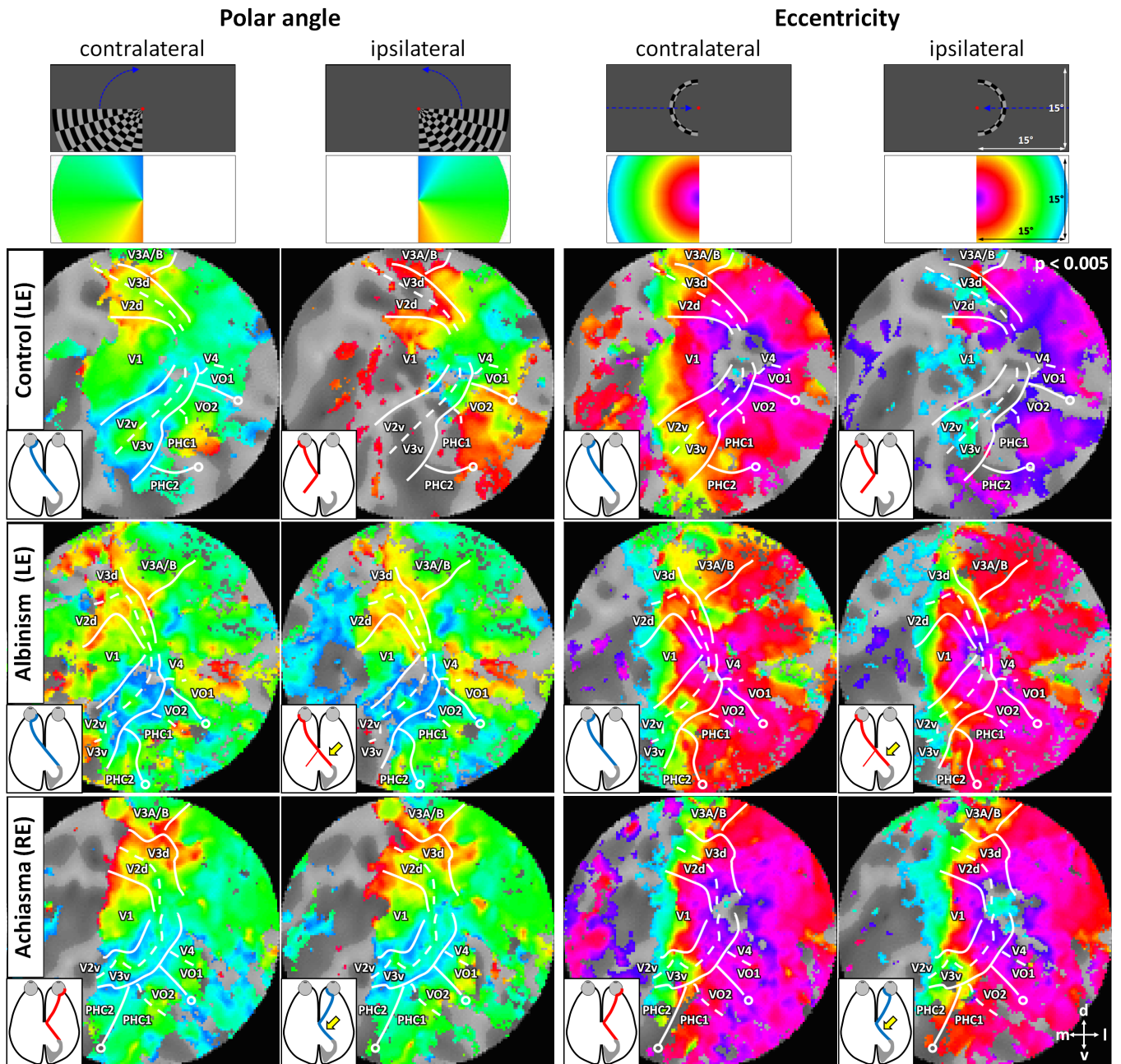
Figure 2.4: Flattened representations of the right occipital lobe for representative individuals of the investigated cases, *i.e.*, control (C1; left eye stimulated), albinism (A1; left eye stimulated), and achiasma (Ach1; right eye stimulated). The superthreshold phase maps for polar angle and eccentricity mapping in the contra- and ipsilateral visual hemifield are projected onto the flatmaps. For all individuals, orderly mappings of the contralateral visual hemifield were evident, which allowed for the identification of early and ventral visual areas. In the control, ipsilateral mappings were restricted partly to representations of the vertical meridian and the central visual field and to spurious activations presumably due to negative BOLD modulations. In albinism and achiasma, extensive orderly mappings of the ipsilateral visual hemifield were evident that resembled those of the contralateral hemifield. The inferred optic nerve projection is given in the insets, abnormal projections are indicated with a yellow arrow. The top row indicates stimulus schematics; second row depicts color codes (see Methods for details). Open circles indicate a representation of the visual field center; lines indicate visual area boundaries (representation of horizontal and vertical meridians) as inferred from the polar angle maps to stimulation in the contralateral visual hemifield. Abbreviations: V1-4: visual areas 1-4; PHC 1/2: parahippocampal cortex 1/2; VO 1/2: ventral occipital areas 1/2.
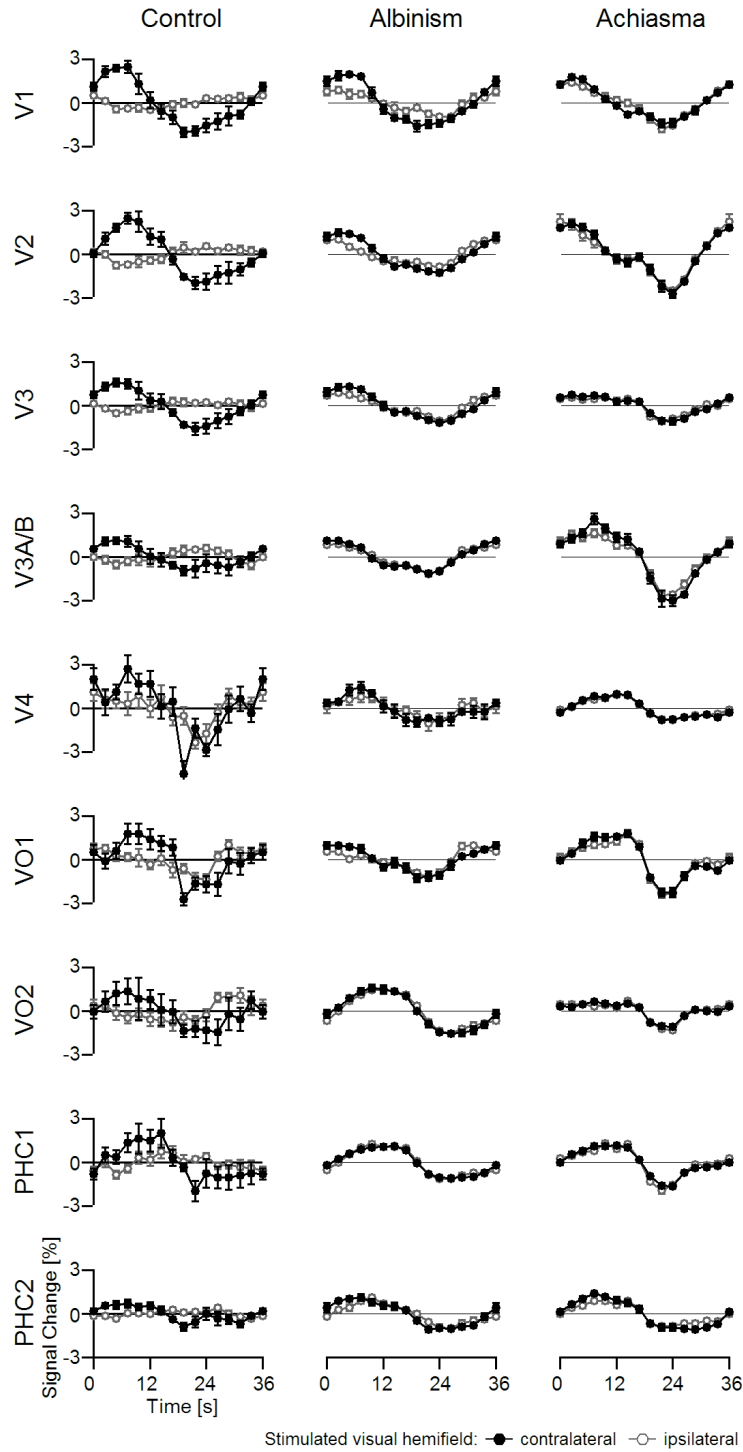
Figure 2.5: Times series of the polar angle mapping data presented in Figure 2.4 (average across all voxels of the respective visual area; average across 7 cycles $\pm$ SEM). Positive BOLD responses are expected predominantly during the first half of the stimulation cycle (as detailed in Methods section). It should be noted that apparent area-related phase shifts within this hemicycle are a natural consequence of different contributions of specific polar angles to the respective average responses. The ROIs comprised voxels that were significantly driven for stimulation in the contralateral visual hemifield. Importantly, even in the areas PHC1/2, stimulation in either hemifield evoked comparable responses in albinism and achiasma but not in the control, where positive BOLD responses were obtained for contralateral hemifield stimulation only. For expansion of the area labels, see Figure 2.4.

While in albinism and achiasma the time courses were similar for stimulation in opposing hemifields, they differed for the controls, *i.e.*, sizable BOLD responses were only evident for stimulation in the contralateral visual hemifield. In albinism and achiasma, responses to ipsilateral stimulation resulted in systematic phase maps of the ipsilateral hemifield. This applied to both the responses of early visual cortex and for areas of the ventral processing stream, *i.e.*, VO1, VO2, PHC1, and PHC2. Remarkably, these maps were, to a large extent similar to those of the contralateral visual hemifield. This indicates a systematic mirror symmetrical overlay of retinotopic maps not only in early visual areas, but also in the ventral processing stream of the visual cortex contra- and ipsilateral to the stimulated eye in albinism and achiasma, respectively. These findings are likely due to a propagation of the organization pattern of the early visual cortex, *i.e.*, an overlaid retinotopic representation of opposing hemifields, to the ventral visual processing stream. We detailed the characteristics of the obtained maps systematically in three separate quantitative analyses that compared the responses to stimulation in the ipsi- and contralateral hemifield with respect to activated cortical surface area, phase maps, and response amplitudes.

2.4.2   Extent of the Representation of the Ipsilateral Visual Field

To quantify the relative extent of the representation of the ipsilateral visual field, we determined the activated cortical surface area, *i.e.*, comprising voxels that exceed a significance threshold of p < 0.005, for stimulation in the ipsi- and contralateral hemifield. Subsequently, we calculated the relative activated ipsilateral surface area (surface area$_{ipsilateralstimulation}$/surface area$_{contralateralstimulation}$ × 100%) for each visual area (*i.e.*, V1, V2, V3, V3A/B, V4, VO1/2, PHC1/2) as depicted in Figure 2.6. For these areas taken together, the relative activated ipsilateral surface area was $27 \pm 5\%$, $66 \pm 13\%$, and 96% in the control group, the albinism group, and in the achiasmic individual, respectively.

This supports previous reports that the representation abnormality in albinism is associated with partial optic nerve misrouting of varying degrees [Creel et al., 1981; Hoffmann et al., 2003, 2005; Von Dem Hagen et al., 2007] while it is associated with more complete misrouting in achiasma [Hoffmann et al., 2012; Prakash et al., 2010], as evident in Figure 2.4. In fact, an analysis of the phase maps of V1 obtained from the five participants with albinism demonstrated that the abnormal representation of the ipsilateral horizontal meridian varied within a range of $3.6\degree$ to $13.0\degree$ [horizontal extent in A1 to A5: $12.7\degree$, $3.6\degree$, $10.2\degree$, $13.0\degree$, $5.9\degree$. To assess the significance of the representation abnormality and its dependence on visual area, we compared the control and the albinism group data, *i.e.*, the relative activated ipsilateral surface area, in a two-way-ANOVA [factors: participant group (controls and albinism) and visual areas (V1/2/3 and VO/PHC)]. This analysis confirmed the group difference ($F(1,16) = 13.12$, $P = 0.002$), while neither the factor visual area ($F(1,16) = 0.679$, $P = 0.422$) nor the interaction of the factors group 3 visual area were significant ($F(1,16) = 0.002$, $P = 0.961$). This finding indicated a largely undiminished propagation of

the abnormal representation in the early visual areas to advanced processing stages in the ventral visual cortex in albinism.
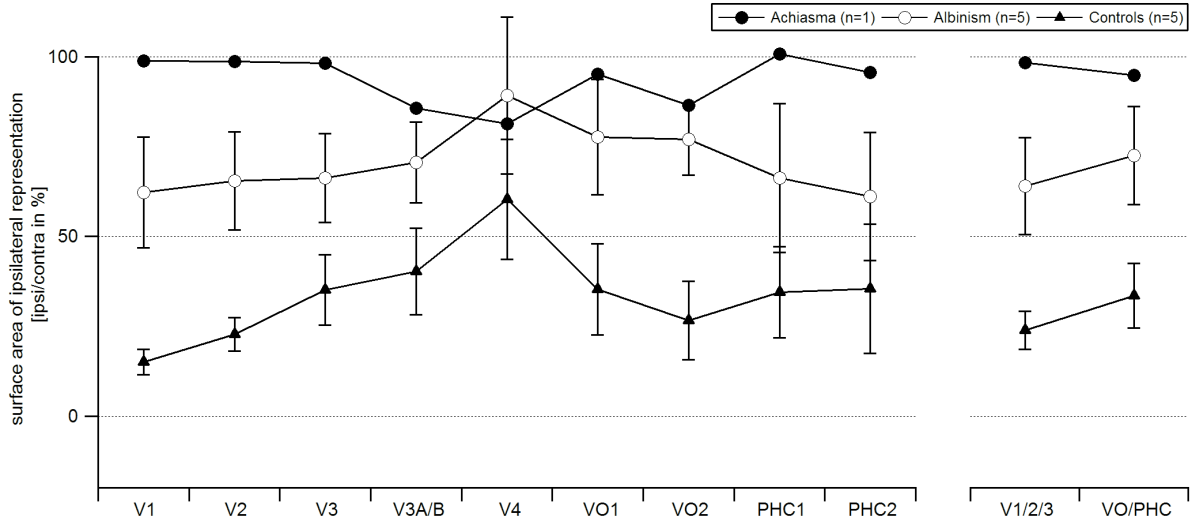

Figure 2.6: Relative surface area of the ipsilateral representation. The respective correlation coefficients are given as a function of visual area for controls, albinism, and achiasma (mean ± SEM). Statistics were computed for the visual area groups V1/2/3 and VO/PHC as detailed in the Methods section. The control group and the albinotic group differ significantly, but independent of visual area group as detailed in Results. For expansion of the area labels see Figure 2.4.

2.4.3 Cortical Overlay of the Representations of Opposing Hemifields

To determine the organization of the additional input to the visual cortex, we conducted a detailed comparison of the phase maps for ipsi- and contralateral stimulation. In Figure 2.4, similar phase maps are evident for stimulation in opposing hemifields in albinism and achiasma. These maps indicate that the cortical representations of opposing visual hemifields are organized as retinotopic cortical overlays of mirror-symmetrical positions in the visual field, not only in early but also in higher visual areas. To assess this in a quantitative manner, we applied correlation analyses to determine the similarity of the phase maps obtained for opposing hemifields (Figure 2.7). We conducted these analyses for ROIs that were restricted to supra-threshold voxels (P < 0.005) upon stimulation of the ipsilateral visual field (ROI_{ipsi}) and to the phase window of the stimulation epoch for polar angle and eccentricity mapping (see the Methods section). This way we ensured, in particular for albinism with its interindividually variable extent of the abnormal representation [Hoffmann et al., 2005], that only voxels were included that were driven by ipsilateral stimulation.
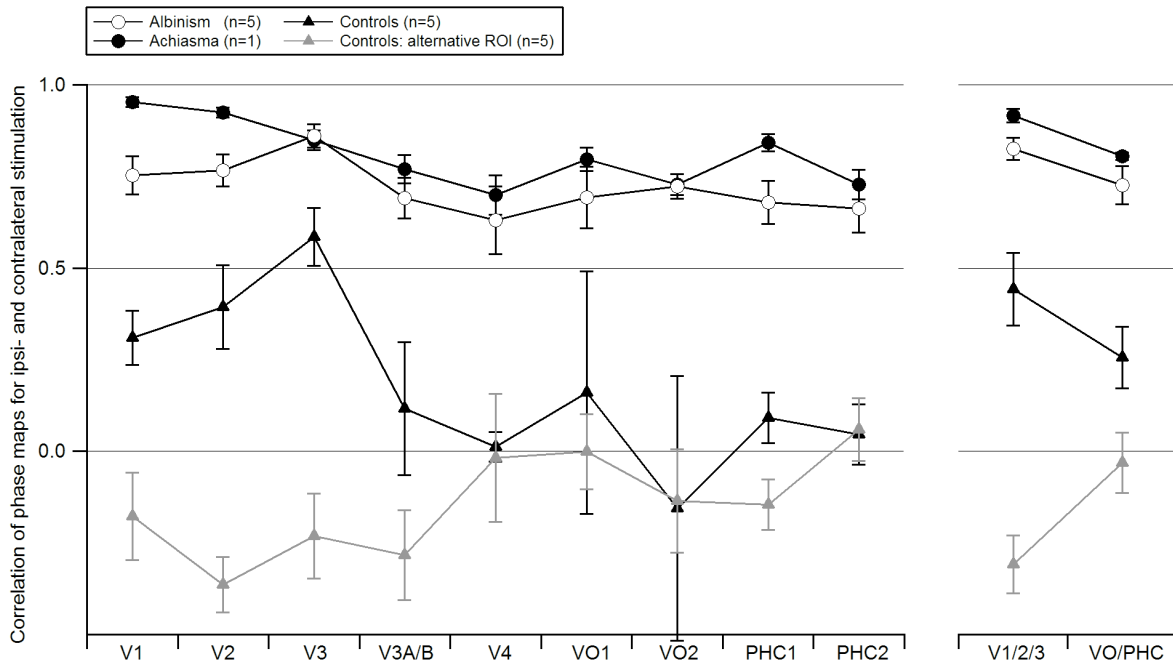
Figure 2.7: Comparison of the phase maps of the right occipital lobe obtained for stimulation in the ipsi- and the contralateral hemifield. The respective correlation coefficients are given as a function of visual area for controls, albinism, and achiasma (mean ± SEM). Statistics were computed for the visual area groups V1/2/3 and VO/PHC as detailed in Methods. The control group and the albinotic group differ significantly, but independent of the visual area group. In addition to the data from ROIs, defined by voxels driven by stimulation in the ipsilateral visual hemifield, data from an *alternative ROI*, defined by voxels driven by stimulation in the contralateral visual hemifield are presented for the control group. For expansion of the area labels see Figure 2.4.

For the control group, this selection yielded ROIs that were confined to the residual representation of the ipsilateral hemifield. As a reference, we included an additional depiction of the control data using ROI definitions that were based on voxels driven by contralateral stimulation (*alternative* ROI in Figure 2.7). Comparing phase maps for ipsi- and contralateral stimulation with the correlation analysis, we obtained for all visual areas assessed, higher correlation values for albinism and achiasma than for controls. This indicated that in albinism and achiasma cortical representations of opposing visual hemifields were organized in similar retinotopic maps. Correspondingly, a two-way ANOVA [factors: participant group (controls and albinism) and visual areas (V1/2/3 and VO/PHC)] for ROI$_{ipsi}$ demonstrated a significant difference between the correlation coefficients of the albinism and the control group ($F(1,16) = 35.299$, $P < 0.001$), while there was no significant effect for visual areas ($F(1,16) = 3.761$, $P = 0.07$). Importantly, there was no significant interaction of participant group 3 visual area ($F(1,16) = 0.203$, $P = 0.658$). This underlines that the organization of visual input from opposing hemifields as a retinotopic overlay is preserved in the ventral processing stream.

2.4.4 Relative Strength of the Cortical Responses to Stimulation of Opposing Hemifields

With the above analyses, we demonstrated for albinism and achiasma that the same voxels that were driven by the ipsilateral visual field, *i.e.*, ROI$_{ipsi}$, were also driven by the contralateral visual field, *i.e.*, by a mirror symmetrical visual field location with respect to the vertical meridian. In a further analysis, we determined whether these voxels responded with the same strength to both hemifields. In Figure 2.8, the response amplitudes of the ipsilateral representation are given as the percentage of the response amplitude of the contralateral representation, *i.e.*, the relative response. For the albinotic group, we observed a small but significant reduction of the responses of the representation of the ipsilateral hemifield (average relative response $\pm SEM : 86 \pm 4\%$). A two-way-ANOVA comparing the response amplitudes obtained for stimulation in the contra- and ipsilateral visual field across visual areas (factors hemifield stimulated [contralateral and ipsilateral (F(1,68) = 6.942, P = 0.01] and visual areas [V1/2/3 and VO/PHC; F(1,68) = 1.13, P = 0.292]) demonstrated that this hemifield-specific reduction was independent of the visual areas stimulated (non-significant interaction of factors hemifield stimulated and visual areas, F(1,68) = 0.204, P = 0.653). No such response reduction was observed in the achiasmic individual [average relative response: 99%]. We assume that the slight amplitude reduction for albinism might be due to the fact that it is only a part of the ipsilateral hemifield that is abnormally represented in albinism and that some voxels that were included in ROI_{ipsi} reflect the transition zone with naturally less ipsilateral responses. In that case, it would be expected that the exclusion of this transition zone from the ROIs ($ROIs_{restricted}$) might yield higher amplitude measures, as compared to the original ROIs ($ROIs_{original}$). We tested this specifically in three participants with albinism and sufficiently large ROIs of the abnormal representation in all visual areas of interest (V1/2/3, VO1/2, and PHC1/2). For this purpose, we created $ROIs_{restricted}$ that were centered with respect to $ROIs_{original}$ and shrunk to $\sim 25\%$ of the $ROIs_{original}$ area. As a consequence, these ROIs were focused on the cortical representations of the horizontal meridian that are dominated by the overlay of abnormal and normal representation. We observed a slight but non-significant trend of increased amplitudes for $ROIs_{restricted}$ (V1/2/3, $ROIs_{original}$ vs. $ROIs_{restricted}$: $83.6\% \pm 2.7\% vs. 88.4\% \pm 6.1\%; VO/PHC, ROIs_{original} vs. ROIs_{restricted} : 91.8\% \pm 9.9\% vs. 93.8\% \pm 3.9\%$). Primary and higher visual areas (V1-4, V3ab, PHC, LO) are organized in a conventional pattern with superposition of the retinal feeding to the hemisphere [**Kaule** et al., 2014; Hoffmann et al., 2003].
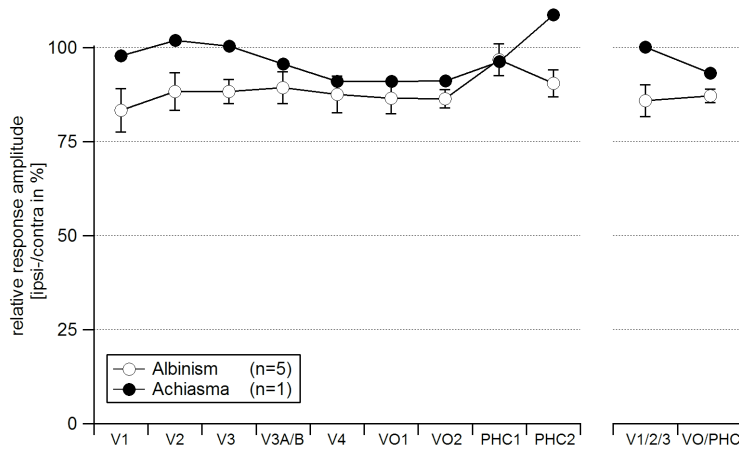
Figure 2.8: Relative response amplitudes to stimulation in the ipsilateral visual hemifield. The amplitudes are given as a function of visual area for albinism (mean ± SEM) and achiasma. For expansion of the area labels, see Figure 2.4.

2.5   Discussion

We report abnormal visual field maps in the ventral visual cortex of individuals with congenitally abnormal input to the primary visual cortex that is caused by enhanced or reduced crossing of the optic nerves at the chiasm in albinism and achiasma, respectively. The retinotopic representations of opposing hemifields were superimposed in the visual field map clusters VO1/2 and PHC1/2, an arrangement also evident in the early visual cortex of these individuals. Consequently, an exclusive retinotopic organization of the contralateral visual hemifield is not imperative for the organization of visual areas of the ventral pathway. Instead, it appears that the visual field map clusters VO1/2 and PHC1/2 follow the gross-organization scheme that is evident in lower tier visual cortex even if this is abnormal. A potential mechanism underlying this organization pattern would be the unaltered propagation of the organization in the earlier visual cortex to downstream areas via largely unaltered cortico-cortical connections despite abnormal input to V1.

2.5.1   Plausibility of the Observed Cortical Mapping

The mappings we report for the early visual cortex of individuals with congenital malformations of the optic chiasm are in close agreement to earlier reports of independent measurements in different (albinism: Hoffmann et al. [2003]; achiasma Davies-Thompson et al. [2013]; Hoffmann et al. [2012], participant AC2]), or the same participants (achiasma: Hoffmann et al. [2012], participant AC1]) and confirm the previously reported cortical overlay of retinotopic maps of opposing visual hemifields in early visual cortex. The results are also in agreement, though partial, with those previously reported in an extremely unusual case, *i.e.*, an individual who lost one hemisphere during embryonic development [Muckli et al., 2009]. Even here, overlaid representations were evident in the dorsal portions of V1 and V2. In

ventral V2, however, islands of non-overlapping maps were observed, which might be related to alterations in the underlying reorganization and/or to the effect of circumscribed defects in the upper visual hemifield field of that individual. Some participants of the present and of previous studies have sizable nystagmus. While small-amplitude nystagmus and other fixation instabilities have little impact on the characterization of retinotopic maps [Baseler et al., 2011; Levin et al., 2010], an impact of larger amplitudes cannot be excluded per se. As similar early visual cortex mappings were previously reported for individuals with albinism with horizontal nystagmus amplitude below and above 2°, such effects appear to be negligible [Hoffmann et al., 2003], but the potential effects of nystagmus still deserve evaluation. Fixation instabilities centered around fixation could introduce spatial blur, which spreads the signal across the cortex and reduces the signal-to-noise-ratios of the signals but would not cause sizable spurious retinotopic maps. They would thus leave the conclusions of the present and previous studies largely unaffected. In contrast, a systematic deviation from central fixation might have a stronger effect on the retinotopic mapping signatures. It would have a distinct effect particularly on the eccentricity maps of the central visual field, *i.e.*, inverted phase progressions along the representation of the horizontal meridian. While such effects would be strongest in areas with extended representations of the visual field center, *i.e.*, V4 and VO1/2 [Arcaro et al., 2009], they should already be evident at the input stage of the visual cortex, *i.e.*, V1, where they can be judged best due to the size of this area and the clarity of the phase signatures [Winawer et al., 2010]. Such phase inversions were not observed (Figure 2.4).

2.5.2 Visual Function in the Presence of Large-Scale Cortical Representation Abnormalities

In the presence of enhanced or reduced crossing of the optic nerves at the chiasm, the organization of the visual field maps in all visual areas examined follows a largely similar pattern, namely that of overlaid retinotopic representations of opposing hemifields. Still, visual function is relatively unaffected, with the exception of nystagmus and the absence of stereopsis. The affected individuals make effective use of their vision in daily life, including sport activities and reading [Apkarian et al., 1994, 1995; Hoffmann et al., 2012; Prakash et al., 2010; Victor et al., 2000]. Visual field sensitivities are largely normal. In particular, there are no visual field defects that are specifically associated with the abnormal representation of the nasal retina [Hoffmann et al., 2007b, 2012]. Further, there is no evidence for perceptual crosstalk across opposing visual hemifields, neither in achiasma [Victor et al., 2000] nor in albinism [Klemen and Chambers, 2012], as it might be expected from the cortical overlay of opposing hemifields. Finally, pattern and object perception and object recognition do not appear to be selectively impaired [Klemen and Chambers, 2012; Victor et al., 2000; Wolynski et al., 2010]. While, lesions in the ventral visual cortex severely impair object recognition [Konen et al., 2011], it appears that a pronounced mapping abnormality in these areas is not

necessarily associated with a distinct dysfunctionality. This suggests that normal mapping is not imperative for the general functionality of the ventral visual cortex. Future specific psychophysical examinations to detail the integrity of visual object perception will help to identify the limits of the preservation of normal function in the presence of the abnormal mappings described in the present study.

2.5.3 Early Visual Cortex Organization in Congenital Chiasmatic Malformations

The consequences of chiasmatic abnormalities on the organization of the visual cortex have been studied in detail in various models of albinism in order to uncover how the additional input from the ipsilateral visual hemifield is represented at the level of the visual cortex. Remarkably, three different cortical organization patterns were found in non-primates [reviewed in Guillery [1986]; Hoffmann and Dumoulin [2015]]. The geniculo-striate connections can be (a) reordered to yield a contingent retinotopic representation of both visual hemifields ('Boston pattern'), (b) unaltered, but not driving activity in the visual cortex due to intra-cortical suppression ('Midwestern pattern'), (c) unaltered and driving the macroscopically superimposed cortical representations of opposing hemifields ('Interleaved representation'). The latter pattern was primarily reported in primates [Davies-Thompson et al. [2013]; albinism: Guillery et al. [1984]; achiasma: Hoffmann et al. [2003, 2012]; Bao et al. [2015]] and was also confirmed in the present study. The interleaved representation pattern is likely due to a reassignment of the cortical ocular dominance columns to hemifield dominance columns [Guillery, 1986]. This reassignment is the direct consequence of unaltered geniculo-striate projections, which normally result in interleaved cortical representations of the two eyes, *i.e.*, ocular dominance columns. In the case of misrouted optic nerves, however, they result in interleaved cortical representations of monocular input from opposing visual hemifields, *i.e.*, hemifield dominance columns. A cortical organization that follows the 'interleaved representation pattern' at the stage of the primary visual cortex is therefore a simple way to allocate resources for the additional representation of the ipsilateral visual field, since it is based on reassigning the resources normally used for processing the, now missing, input from the ipsilateral eye in albinism and the contralateral eye in achiasma.

2.5.4 Higher Visual Cortex Organization in Congenital Chiasmatic Malformations

We report evidence for macroscopically superimposed retinotopic maps of opposing visual hemifields not only in the primary and early visual cortex, but in higher processing stages as well. A likely mechanism for the propagation of this organization pattern through the visual cortex, are largely unaltered cortico-cortical projections. This way the organization pattern of early visual areas would be adopted by higher visual areas. Such a conservative mechanism appears to prevail even for the specialized visual field maps in the PHC.

Incorporating a representation of the ipsilateral visual field is much more demanding at the level of extrastriate and higher tier visual cortex, since at this stage many neurons normally receive predominantly binocular input [Felleman and Van Essen, 1987; Maunsell and Van Essen, 1983; Tanabe et al., 2005]. Consequently there are, in contrast to V1, no spare resources in albinism and achiasma that would normally be selectively concerned with processing the monocular input that is missing in albinism or achiasma. As a consequence, part of the neural resources normally available for processing the contralateral visual field must be made available for processing the additional input from the ipsilateral visual field. Remarkably, the relative responses of the ipsilateral representation [amplitude$_{ipsilateral representation}$/amplitude$_{contralateral representation}$ $\times 100(\%)$ as depicted in Figure 2.7] did not differ between striate, extrastriate cortex, and the two visual field map clusters in the ventral processing stream, *i.e.*, the VO cortex and the posterior PHC, neither in albinism and nor in achiasma. This demonstrated undiminished processing of the additional visual input up to higher levels of visual processing. We conclude that the mechanisms that govern the allocation of neural resources for processing of the additional visual input appear to be operating with a similar effectiveness for striate, extrastriate, and higher tier visual areas. Finally, the remote representation of corresponding parts of the visual field, *i.e.*, on opposing hemispheres, in albinism and achiasma might induce changes to the interhemispherical information flow via the splenial callosal connections. Diffusion tensor imaging studies revealed largely unaltered interhemispheric splenial connections in achiasma [Hoffmann et al., 2012; Davies-Thompson et al., 2013], but the issue deserves to be studied in more detail and to be extended to albinism.

2.5.5 Principles of Visual System Organization in Achiasma and Albinism

From the direct juxtaposition of the organization of the visual cortex in albinism and achiasma, general principles governing map formation in the human visual cortex can be inferred. In both types of visual pathway abnormalities, *i.e.*, enhanced and reduced optic nerve crossing, visual hemifields are made available for visual perception [Hoffmann et al., 2007b, 2012; Klemen and Chambers, 2012; Victor et al., 2000; Wolynski et al., 2010]. As detailed above, a combination of unaltered development of the thalamo-cortical and cortico-cortical connections on the one hand, and an adaptation of intracortical connections, *e.g.*, , experience driven cortical pruning [Sinha and Meng, 2012], on the other hand, might serve to mediate an independent visual perception in opposing visual hemifields in both human albinism and human achiasma [Hoffmann et al., 2012; Klemen and Chambers, 2012]. In contrast, a variety of mechanisms appear to be available in non-primate animal models of albinism, even within the same species or individual [reviewed in: Guillery [1986]; Hoffmann et al. [2003]]. One of these, the Midwestern pattern, actually fails to translate the additional visual input into visual perception, which results in selective visual field defects [Elekessy et al., 1973; Garipis

and Hoffmann, 2003] that are not evident in primates with chiasmal abnormalities [Guillery et al., 1984; Hoffmann et al., 2007b; Muckli et al., 2009]. In contrast, uniform developmental mechanisms that reflect an interplay of plasticity and stability govern the development of the primate visual system and preserve fundamental aspects of visual function despite abnormal visual field representations even for high-level visual processing.

The misrouting in albinism and achiasma leads to superimposed instead of opposed hemifield maps. The same counts for higher areas as VO and PHC [**Kaule** et al., 2014].

Chapter 3

Functional Alignment: Hyperalignment

3.1 Introduction to the Experiment

Research Questions

The Chapter *Functional Alignment: Hyperalignment* aims to develop a clinical application: a tool which can be used to help with diagnosis and validation of visual field defects. At the moment, the validation of visual field defects mostly relies on direct feedback of patients and proper fixation.

> "Those with eye disease involving the fovea have difficulty in keeping the eyes fixed on a target in comparison to normally sighted individuals. Eye movements will in turn affect the fMRI data acquired, as stimuli may fall on a different part of the visual cortex in participants with unstable fixation; therefore, when mapping out visual field representations in visual cortex, eye movements could be a confounding factor." [Brown et al., 2016]

The principal goal is to investigate a non-visual stimulus (*e.g.*, audio-book), to objectively evaluate visual field defects in patients, that does not require the patient's feedback or visual cooperation: It should be more objective than methods that require a subject's feedback and visual cooperation.

Hyperalignment is functional alignment and refers to the method used in Haxby et al. [2011]. It is spatially very restricted. For application on visual areas, this implies strong visual stimulation. To be able to use whole brain activation, the Connectome-Hyperalignment (Hyperalignment using a Connectome), and its variant the Pre-Connectome-Hyperalignment (Hyperalignment using a Pre-Connectome), was introduced.

When using the (Pre-)Connectome-Hyperalignment, the reference data should have activation in a wide range of cortical areas, including visual areas. Especially for clinical use, an interesting stimulus helps with patient compliance and as result, should generate better data. The complex activation pattern of the brain is expected to be widely similar across controls and patients, too.

In the focused application, impaired patients listen to an audio book to get an objective measurement for visual field defects and/or changes in retinal representations. The focus was to be able to use whole brain data, accordingly also audio and more complex data, to transfer visual ROIs. The importance for the application to visually impaired patients lies in the avoidance of fixation dependence methods *i.e.*, retinotopic mapping via traveling wave [Engel et al., 1997] or pRF paradigm [Dumoulin and Wandell, 2008]. An alternative could be in using naturalistic/complex stimuli [Dubois and Adolphs, 2016]. Using more "interesting"stimuli additionally make it easier for the patients to maintain attention to the stimulus. Anatomical alignment would only transform the functional data on the basis of structural information. Changes in the functional brain activity, *i.e.*, visual impairments, are not covered by this method of transformation. The transformation matrix was derived from the activation patterns (time series) of the ROIs' voxel that should be transferred. To sum every preference of a preferred stimulus, a movie would be the best for the purpose of generating visual activation with an fixation-independent stimulus. Therefore, data from the presentation of a pure audio-movie and an audio-visual movie has been chosen [Hanke et al., 2014, 2016] as well. Therefore, I undertook the following steps:

1. Writing a retinotopic mapping processing pipeline working with open access tools.

2. Generating retinotopic maps to use as reference for the functional alignment quality.

3. Writing a processing pipeline to automatically process the data from the data papers Hanke et al. [2016, 2014]; Sengupta et al. [2016] and to help assess the data quality (initially using the openfmri.org-data format [Poldrack et al., 2013], later using BIDS data format [Gorgolewski et al., 2016]).

4. Converting the pipeline for improved performance using parallel processing on a computational cluster.

5. Implementing the original Hyperalignment [Haxby et al., 2011] into the processing pipeline.

6. Testing and implementing different ways of extending the original Hyperalignment.

7. Wrote the analysis to validate the quality of the different Hyperalignment variants, regarding transferability of cortical visual field representations, *i.e.*, retinotopic maps, across subjects.

Contributions by Collaborators

The data used for this study are described and taken from multiple data papers which I co-authored: audio movie from Hanke et al. [2014], audio-visual movie from Hanke et al. [2016], and retinotopic mapping data from Sengupta et al. [2016](shared first-author with me); I will quote these papers when writing about the specific fMRI parts. The Hyperalignment was not part of any of these papers. My part in Sengupta et al. [2016] was writing the retinotopy analysis, performing the retinotopy dataset validation analysis, presenting the results, and writing the manuscript. For the other papers [Hanke et al., 2014, 2016], the contribution was quality control for the datasets used for this thesis and contribution to the manuscript. Further details about contributions can be found in the "author contributions" section of these papers [Hanke et al., 2014, 2016; Sengupta et al., 2016].

3.2 Background

3.2.1 Hyperalignment and Connectome-Hyperalignment

3.2.1.1 What is Hyperalignment

Hyperalignment is a type of functional alignment [Haxby et al., 2011]: instead of using spatial structure(al) landmarks, it can use any kind of structure which is congruent across subjects. Here, this "congruent structure" is the normalized time series across all voxels that should be aligned. Hence, instead of using spatial patterns (like anatomy), temporal activation patterns across the voxels' time series are used. Basically, the aim can be the same as for anatomical alignment: transfer different subjects' brain data into the same space.
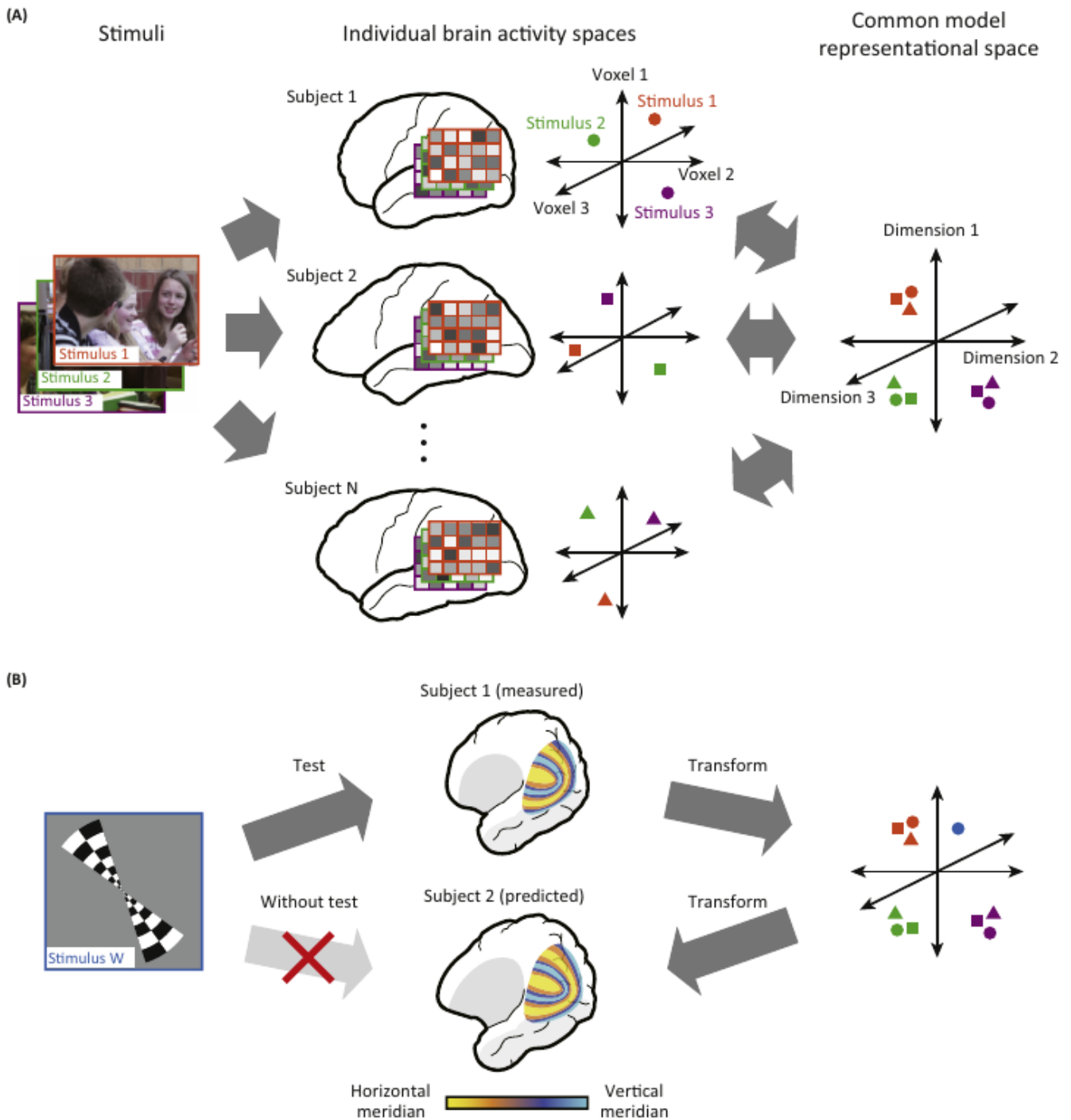
Figure 3.1: "Schematic of Hyperalignment and an Example of its Use. **(A)** Schematic of hyperalignment. Using movie-evoked brain activity, hyperalignment procedure learns subject-wise optimal transformations of brain activity into a common representational space. **(B)** An example of how hyperalignment might be used. Once hyperaligned, the brain activity of one or more subjects can be used to predict the activity of another subject. This allows, for example, the inference of a retinotopic map for a subject without conducting a retinotopic mapping experiment for the subject." [Nishimoto and Nishida, 2016, Figure 1]

Hyperalignment can be used to transfer datasets between subjects (see Figure 3.1). The original Hyperalignment [Haxby et al., 2011] is restricted to the ROI which should be aligned. This means that the activation within this ROI is used to derive the transformation matrix: the transformation matrix is the basis of transformation into a common space and therefore for the transfer onto another subject's space. From Guntupalli et al. [2016]:

"The common model of representational spaces in human cortex consists of a single high-dimensional representational space and individual-specific transformation matrices that are used to derive the space and to project data from individual anatomic spaces into the common model space and, conversely, to project data from the common space into individual anatomic spaces. The model uses hyperalignment to derive the transformation matrices and the common model representational space. We base the derivation of the transformation matrices and the common space on responses to the movie –a complex, naturalistic, dynamic stimulus. Although the algorithm also can be applied to fMRI data from more controlled experiments, we found that a common model based on such data has greatly diminished general validity (Haxby et al. 2011), presumably because, relative to a rich and dynamic naturalistic stimulus, such experiments sample an impoverished range of brain states.

Overview of Algorithm

An individual's transformation matrix rotates that subject's voxel space into the common model representational space (with reflections), and its transpose rotates the common model space back into the individual subject's anatomical voxel space (Haxby et al. 2011). Hyperalignment uses the Procrustes transformation (Schönemann 1966) to derive the optimal rotation parameters that minimize intersubject distances between response vectors for the same stimuli, namely the same timepoints in the movie. Consequently, common model dimensions are weighted sums of individual subjects' voxels. In other words, individual voxels are not simply shuffled or assigned, one-by-one to single common model dimensions.

Derivation of a Common Model Space

To derive a single common representational space, we first hyperalign one subject to a reference subject's representational space. Then, we hyperalign a third subject to the mean response vectors for the first 2 subjects. We then hyperalign each successive subject to the mean vectors for the previously hyperaligned subjects. In a second iteration, we recalculate transformation matrices for each subject to the mean vectors from the first iteration and then recalculate the space of mean vectors. This space is the model space. We then recalculate the transformation matrices for each subject to the mean vectors in this common space. Each dimension is linked to a single location in the reference subject's brain, but the mean response vectors in this space are derived from all subjects and the transformation matrix for the reference subject is not an identity matrix."

The dataset which is used to generate the transformation matrix will further be refereed as the *training dataset.*

3.2.1.2   The Connectome-Hyperalignment

Why Using the Connectome-Hyperalignment

Hyperalignment [Haxby et al., 2011; Guntupalli et al., 2016] seemed to be the method of choice for projecting different kinds of data onto other subjects' brain. Initially, it had the drawback of only using data from the ROI which is chosen to project. The transformation matrix was derived from the activation patterns (time series) of the ROIs' voxel that should be transferred *e.g.*, a V1 ROI. The data to generate the transformation matrix (training dataset) and the data to transfer (*e.g.*, V1 phase maps) need to be congruent in the dimension which should be transfered, here the spatial dimension, meaning the location of the V1 voxels:

Training dataset and transfered dataset derive from the same ROI — *i.e.*, V1 voxels' time series are used to derive the transformation matrix to transfer V1 voxels' time series or activation maps (like phase maps) between subjects.

As a result it is hard to get a transformation matrix with *i.e.*, an audio dataset and transfer a *i.e.*, visual dataset, both using the same (visual) area ROI: here this would mean that V1 ROI is used to generate the transformation matrix because V1 ROI should be transfered. Using a pure audio stimulus to drive the V1 activity is suboptimal because an audio stimulus probably would not elicit a comprehensive activity across subjects in this specific ROI. To overcome this limitation, Florian Baumgartner came up with the idea of the Connectome-Hyperalignment. Usually the "Connectome" in neuroscience is referred as a "map" of neuronal connection in the brain, so what is the Connectome-Hyperalignment?

What Is the Connectome-Hyperalignment

In short, the Connectome-Hyperalignment is Hyperalignment using a Connectome. It takes the whole brain's activation into account, whereas the original Hyperalignment [Haxby et al., 2011] is restricted to the projected ROI [Haxby et al., 2011]. The Connectome-Hyperalignment depends on activity in other parts of the brain that are correlating with the ROI activity. The whole brain activation is ideally evoked by complex stimulation, *e.g.*, a movie. To acquire the correlation of the whole brain's activation, the ideal case would be to correlating every voxel's time series with each of the ROI voxels' time series. Since the resulting matrix is too big to process ($\sim$ 100.000 brain voxel x $\sim$ 4.000 ROI voxel), the number of datapoints needed to be reduced. Therefore, a mask of the gray matter was applied. To reduce the number of brain voxels even further, brain voxels' time series were averaged with voxels in their vicinity, using spheres. These spheres have a certain radius to include a certain vicinity. All voxels which are in this sphere are averaged to become one mean time series. The spheres are defined in their size by their radius in voxels. The bigger

the radius, the bigger the sphere and as a result more voxels are averaged into the mean time series of a sphere. To cover the whole brain, spheres are packed across the whole brain. The end result is a functional Connectome: the correlation matrix of *i.e.*, sphere mean time series and each ROI voxel's activity. The Connectome is used to derive the transformation matrices to transform the subject's data from its anatomical space to the common space and vice versa. Especially the transformation of different conditions should profit from using the Connectome-Hyperalignment because it removes the restriction to analyse only within the ROI. The ROI itself is also limited in its size by the processing power of the used machines.

The Pre-Connectome Hyperalignment is introduced to hyperalign the "Connectome" before using it for the major Connectome which is then used to generate the transformation matrix to functionally align other modalities data, *i.e.*, phase maps.

Limits in Number of Voxels

The number of the subject's ROI voxels to transfer should be less than the number of volumes of the training dataset: It bears the risk of using too many voxels to explain the same activity pattern. Because it has more degrees of freedom to fit, it makes it easier in the first place to fit the different subjects' data into the common space. Hence, across subjects, arbitrarily many different voxels explain the same activity pattern. So, the activity pattern of subjects would be less likely similar to each other. This leads to less distinct transformations from subject to subject, and this results in random alignment of the hyperalignment.

3.2.1.3 What Kind of Stimuli Can Be Used

The ideal training dataset has a complex, whole brain activation. Important is that the activity is comparable across subjects. This comparable activity pattern is needed to make it possible for the hyperalignment algorithm to rotate all different subjects' activity pattern into one pattern. The more similar the activity, the more precise the transformation into the common space. The better the transformation into the common space, the better subject's differences can be coded into this transformation matrix. If the major difference between the subjects is due to different stimulation, here brain activation, the real intersubject difference is more likely to be lost within the transformation between conditions to generate the transformation matrix. In other words: when functionally aligning different conditions into one space, it is difficult to determine if the difference in the result is due to the different conditions or the different subjects' overall brain activity.

Hyperalignment can be used on every kind of functional data if used to transfer different datasets of the same condition to each other [Guntupalli et al., 2016]. For transferring different kind of conditions, the Connectome-Hyperalignment is used. In this study, it is used to generate a phase map of a patient without showing a mapping stimulus. Technically, Hyperalignment can also be used on other multichannel data *e.g.*, from EEG or MEG. The main issue is to transfer the training dataset and the data to transfer into the same (here

spatial) space, *i.e.*, transfer from one subject's data onto another subject's space.

3.2.2   Region of Interest for the Hyperalignment

The presentation of the retinotopic maps onto surface representation is crucial since it is needed to identify, delineate, and select the visual areas. Viewing the volume in slices, *i.e.*, axial, sagital, or coronal view, makes it very difficult to follow the surface and identify the visual areas boundaries at the surface. To compare the outcome from Hyperalignment, here phase maps, no manually delineated ROIs were necessary: basically validation was a within-subject within-voxel comparison. As a result it didn't really matter where the voxels were, as long they were primarily driven by the retinotopic mapping stimulus; the selection of voxels was independent from the visual area they are located in. This does not mean that the information of visual area borders is lost. It is just not used to define the visual areas beforehand.

3.2.3   The Processing Pipeline

For processing a higher number of participants and to run processes in parallel on a computing cluster, an input independent processing pipeline is necessary. Besides this, scripting makes documentation, reproduction, and sharing easier. Furthermore, the analysis should be open source based to share it more easily [Eglen et al., 2016; Halchenko and Hanke, 2015] and spur reuse. To use a computational cluster, a software package is needed which can easily use the resources of the cluster. Since no software package (*i.e.*, *freesurfer*, *fsl*, *AFNI*) has the best tool for every processing step, an ideal processing pipeline should be able to use different tools from different software packages.

Nipype

Nipype [Gorgolewski et al., 2011] is a Python-based, community driven, open-source data processing framework. Nipype offers all of this: open, free, easy interaction with cluster resources via condor-plugin, and possible implementation of different other toolboxes. Condor is a software to distribute calculations on a computational cluster [Thain et al., 2005].

Since Chapter *Functional Alignment: Hyperalignment* was primarily about method improvement, it was necessary to iterate many different variables and rerun the pipeline for each different combination of settings. *Nipype* has the advantage of only recalculating parts of the processing which are affected by a changed variable (or function). This saves a lot of time and memory by not recreating data doubles. The processes of the workflow are automatically split up for best parallel-processing usage.

3.3 Methods

The data used is published and can also be found in Sengupta et al. [2016]; Hanke et al. [2014, 2015].

3.3.1 Participants

Only subjects with complete datasets for retinotopic mapping, audio, and audio-visual movie and a good anatomical alignment between these datasets were used for the study. Coverage and the warping from 7T to 3T data were critical factors here. It resulted in eight right-handed participants (mean age 30.5 years, range 23–39, 4 females). This way it was possible to draw direct comparisons between all 3 datasets in this study. The reason is missing or bad data for either retinotopic mapping, audio, and/or audio-visual movie data. This made it impossible to use these subjects' data for the comparison between all tasks (audio movie, audio-visual movie, and retinotopic mapping). The subjects' IDs, according the given datasets where: 01, 03, 09, 14, 16, 18, 19, 20. The native language of all participants was German. They all reported to have normal hearing without permanent or current temporary impairments and no known history of neurological disorders. No formal test of their hearing capabilities was conducted. All but three participants reported to have seen the movie "Forrest Gump" before at least once. Participants underwent a dedicated ophthalmologic exam to confirm normal vision.

3.3.2 Procedures

3.3.2.1 Audio and Audio-Visual Movie

Movie Segment Presentation

Two types of the Forrest Gump movie were presented: and audio-visual and an audio movie. Both types were divided into eight segments. All eight movie segments were presented individually in chronological order in two sessions of four segments each. Between sessions, participants left the scanner for a break with a flexible duration. On average, participants chose to continue with the second session after approximately 15 min for the audio movie, and for the audio-visual movie approximately 10 min.

Subject Instructions

For the audio and audio-visual movie, participants were instructed to inhibit any physical movements, as best they could, throughout the recording sessions. At the same time, they were informed to feel free to perform eye-movements, if they were so inclined, and that it was not required to maintain fixation or to keep the eyes open. Other than that, participants were instructed to simply "enjoy the movie".

3.3.2.2   Retinotopic Mapping

Participants performed four acquisition runs in a single session with a total duration of 12 min, with short breaks in-between and without moving out of the scanner. In each run, participants performed the center letter reading task while passively watching the contracting, counter-clockwise rotating, expanding, and clockwise rotating stimuli in exactly this sequential order.

3.3.3   Stimulus

3.3.3.1   Audio Movie

Stimulus

Participants listened to a German audio-description (Koop, Michalski, Beckmann, Meinhardt & Benecke produced by Bayrischer Rundfunk, 2009) of the movie "Forrest Gump" (R. Zemeckis, Paramount Pictures, 1994) as broadcast as an additional audio track for visually impaired listeners on Swiss public television. The audio content is largely identical to the dubbed German soundtrack of the movie except for interspersed narrations by a male speaker who describes the visual content of a scene. These descriptions take place when there is no dialog, off-screen speech, or other relevant audio-content in the movie. During narrations, the volume of the original soundtrack is reduced so that they are clearly audible. To aid reproducibility and further analysis, the audio description soundtrack was temporally aligned to the audio track of the "Forrest Gump" DVD release (Paramount Home Entertainment, Germany, 2002; PAL video, DE103519SV) by shifting the audio description to match waveform envelope shapes in Audacity [Audacity developers, 2012]. For this purpose, the audio track of the DVD was extracted using the Handbrake software [Handbreak team, 2012] and, together with the audio description, both were converted into the "Free Lossless Audio Codec" [Coalson, 2007] while down-mixing multi-channel audio to stereo.

Stimulation Setup

Participants listened to the movie stimulus using custom-built in-ear headphones. In order to maximize participants' comfort in the narrow head coil and maintain a high audio quality, the headphones use a combination of electrostatic loudspeakers (HP-M01, MR confon GmbH, Magdeburg, Germany) located just outside the head coil, a short air-conducting part consisting of a funnel-like adapter, and an approximately 15 cm long tube that connected a speaker with a communication earplug (Peltor HearPlug, PELTIP1-1, ≈25 db attenuation). This setup significantly reduces the pressure on the auricles, thus avoiding the pain often experienced during imaging sessions and consequently helped participants maintain a steady head position. Headphones were driven by an MR confon mkII+ fed from a Aureon 7.1 USB (Terratec) sound card through an optical connection. Visual instructions were

presented with an LCD projector (DLA-G150CL, JVC Ltd.) on a rear-projection screen positioned behind the head coil within the magnetic bore. Participants viewed the screen through a mirror attached to the head coil. During the functional scans, the projector presented a medium gray screen with the primary purpose to illuminate a participant's visual field in order to prevent premature fatigue. The screen contained a solid black "fixation" dot that faded in and out at the beginning and end of a movie segment.

Stimulus presentation and response logging were implemented using PsychoPy [Peirce, 2007]. The source code of the complete implementation of the experiment is available as supplementary material in Hanke et al. [2014].

3.3.3.2 Audio-Visual Movie

Stimulation Setup

Visual stimuli were presented on a rear-projection screen inside the bore of the magnet using an LCD projector (JVC DLA RS66E, JVC Ltd., light transmission reduced to 13.7% with a gray filter) connected to the stimulus computer via a DVI extender system (Gefen EXT-DVI-142DLN with EXT-DVI-FM1000). The screen dimensions were 26.5 cm×21.2 cm at a resolution of 1280×1024 px with a 60 Hz video refresh rate. The binocular stimulation were presented to the participants through a front-reflective mirror mounted on top of the head coil. The movie was shown at a viewing distance of 63 cm in 720p resolution at full width on a 1280×1024 pixel screen that was 26.5 cm wide — corresponding to 23.75° × 13.5° of visual angle or 23.75° × 10.25° when considering only the movie content and excluding the horizontal gray bars. Stimulation was implemented with PsychoPy v1.79 on the (Neuro)Debian operating system [Halchenko and Hanke, 2012]. Participant responses were collected by a two-button keypad and was also logged on the stimulus computer.

Stimulus

Participants watched and listened to the movie "Forrest Gump" (R. Zemeckis, Paramount Pictures, 1994, dubbed German soundtrack). The stimulus source was the commercially available high-resolution Blu-ray disk release of the movie from 2011 (EAN: 4010884250916). Temporal alignment of the movie with the previously used[Hanke et al., 2014] DVD release was manually verified by audio waveform matching in order to guarantee synchronous stimulus time series between studies. The video track of the Blu-ray was extracted, re-encoded as H.264 video (1280×720 at 25 fps), and muxed with the DVD's dubbed German soundtrack using the MLT Multimedia Framework [Yates and Dennedy, 2012].

3.3.3.3 Retinotopic Mapping

The stimulation setup was the same as for the audio-visual movie. Similar to previous studies [Engel et al., 1997; Sereno et al., 1995], traveling wave stimuli were designed to encode visual field representations in the brain using temporal activation patterns [Warnking

et al., 2002]. Expanding/contracting rings and clockwise/counter-clockwise wedges (see Figure3.2A) consisting of flickering radial checkerboards (flickering frequency of 5 Hz) were displayed on a gray background (mean luminance $\approx 100\,cd/m^2$) to map eccentricity and polar angle. The total run time for each eccentricity and polar angle stimuli was 180 s, comprising five seamless stimulus cycles of 32 s duration each along with 4 s and 16 s of task-only periods (no checkerboard stimuli) respectively at the start and the end.

The flickering checkerboard stimuli had adjacent patches of pseudo-randomly chosen colors, with pairwise euclidean distances in the *Lab* color space (quantifying relative perceptual differences between any two colors) of at least 40. Each of these colored patches were plaided with a set of radially moving points. To improve the perceived contrast, the points were either black or white depending on the color of the patch on which the points were located. The lifetime of these points was set to 0.4 s, a new point at a random location was initialized after that. With every flicker, the color of the patches changed to its complementary luminance. Simultaneously, the color changed and the direction of movement of the plaided points also reversed.

Eccentricity encoding was implemented by a concentric flickering ring expanding and contracting across the visual field (0.95 ° of visual angle in width). The ring was not scaled with cortical magnification factor. The concentric ring traveled across the visual field in 16 equal steps, stimulating every location in the visual field for 2 s. After each cycle, the expanding or the contracting rings were replaced by new rings at the center or the periphery respectively.

Polar angle encoding was implemented by a single moving wedge (clockwise and counter-clockwise direction). The opening angle of the wedge was 22.5 °. Similar to the eccentricity stimuli, every location in the visual field was stimulated for 2 s before the wedge was moved to the next position.

Center Letter Reading Task

In order to keep the participants' attention focused and to minimize eye-movements, they performed a reading task. A black circle (radius 0.4°) was presented as a fixation point at the center of the screen, superimposed on the main stimulus. Within this circle, a randomly selected excerpt of song lyrics was shown as a stream of single letters (0.5° height, letter frequency 1.5 Hz, 85% duty cycle) throughout the entire length of a run. Participants had to fixate, as they were unable to perform the reading task otherwise. After each acquisition run, participants were presented with a question related to the previously read text. They were given two probable answers, to which they replied by corresponding button press (index or middle finger of their right hand). These question only served the purpose of keep participants attentive — and was otherwise irrelevant. The correctness of the responses was not evaluated.

3.3.4 Data Acquisition

3.3.4.1 Audio Movie

$T2^*$-weighted echo-planar images (gradient-echo, 2 s Repetition Time (TR), 22 ms echo time, 0.78 ms echo spacing, 1488 Hz/Px bandwidth, generalized autocalibrating partially parallel acquisition (GRAPPA) acceleration factor 3, 24 Hz/Px bandwidth in phase encoding direction) were acquired during stimulation using a whole-body 7 Tesla Siemens MAGNETOM magnetic resonance scanner equipped with a local circularly polarized head transmit and a 32 channel brain receive coil (Nova Medical, Inc., Wilmington, MA, USA). 36 axial slices (thickness 1.4 mm, 1.4 × 1.4 mm in-plane resolution, 224 mm FOV, anterior-to-posterior phase encoding direction) with a 10% inter-slice gap were recorded in ascending order. This configuration represents a good compromise between spatial resolution, volume coverage, and volume acquisition time. include the ventral portions of frontal and occipital cortex while minimizing intersection with the eyeballs. The field-of-view was centered on the approximate location of Heschl's gyrus. Slice orientation was manually configured for the first pilot recording session only. Subsequent sessions for all participants were automatically aligned to this setup by the scanner software (auto align) using skull and brain landmarks identified from a short 3D scout scan (1.6 mm isotropic resolution, 14 s duration).

For the audio-visual movie the number of volumes acquired per movie segment was 451, 441, 438, 488, 462, 439, 542, and 338 volumes (for movie segments 1–8 respectively), and was therefore identical to the audio-visual movie. All 8 movie segments were used for the Hyperalignment.

3.3.4.2 Audio-Visual Movie and Retinotopic mapping

$T2^*$-weighted echo-planar images (gradient-echo, 2 s TR, 30 ms echo time, 90 ° flip angle, 1943 Hz/Px bandwidth, parallel acquisition with sensitivity encoding (SENSE) reduction factor 2) were acquired during stimulation using a whole-body 3 Tesla Philips Achieva dStream MRI scanner equipped with a 32 channel head coil. 35 axial slices (thickness 3.0 mm) with 80×80 voxels (3.0×3.0 mm) of in-plane resolution, 240 mm FOV, anterior-to-posterior phase encoding direction) with a 10% inter-slice gap were recorded in ascending order — practically covering the whole brain. Philips' "SmartExam" was used to automatically position slices in AC-PC orientation such that the topmost slice was located at the superior edge of the brain. For the retinotopic mapping experiment, 90 volumes of fMRI data were acquired for each run. All scans from the retinotopic mapping were used for the Hyperalignment: contracting and expanding ring, and clockwise and counter-clockwise wedge stimulus. Each condition was measured once.

3.3.4.3   Anatomy

Structural MRI Data Acquisition

The anatomical data was recorded at the 3 Tesla Philips Achieva equipped with a 32 channel head coil using standard clinical acquisition protocols. An image with 274 sagital slices (FOV 191.8 × 256 × 256 mm) and an acquisition voxel size of 0.7 mm with a 384 × 384 in-plane reconstruction matrix (0.67 mm isotropic resolution) was recorded using a 3D Turbo Field Echo (TFE) sequence (TR 2500 ms, Inversion Time (TI) 900 ms, flip angle 8°, Echo Time (TE) 5.7 ms, bandwidth 144.4 Hz/px, Sense reduction AP 1.2, RL 2.0, scan duration 12:49 min).

3.3.5   Preprocessing

For the preprocessing procedures, code from Hanke et al. [2014] was used.

3.3.5.1   Retinotopic Mapping Analysis

Many Regions Of Interest (ROI) in the human visual system follow a retinotopic organization [Sereno et al., 1995; Engel et al., 1994, 1997]. The primary areas like V1 and V2 are also provided as labels with the Freesurfer segmentation using the `recon-all` pipeline [Dale et al., 1999]. But the higher visual areas (V3, VO, PHC, etc) need to be localized by retinotopic mapping [Sereno et al., 2012; Arcaro et al., 2009; Wandell et al., 2007; Silver and Kastner, 2009] or probability maps [Wang et al., 2014; Van Essen et al., 2001].

We implemented a standard analysis pipeline for the acquired fMRI data based on standard algorithms publicly available in the software packages Freesurfer [Dale et al., 1999], FSL [Smith et al., 2004], and AFNI [Cox, 1996]. All analysis steps were performed on a computer running the (Neuro)Debian operating system [Halchenko and Hanke, 2012], and all necessary software packages (except for Freesurfer) were obtained from system software package repositories.

BOLD images time series for all scans of the retinotopic mapping paradigm were brain-extracted using FSL's BET and aligned (rigid-body transformation) to a participant-specific BOLD template image. All volumetric analysis was performed in this image space. An additional rigid-body transformation was computed to align the BOLD template image to the previously published cortical surface reconstructions based on T1 and T2-weighted structural images of the respective participants [Hanke et al., 2014] for later delineation of visual areas on the cortical surface. Using AFNI tools, time series images were also "deobliqued" (`3dWarp`), slice time corrected (`3dTshift`), and temporally bandpass-filtered (`3dBandpass` cutoff frequencies set to 0.667/32 Hz and 2/32 Hz, where 32 s is the period of both the ring and the wedge stimulus).

For angle map estimation, AFNI's `waver` command was used to create an ideal response time series waveform based on the design of the stimulus. The bandpass filtered BOLD images were then processed by the `3dRetinoPhase` (`DELAY` phase estimation method was based

on the response time series model). Expanding and contracting rings, as well as clockwise and counter-clockwise wedge stimuli, were jointly used to generate average volumetric phase maps representing eccentricity and polar angles for each participant and neutralize phase shifts introduced by hemodynamic delays. Polar angle maps were adjusted for a shift in the starting position of the wedge stimulus compared between the two rotation directions. The phase angle representations, relative to the visual field, are shown in Figure 3.2A. As an overall indicator of mapping quality, Figure 3.2B shows the distribution of the polar angle representations across all voxels in the MNI occipital lobe mask combined for all participants.

For visualization and subsequent delineation, all volumetric angle maps (after correction) were projected onto the cortical surface mesh of the respective participant using Freesurfer's `mri_vol2surf` command — separately for each hemisphere. In order to illustrate the quality of the angle maps, the subjectively best, average, and worst participants (respectively: participant 1, 10, and 9) have been selected on the basis of visual inspection. Figure 3.2C shows the eccentricity maps on the left panel and the polar angle maps for both hemispheres on the right panel. A table summarizing the results of the manual inspections of all surface maps can be found in the appendix (7.3) and is available at github.com/psychoinformatics-de/studyforrest-data-retinotopy/qa. Delineations of the visual areas depicted in Figure 3.2C were derived according to **Kaule** et al. [2014]. Further details on the delineation procedure can be found in Arcaro et al. [2009]; Wandell et al. [2007]; Silver and Kastner [2009].
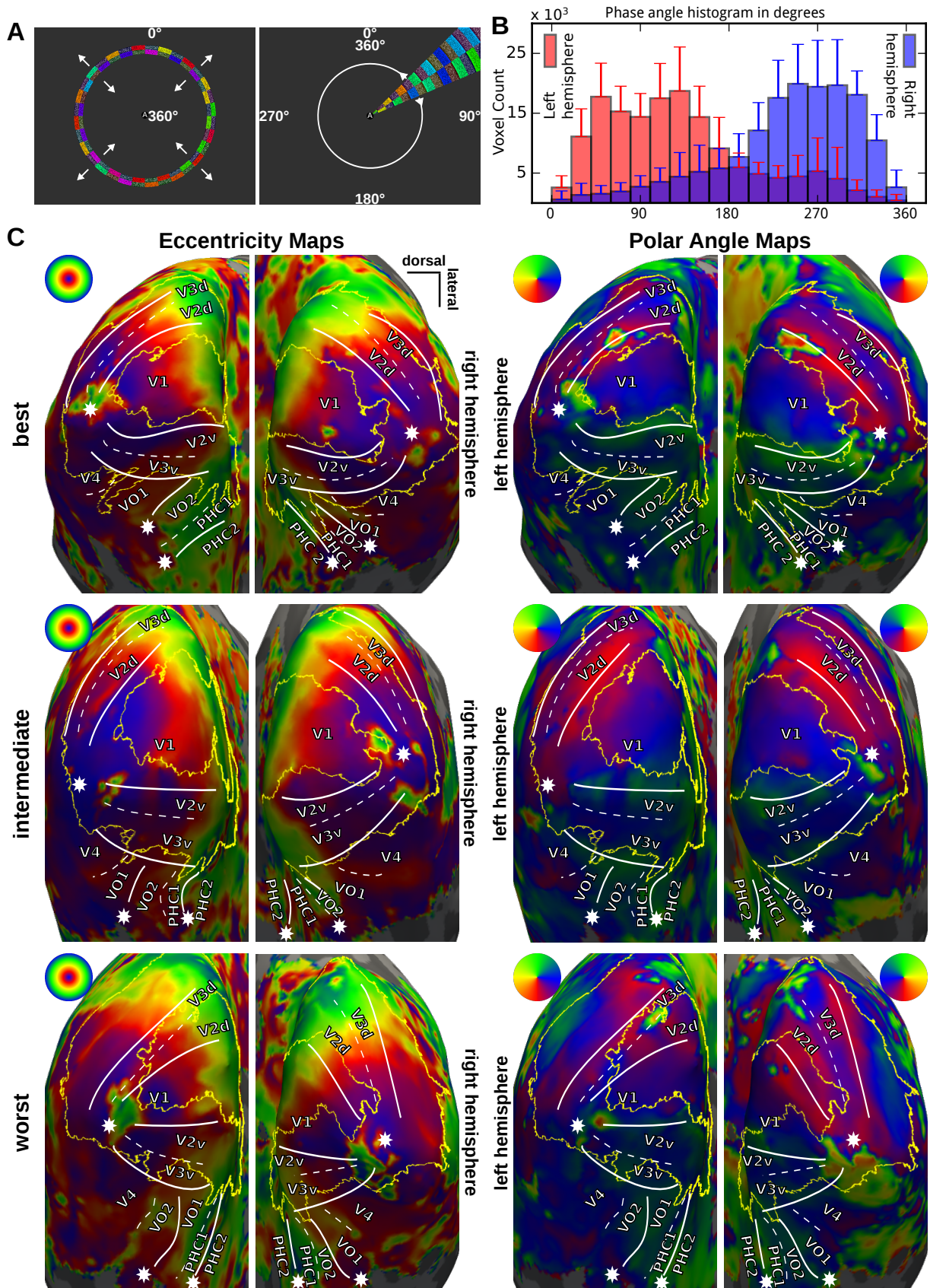
Figure 3.2: (A) Ring and wedge stimuli with continuous central letter reading task to encourage fixation. White numbers indicate the respective phase angle encoding. (B) Histogram of polar angles for all voxels in the MNI occipital lobe mask for the left and right hemisphere. Error bars indicate standard deviation across all subjects. (C) Inflated occipital cortex surface maps for eccentricity and polar angle for the best, intermediate, and worst participants: participants 1, 10, and 9 respectively. White lines indicate manually delineated visual area boundaries; stars mark the center of the visual field; yellow lines depict the outline of the autogenerated Freesurfer V2 label[Hanke et al., 2014] for comparison. All maps are constrained to the MNI occipital lobe mask.

3.3.5.2 Audio and Audio-Visual Movie

The data were spatially smoothed using FSL [Smith et al., 2004] SUSAN (brightness threshold 180; fwhm 8 mm). Additional temporal smoothing was done using AFNI [Cox, 1996] 3dBandpass (highpass: 1/150 Hz, lowpass: 1/9 Hz). From the audio-visual movie data, the grand mean were removed using a custom Python-script. The leading and last 4 volumes of each scan were cut to avoid overlap of the scans and give enough onset time of the BOLD [Hanke et al., 2014].

3.3.5.3 Anatomical Alignment - Group templates

The generation of the templates and the alignment between and within subjects was done via Nipype as follows:

1. Choosing a subject's brain as the initial reference template. The subject's brain most similar to all other subjects brain was chosen.

2. Linearly coregister all the subjects to the template reference. The average out of those was the reference template for the next step.

3. Again, linearly coregistered all the subjects to the template reference. The average out of those was the reference template for the next step.

4. Non-linearly coregistered all the subjects to the template reference. The average out of those was the reference template for the next step.

5. Again, non-linearly coregistered all the subjects to the template reference.

6. Concatenated all the coregistration matrices from all previous steps into one coregistration matrix.

7. Applied the coregistration matrix of every subject to bring every subject's data into the group-template space. In group-template space the subjects were anatomically aligned.

3.3.5.4 Voxels Selection

With each phase map came a coherence threshold map given by AFNIs 3dRetinoPhase [Cox, 1996]. This threshold map was used for further voxel selection, using a lower boundary of 0.5. This threshold mask, the gray-matter mask, and the brainmask were used to mask the whole brain data. These voxels were used for further analysis.

3.3.6　Anatomical Alignment - Analysis

As a reference for Hyperalignment, anatomical alignment was done. Reference in sense of alignment: anatomical alignment is based on structural patterns, whereas Hyperalignment is based on temporal or functional patterns. For many studies the transformation into MNI-space as a common anatomical space is usual. To determine the correlation distance between all subjects in group-space, the following steps were performed:

1. Generated a sum mask in anatomical space across all subjects. (This was necessary to produce the same shape for all subjects.)

2. Averaged all subjects except the target-subject (Leave-1-out).

3. Removed voxels with zero variance from the averaged dataset.

4. Calculated the correlation distance between just generated average dataset and the target-subject's data. Since the correlation process was the same also for the hyper-alignment validation, it is explained with more detail in the later Section see 3.3.9, p.51.

All function were implemented using custom-made Python scripts run within the Nipype processing pipeline.

3.3.7　Application of Hyperalignment

Hyperalignment was done using the algorithm from Haxby et al. [2011]. The initial reference subject is chosen to be the subject with the biggest ROI *i.e.*, biggest number of voxel. The transformation matrix was generated subject-wise, separately using three different training datasets: retinotopic maps, audio movie data, audio-visual movie data. To transfer (hyper-align) data into another subject's space, here referred as "target-subject", the steps of the Hyperalignment processing were the following:

1. Rotating (/trained) the functional spaces of the subjects, excluding the target-subject

2. Generate the transformation matrix for every subject

3. Use this transformation matrix to transform all subjects' phase maps into common space

4. Generate the mean of the phase maps in *common space* across the subjects, excluding the target-subject

5. Use the subject-specific transformation matrix of the target-subject to bring all other subjects from *common space* into the target-subject's space

6. Validation

The hyperalign algorithm itself was already integrated into PyMVPA [Hanke et al., 2009] and was implemented into my Nipype processing pipeline.

3.3.8   Extending the Hyperalignment - the Connectome-Hyperalignment

To generate the Connectome, the brain was subdivided into close-packed hexagonal spheres using a script from Florian Baumgartner. The radius of the spheres was 2 voxel. For every sphere, the time series of all voxels inside a sphere were averaged. For every subject, every mean time series was then correlated with each ROI voxels' time series. The resulting correlation matrix (shape: "number of Spheres" × "number of ROI voxels') is the Connectome. The Connectome represents the whole pattern of cortical activation in relation to the ROI voxels'. The more complex the brain's activation of the Connectome dataset is, the more other conditions can be described by the activation pattern of this ROI. In these terms a stimulus like an audio-visual movie is a more "complex" stimulus, than a block-design on/off-full-field checkerboard pattern stimulus.

3.3.8.1   Pre-Connectome-Hyperalignment

The Pre-Connectome is a more complex Connectome. According Figure 3.3, the basic Connectome was performed by:

(1-) Directly generating the Connectome by correlating the sphere mean time series with the ROI's voxels' time series.

The Pre-Connectome was generated using more steps: Basically it transfers the pure Connectome (using the hyperalignment algorithm) into the common space. Then this "Connectome in common space" is used as the basis to generate a new Connectome. In the end, it is a Connectome generated out of a common space, as also shown in Figure 3.3:

(1+) Averaging the sphere time series across all subjects in anatomical space (black arrow).

(2) Correlating each of these mean time series (black) with each subject's ROI's voxel time series separately. The resulting correlation matrix was the Pre-Connectome.

(3) Bringing the Connectome of all except the target-subject into the common space.

(4) Generating the transformation matrix for all subjects.

(5) Using this transformation matrix to transform all subjects' Pre-Connectome into common space, using the hyperalignment algorithm.

(6) Correlating the Pre-Connectome in common space with each ROI's voxel time series to generate the Connectome.
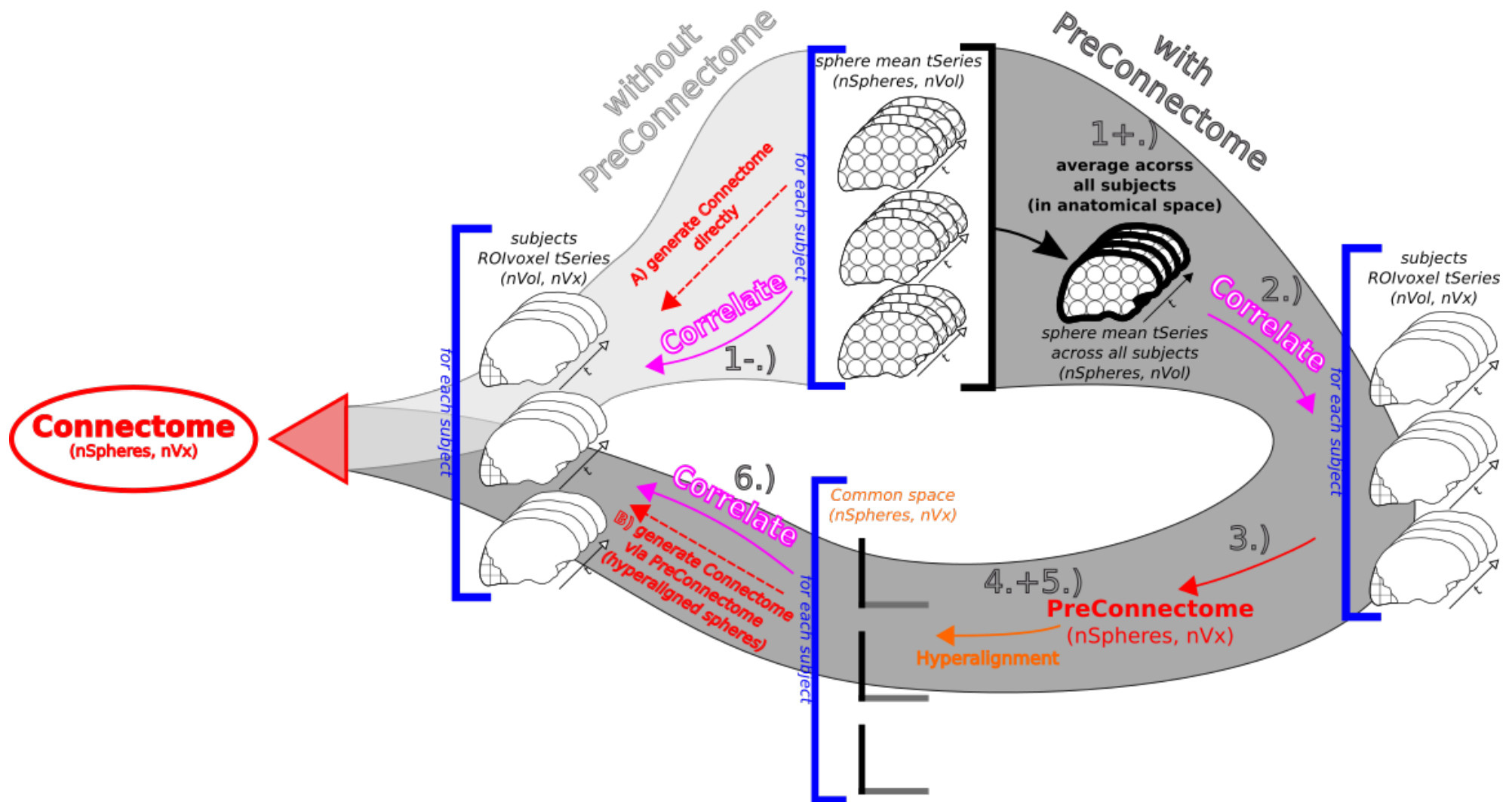
Figure 3.3: Shown are the two routes to generate the Connectome: without (light gray stream to the left) or with Pre-Connectome (dark gray stream to the right). Same colors indicate same algorithms (correlation, transformation) or iterators (*e.g.*, subjects, spheres) used. For each step, the shape of the resulting output matrix is written in brackets underneath. Detailed description of steps 1+ -6 and 1- can be found in *Pre-Connectome-Hyperalignment* (see 3.3.8.1, p.49). Furthermore, the blue square bracket indicates that the operation is done for each subject separately. The black square bracket indicates averages across all subjects.

3.3.9 Validation

For the phase maps of the retinotopy, the phase values were in a range of 0 to 360° for eccentricity and 0 to 180 and 180 to 360° for polar angle for the left and right hemisphere, respectively. These phase values cannot be aligned by Hyperalignment since they have no basis for the procrustean transformation to rotate around. Also, to compare polar angles of 0 and 360°, circular statistics were needed.

To account for both: converting single degree phase angles and circular statistics easier, each phase value was transfered into a number of cosine values of a cosine wave (namely 10). Each phase value was coded into the phase shift of this cosine wave [Guntupalli et al., 2016]. To convert the phase value (one for each voxel), following steps ware made:

1. The phase value was transformed from degree to radiant

2. Distributed every single radiant value across the channels (here 10) values of cosine:

$$value\left(channel\right) = \cos\left(ph + \left(\frac{channel * 2\pi}{nChannel}\right)\right); 0 \leq channel \leq nChannel \quad (3.1)$$

   Iteration across *channel*, with *nChannel* being number of Channels (here 10) and *ph* being the phase value to transform.

The validation was done by correlating each of the transfered phase maps with the phase map of the target-subject. There is a difference between the correlation values of eccentricity and polar angle values due to the fact that polar angle data are circular and eccentricity data are not. For correlation analysis, the hyperalignment-transfered channel-values were converted back into single values. The back-converted values were then correlated with the target-subject's values. For polar angles, the single phase values were transformed into circular values (cosine values) beforehand. This was necessary because only polar angle representations are circular.

An example of possible results is given in Figure 3.4: Due to the cortical magnification factor, the bar plots show a higher voxel count around 360°, the foveal representation. The histograms show a similar distribution for the x and y-axis for bad and good transformation. For "bad", these voxels represent different phase values, as a result the correlation distance is much bigger. The given correlation distance is therefore given and is 1-correlation. The confidence interval is calculated using bootstrap with 10000 re-samples. The overlays "good" and "target" look quite similar. Due to its bad transformation, "bad" looks different: more noisy. The "bad" overlay is done using a hyperalignment transformation matrix, obtained using the audio movie. The "good" overlay is done using a hyperalignment transformation matrix, obtained using the retinotopic mapping data.
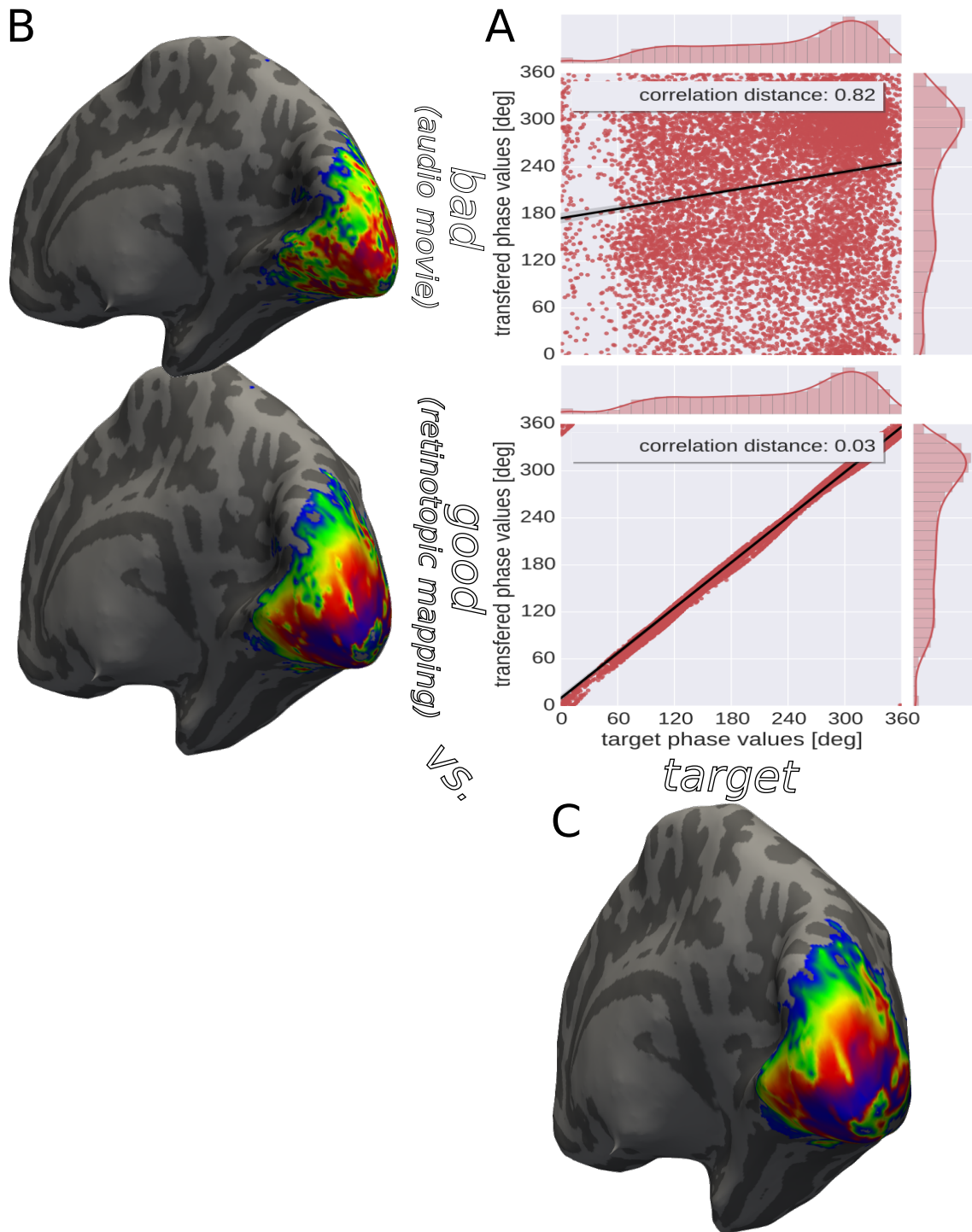
Figure 3.4: Example of a bad and a good transformation of eccentricity representation on right hemisphere, exemplary demonstrated with subject 16 overlays. Important: The Plots show the average data over all subjects, details in Section Results. **(A) The plots:** The x-axis represents the phase representation of each target-subject's voxel in the target-subject's space. The y-axes represents the phase representation of each transfered voxel in the target-subjects' space. Each plots shows the relationship between transfered and target-subjects' phase values. If every transfered voxel has the same phase value as the target-subjects' voxel, a straight diagonal would be visible (as closely in good vs. target). The broader the distribution of points, the worse the transformation. The dark black line represents a linear fit across all the points with its 99% bootstrapped confidence interval (gray shade, 10000 iterations). Additionally the correlation distance is given. The histograms shows how many voxels represent the corresponding phase value. The area around 360° is the foveal representation. The finer the bins, the more equal the distribution of voxels across the phases: big bins indicate strongly agglomerated phase representations. **(B+C) The brain surface overlays:** According to the plot axes, they show overlays of the eccentricity representations on the target-subject's brain surface.

3.4 Results

Subjects' data were aligned into a common group space using anatomical alignment procedures (*Anatomical Alignment - Analysis* (see 3.3.6, p.48)). The phase maps of the subjects were then correlated with each other. The transfered and the training datasets have to be anatomically aligned inside each target-subject's space. The target-subject's space here refers to the anatomical space of the subject. The better the functional data are aligned to each other, the smaller the correlation distance. Anatomical alignment leads to a mean correlation distance of 0.22 for eccentricity and 0.29 for polar angle.

Using the original Hyperalignment algorithm from [Haxby et al., 2011] led to quite different results, depending on which training dataset used (see Table 3.1, 3.2). To improve the Hyperalignment, the Connectome-Hyperalignment and Pre-Connectome-Hyperalignment was introduced. The phase values from retinotopic mapping were transfered, using three different training datasets: retinotopic mapping data, audio-visual movie data, and audio-movie data (see Table 3.1 and 3.2). A summary of the values with all methods used for alignment (normal hyperalignment, hyperalignment with Connectome (Connectome-Hyperalignment), hyperalignment with Pre-Connectome (Pre-Connectome-Hyperalignment), and anatomical alignment) are illustrated in figures 3.5-3.8: All subjects, except the target subject, are averaged and then compared to the target subject (leave-1-out). This is done for every subject being the target subject once. The plots show the average across all these comparisons. In figures 3.7 and 3.8, voxels outside the ideal diagonal can be found at (360,0) and (0,360) can be found. They reflect voxels which have phase values just slightly shifted at the $0 - 360°$ border by the alignment process. The influence on correlation distance is much bigger for eccentricity than for polar angles because polar angle values are circular and eccentricity values are not. An example of transfered phase maps can be found in Figure 3.6. It shows that the anatomical alignment gives the least patchy phase maps. The anatomical alignment has a better occipital coverage of the phase maps, which are present in the target-subject's dataset. That means that the anatomical alignment loses subject-specific features compared to hyperaligned phase maps. The phase maps of the audio-movie are the most dissimilar among the phase maps shown.

Summarized, the figures 3.5-3.8 and tables 3.1-3.2 show that hyperalignment using the retinotopic mapping as training dataset gives the best results (smallest correlation distances). For hyperalignment, retinotopic mapping gives the best training dataset, followed by the audio-visual movie, and the worst results with the audio-movie as a training dataset. Plots from left hemisphere data can be found in the appendix (figures 7.1 & 7.2).

Table 3.1: Overview eccentricity: correlation distance comparing aligned phase maps between target and aligned phase values, mean across hemispheres. For anatomical alignment, no hyperalignment was done, hence only retinotopy data was aligned. Accordingly, anatomical alignment has just one value for doing anatomical alignment using the anatomy. For hyperalignment, no anatomical alignment was done, as a result this line stays empty.

	Connectome	Pre-Connectome	normal Hyperalignment	Anatomical Alignment
Retinotopy	0.08	0.20	0.09	
Audio-visual movie	0.44	0.42	0.54	
Audio-movie	0.93	0.88	0.95	
Anatomy				0.22

Table 3.2: Overview polar angles: correlation distance comparing aligned phase maps between target and aligned phase values, mean across hemispheres. For anatomical alignment, no hyperalignment was done, hence only retinotopy data was aligned. Accordingly, anatomical alignment has just one value for doing anatomical alignment using the anatomy. For hyperalignment, no anatomical alignment was done, as a result this line stays empty.

|	Connectome	Pre-Connectome	normal Hyperalignment	Anatomical Alignment
Retinotopy	0.00	0.00	0.00	
Audio-visual movie	0.21	0.18	0.16	
Audio-movie	0.81	0.60	0.75	
Anatomy				0.29
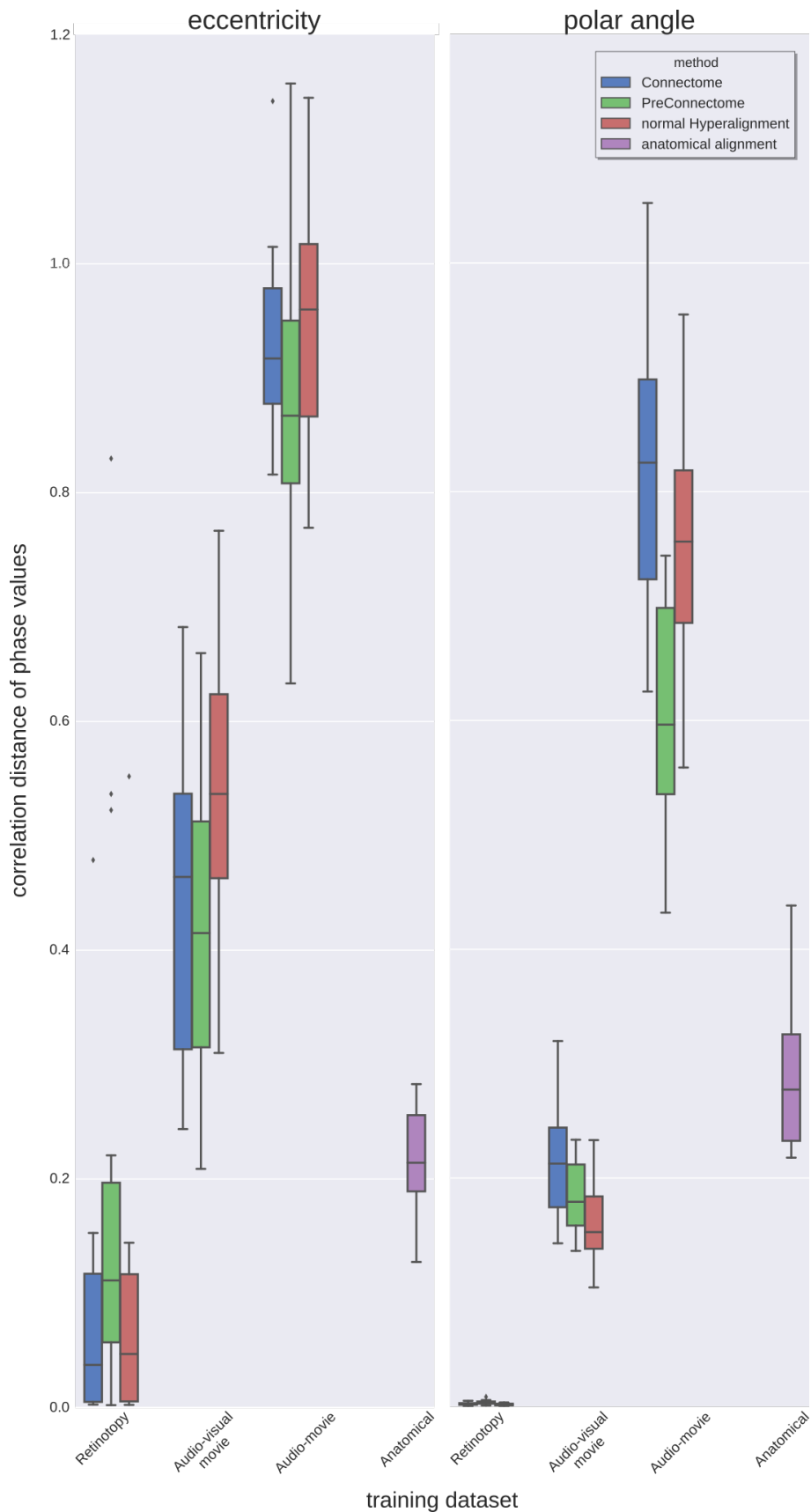
Figure 3.5: Boxcar plot of correlation distances across subjects and hemispheres: Correlation distance between target-subject's phase values and transferred phase values, using different training datasets. Also the results using different methods (Connectome-Hyperalignment, Pre-Connectome-Hyperalignment, "normal" Hyperalignment, and anatomical alignment). The error bars indicate 99% bootstrapped confidence interval (10000 iterations). Outliers are indicated by dots.
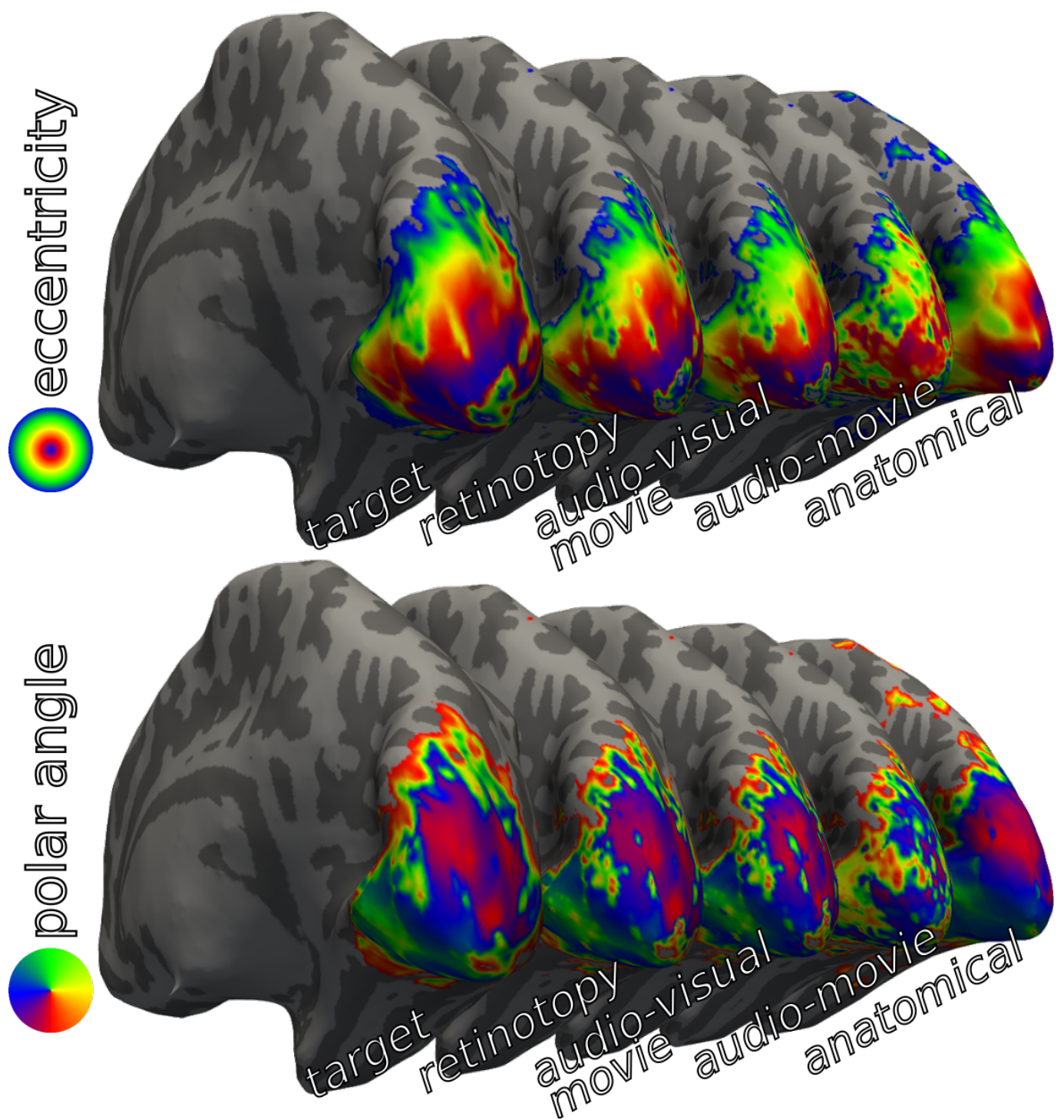
Figure 3.6: Example of transferred phase values on target-subject's surface (right hemisphere, subject 16): using normal hyperalignment, without any Connectome-Hyperalignment. Masking to visual cortex ROI by coherence threshold of 0.5 (see 3.3.5.4, p.47). From left to right: target-subject's data, followed by the results using the different training datasets: retinotopic mapping, audio-visual movie, audio-movie data, and at the very right the result of anatomical alignment. upper: eccentricity maps, lower: polar angle maps, colorkey accordingly. For quality comparison with figures 3.7 and 3.8, see explanation at Figure 3.4.
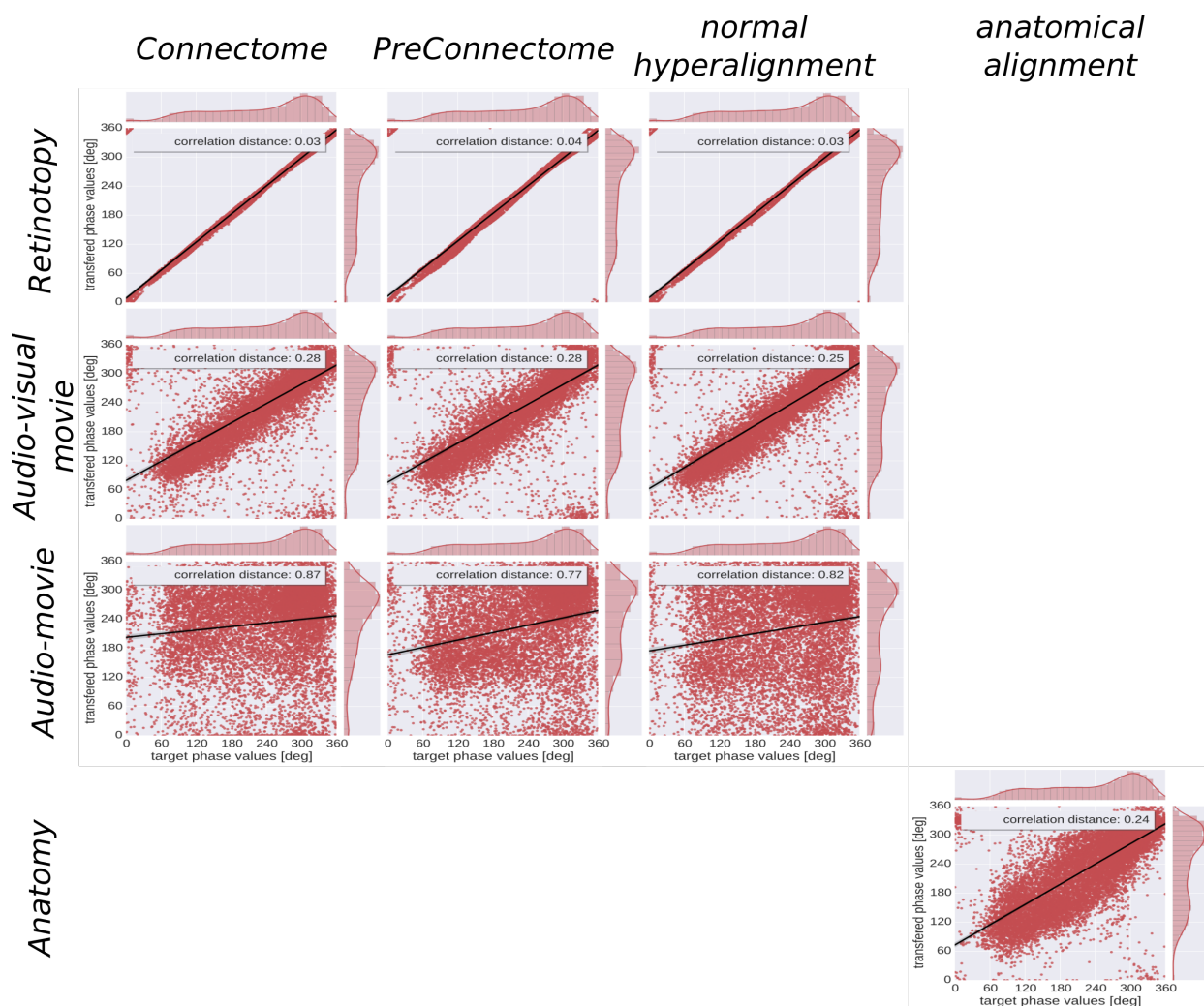
Figure 3.7: Eccentricity phase representations for for different methods and used datasets, as in Figure 3.4, shown for the right hemisphere, too. Rows: different origins (training datasets) of the transformation matrix; columns: methods used to generate the transformation matrix.

3.5 Discussion

3.5.1 Overall Conclusions

General Results

Correlation distance depends primarily on the training dataset: Retinotopic mapping data provide the best result, followed by audio-visual movie, and audio-movie (see Figure 3.5). Excluding the anatomical alignment, the polar angle gives a smaller correlation distance than the eccentricity representations. This is probably due to the fact that the only polar angle correlation distance is calculated using circular statistics. Circular statistics were used because the polar angle representations are circular, whereas 0 and 360° represent the same polar angle. Eccentricity values of 0 and 360° go from periphery to center. As a result 0 and 360° are not close to each other in terms of eccentricity phase angle. Circular
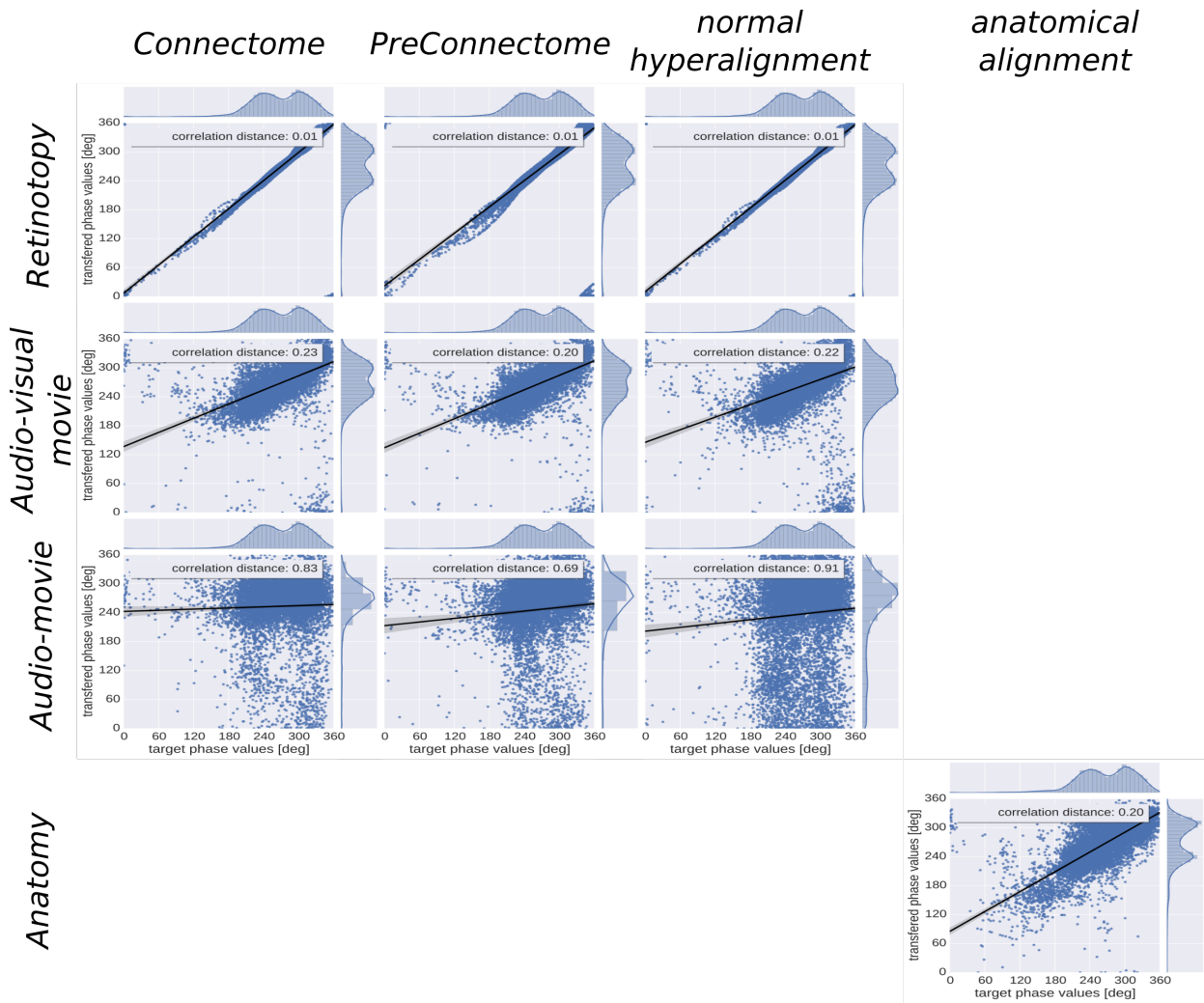
Figure 3.8: Polar angle phase representations for different methods and used datasets, as in Figure 3.4, shown for the right hemisphere, too. As a result polar angle ranges mostly for 180 to 360° (see also Figure 3.2B). rows: different origins (training datasets) of the transformation matrix; columns: methods used to generate the transformation matrix.

statistics are more resilient to small phase shifts around 360 and 0° so the correlation distance of eccentricities is influenced by small phase shift in the realm. Therefore, applying circular statistics to eccentricity representations would lead to false impressions for big correlations: If the periphery or center visual field is represented *e.g.*, at the occipital pole, it would not make a big difference in correlation but it would make a big difference in the retinotopic eccentricity representation. Since anatomical alignment happens without transformation into the common space, no shifts by back-transformation in subject's space appear. Accordingly anatomical alignment is less prone to small shifts around 360 and 0° in eccentricity. Therefore the difference between eccentricity and polar angle is not as big as by hyperalignment. The large confidence interval for eccentricity is probably due to small shifts around 0 and 360° in the transformation process. For the audio-movie, the Pre-Connectome-Hyperalignment shows better results than the normal hyperalignment or the Connectome-Hyperalignment used (see green bars in Figure 3.5). Since the eyes of the

subject were not uniformly open or closed across subjects, during the audio-movie and they were allowed to freely viewing, an additional noise source was introduced. Closed eyes may have led to better hyperalignment results since the brain activity might have been different between the subjects.

Different Scanners

It is important to mention that the usage of the audio-visual movie was easier since the retinotopic mapping and the movie were recorded in the same scanner. The audio-data are from a very different field strength and thus scanner, *i.e.*, 3T Phillips vs 7T Siemens. In the alignment process, the voxels' resolution was transfered into 2.5 mm isotropic voxels, but the initial resolution was different between the scanners: 3 mm isotropic voxels with 10% inter-slice gap at 3T and 1.4 mm isotropic voxels with 10% inter-slice gap. Especially the alignment between T2∗ datasets relies on proper unwarping of the scanner specific magnetic field distortions. Hence the different scanners where audio-movie and retinotopic mapping were collected, might be another influence on worse hyperalignment using the audio-movie. To correct for warping inaccuracies, the gray mask was blurred by 3 voxels. This way, alignment inaccuracies were still within the mask. The conclusion is that switching between scanner sites should only be done if proper warping procedures exist.

Subject Specific Anatomic Features

Another issue is the averaging before transformation. For Hyperalignment, empty voxels have to be excluded because they cannot be transfered into common space. Empty voxels mostly result from low coherence values, FOV of the MRI scan or, for anatomical alignment, from different anatomical structure between the subjects' brain. For anatomical alignment averaging phase maps across subjects, these "empty" voxels usually get a value. Hence the phase maps from *anatomical* alignment in Figure 3.6 look smoother then all other maps, even compared to the target-subject's phase map. Phase maps transfered using hyperalignment keep the fine-grained structure of the target-subject's dataset, since there would be no transformation from the empty voxels into the common space. As a result there would be no transformation from the common space into the target-subject's space. Here, this might show sub-optimal alignment but it also shows that hyperalignment keep subject-specific local features — whereas anatomical alignment loses the local subject-specific informations. This is of special interest when it comes to the application at patients: When using anatomical alignment, pathological features may get lost during the averaging process. Hyperalignment is more likely to keep these features. The small holes in the projection are mostly due to the initial intra-subject alignment of the functional data to its anatomy and the transformation from the functional volumes to the surface. There is room for improvement: aligning each subject separately would perhaps improve the result, but the whole processing pipeline was focused on processing many subjects — nearly entirely automatically. Manual single-

subject anatomical alignment would have impaired this idea. The shown result shows the best trade-off between automatic processing and quality.

Resting State as an Alternative?

Comparing with transfer retinotopic maps using resting state data [Gravel et al., 2014; Raemaekers et al., 2014; Arcaro et al., 2015; Striem-Amit et al., 2015] hyperalignment was superior for two major reasons: First, it provided proper polar angle maps as well; using resting state only led to eccentricity maps. Second, the quality of the generated maps was better (more fine-grained). Arcaro et al. [2015] used a small movie clip of 5:45 min but also was not able to generate proper polar angle maps. On these grounds resting state has the potential to generate better eccentricity maps than hyperalignment using the audio movie, but since polar angle maps are also needed for proper visual area definition, this is not an alternative for *i.e.*, hyperalignment using the audio-visual movie. Hyperalignment using the audio-visual movie led to a polar angle and an eccentricity map based on free movie viewing. It needs further experiments to determine how feasible it is with visually impaired patients but it should be a good alternative to conventional retinotopic mapping that relies on center fixation. Striem-Amit et al. [2015] transfered retinotopic maps onto blind subjects' brain using resting state to acquire very rough polar angle (4 sectors) and eccentricity maps. The initial voxel selection is in Talairach group space and that is why it is prone to lose fine-grained informations — which might be of interest in patient examinations. As shown in Figure 3.6 (compare "target" with "anatomical), anatomical alignment leads to smooth maps but loses the subjects' fine spatial informations.

Overall Conclusion

Based on the correlation distances (as shown in Figure3.7 and 3.8) and the quality of the phase maps (*i.e.*, . Figure3.6), it can be said that the transfer of phase maps using hyperalignment works. Using Retinotopic maps works far better and results in much more consistent phase maps compared to using audio-visual movie and audio-movie data. Anatomical alignment gives a comparable intermediate result. Especially Figure3.7 and 3.8 also show, that the overall the subjects had quite similar phase maps– subjects with bad transfer results, *i.e.*, big correlation distances, would have increased the average correlation distance across all subjects.

Hyperalignment is a good basis for group based analysis, since all analysis can be done on the surface of one subject or compared on the surface of each subject, as it is nowadays done via projecting all subjects in *e.g.*, MNI or Talairach space. Hyperalignment is a good alternative to anatomical alignment. The option to use different datasets as a basis to transfer condition between subjects is a big advantage. It gives the possibility to use *e.g.*, movie data to generate phase maps of subjects, who never underwent the retinotopic mapping paradigm. This provides the opportunity to acquire retinotopic presentations of patients

who are unable to properly fixate during a retinotopic mapping task (further discussion in *Application and Outlook* (see 5, p.69)).

It is important to mention that during the progress of this thesis, the developers of the original hyperalignment algorithm introduced the searchlight hyperalignment [Guntupalli et al., 2016], which allows whole brain alignment, too. It uses a completely different approach: aligning the whole brain step-by-step using a searchlight algorithm (see 3.5.2, p.61). The question left open is how much data of each condition are needed to generate good results: is it possible to reduce the number of used volumes (thus scanning time) to get the same or even better results?

### 3.5.2 Comparison with Guntupalli et al., 2016
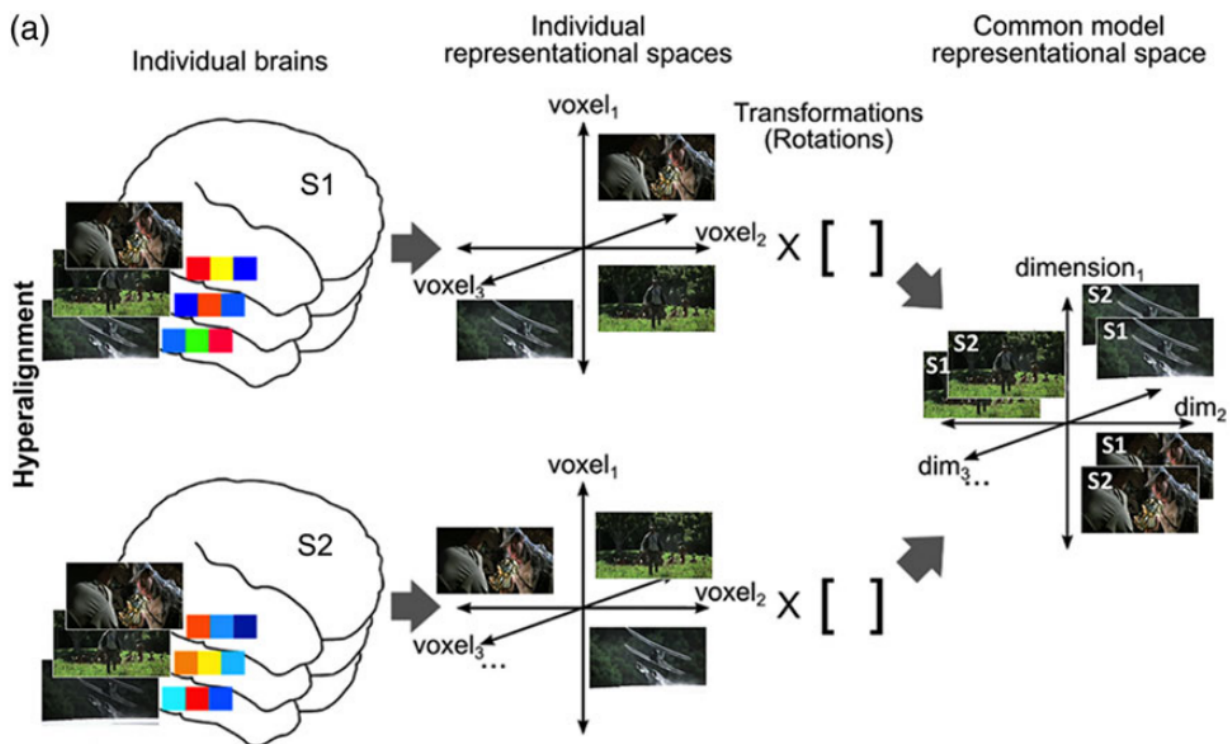
Figure 3.9: "Schematic of whole-cortex searchlight hyperalignment. (a) Hyperalignment aligns neural representational spaces of ROIs in individual subjects' into a common model space of that ROI using rotation in a high-dimensional space. The Procrustes transformation finds the optimal orthogonal transformation matrix to minimize the distances between response vectors for the same movie timepoints in different subjects' representational spaces. An individual subject's transformation matrix rotates that subject's anatomical space into the common space and can be applied to rotate any pattern of activity in that subject's brain into a vector in common space coordinates." Guntupalli et al. [2016, Figure 1]

A paper important to mention here is Guntupalli et al. [2016]. They also used a movie to hyperalign retinotopic mapping data using searchlight hyperalignment (Figure 3.9). Besides using a searchlight algorithm, the differences are:

"Raiders of the Lost Ark" as movie: their anatomical alignment was alignment with MNI

space group-template. As a result their anatomical alignment was worse than the subject-group specific template used for this thesis. They preselected the voxels of each searchlight disc to the top 70 % contributing voxels as well.
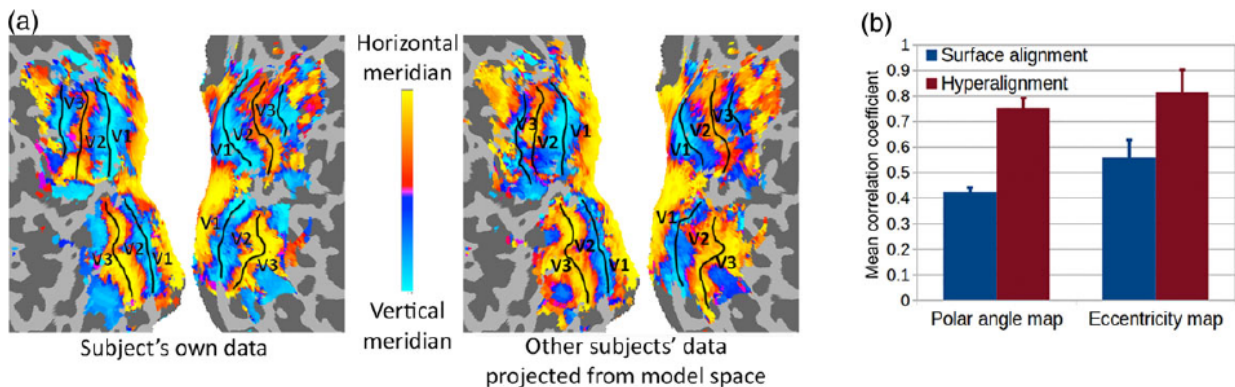

Figure 3.10: "Modeling individual retinotopy maps using the common model. Polar angle and eccentricity maps were estimated in each subject based on corresponding maps of other subjects aligned into the common model derived from the movie data. (a) Polar angle maps in a subject based on that subject's own retinotopy scan and based on others' retinotopy that was rotated into common model dimensions then projected in this subject's cortical anatomy. (b) Mean correlations between the polar angle and eccentricity maps of each subject and maps estimated from other subjects after anatomical alignment (surface alignment using sulcal curvature, blue) and whole-cortex hyperalignment (red). Retinotopic maps based on the common model are significantly better predictors of individual retinotopy than are maps based on anatomical features." Guntupalli et al. [2016, Figure 7]

"The common model-estimated polar angle map is highly similar to the map based on the subject's own retinotopy scan data and preserves the topography enough to draw the boundaries between multiple early visual areas. Figure 3.10 shows the average spatial correlations of the measured maps with the maps estimated based on other subjects' data after hyperalignment (mean correlation for polar angle = 0.75 and eccentricity = 0.81) and after surface-curvature-based alignment (mean correlation for polar angle = 0.42 and eccentricity = 0.56)." [Guntupalli et al., 2016]

That is why their result is in the same range as the results presented here (see Figure 3.5).

3.5.3 Why ROI Selection Is Critical

A major influence is the mask selection and alignment. Since improper ROI alignment leads to patchy phase overlays, possibly with holes. Here the coherence maps maps from the retinotopic mapping were used. This was only possible because the retinotopic mapping data from all participants was available. In case phase maps from retinotopic mapping shall be transfered onto a patient's brain, the coherence map for the patients is probably not available. To solve this, one solution could be to use standard masks from the MNI space

and transform them subject-wise for all subjects with the aim to use these maps, instead of the coherence maps. Another solution could be to anatomically coregister the patient's brain to the average control-subjects' brain and transfer an average control-subjects' coherence mask onto the patient's brain. Besides this, selecting inappropriate areas probably leads to worse hyperalignment results. The preselection of voxels is critical to limit the number of used voxels since whole brain data matrix becomes too big for generating the transformation matrix. The transformation matrix has to be created within the ROI which should be projected, too. Additionally better ROI's voxel match the position of the transfered voxels location more accurately, give a better representation of the projection voxels, which are supposed to be in the same location. This is crucial when aligning a Connectome. Here, the transformation matrix is generated by using the connectivity between the spheres across the brain and the ROI's voxel.

3.5.4 Outlook

3.5.4.1 Improving the Connectome-Hyperalignment

The results from the hyperalignment are already better than in Guntupalli et al. [2016], but there is room for further improvement. Issues to test would be the usage of smaller and therefore more spheres to generate the Connectome. This should give a finer-grained resolution of the subjects' activity patterns. The resulting transformation matrix would eventually be more specific. The limit used was primarily given by the capacity of the computational cluster used. Using the searchlight hyperalignment would also be an option to get whole brain coverage without using one huge matrix. The voxels' contributing to the sphere mean could be preselected, too. The generation of the Connectome itself has also space for tweaking: here correlation distance was used. Different other methods (*e.g.*, covariance, difference, product) to quantify the relationship between two matrices would be a possible option to use in order to generate the Connectome.

3.5.4.2 Preselection of Voxels

The selection of voxels used to generate the initial transformation matrix is crucial. As the usage of all available brain's voxel would generate too big matrices (around 60-90k voxels), restriction is needed. Because of that the first restriction is the usage of gray matter masks. Dilation of the preselective ROI (here gray matter mask) allowed balancing of bigger distortions by warped bold images. The usage of both 7T and 3T especially lead to problems according the coregistration of differently warped bold images from different magnetic fields *i.e.*, different magnetic field strengths. The usage of a surface searchlight based Hyperalignment would be the next step for a whole brain hyperalignment [Guntupalli et al., 2016]. An additional restriction was the limitation onto a ROI of the visual area aimed to be transfered. Transferring the whole brain or all gray matter voxels lead to very long processing times or even too big datasets. It is important to mention that only voxels which

are in the initial training dataset can be projected or hyperaligned. This is a big restriction, since it needs a priori information which areas are interesting for further analysis / between subjects comparison. Due to limited processing power by the used cluster, aligning the whole brain of all participants and look for significant activity everywhere is not possible at the moment. Besides the fact that "an" ROI is needed, this ROI needs to be defined.

3.5.4.3   Rerun With More Subjects

It is possible to keep a stem of subjects and just add subjects by generating transformation matrices for them without changing the common space of all others. The major factor is that the "quality" core subjects, here the ones used to generate the initial common space, need to be similar to the other core subjects. If one subject significantly reduces the overall quality by being to different from the rest, it should not influence the common space. Instead, it should "just" obtain its own transformation matrix to project into the common space. A validation would be to generate a transformation matrix without every subject and see how the quality of the transfered phase map differs, in regards to the correlation distance between target's phase map and transfered phase map.

Chapter 4

General Discussion

Chapter *Visual Pathway Abnormality* showed that there is a basic organization principle of the visual field representation, even with atypical crossing of the optic chiasm. Therefore it would be expected to be able to execute this principle in patients with visual impairment. On these grounds the usage of visual field maps as retinotopic maps would be a possible entry point to validate changes in visual field representations among patients with visual field defects. Accordingly hyperalignment could be used to transfer retinotopic maps for visual field evaluation, but this needs further investigation. An objective measurement method is important, especially to validate methods influencing visual field representations, particular with the upcoming therapeutic methods [Davidson and McCray, 2011; Ali et al., 2000] for visual field recovery.

"In the case of any treatment, however, it would be valuable to use fMRI (and potentially other MR methods) to provide visual cortical biomarkers of treatment outcome." [Brown et al., 2016]

"If differences in connective field parameters between stimulus-driven and resting-state conditions prove local to cortical regions representing the stimulated visual field, these differences may provide a method for mapping cortical regions with residual visual field function in cognitively impaired individuals with cortical visual impairment. Although collecting MR data in these individuals will generally require sedation, many undergo MR scans for medical reasons. Traditional perimetry tests are often impossible in these individuals, so estimating regions of spared vision is done on the basis of spontaneous behavioral responses, which is difficult and imprecise. Because caregivers are instructed to present items of interest in the spared visual field, an improved ability to estimate spared regions would have clinical value." [Bock et al., 2015]

4.1 Traveling Wave Based Retinotopic Mapping

4.1.1 Limits by Dependency on Fixation

Chapter *Visual Pathway Abnormality* showed that retinotopic mapping is possible with visually impaired and compliant participants. Conventional retinotopic mapping is based on proper fixation of the participants. Time and place of stimulation have to be distinct. As a result improper fixation leads to irregular or shifted phase maps. Patients with foveal FOV defects often develop an Preferred Retinal Locus (PRL) [Crossland et al., 2005] or are not able to fixate properly. To overcome this issue, projecting phase maps via Hyperalignment is an option. This way a stimulus which is fixation independent could be used to obtain phase maps from patients with a PRL. The independence from fixation would also be much bigger using auditory stimuli, *e.g.*, the Forrest Gump audio movie, even if the eye movement pattern for *e.g.*, macula degeneration patients is different.

4.1.2 Why not pRF

A pilot study showed that (stripe) artifacts due to projector artifacts have a big impact on pRF sizes but less on standard traveling wave based retinotopic mapping. The issue was the sensitivity to a projector artifact at the 7T Siemens and 3T VERIO setup. Because the same projector type was used, both setups caused shadow artifacts on the stimulus. It is barely visible, but it seems to influence the resulting pRF-sizes by making them bigger. Additionally this kind of mapping is not supported by the AFNI retinotopic toolbox. Also the major pRF toolbox [Dumoulin and Wandell, 2008] is MATLAB based, depending on commercial licensing.

4.2 The Major Processing Pipeline

This thesis contains many processing steps: alignment, preprocessing, data analysis, and data presentation. There are plenty of processing pipelines for most of the analysis parts of this thesis, but there is no toolbox directly containing all tools needed. Hence, the toolbox used should be able to work with different toolboxes of different vendors, *i.e.*, freesurfer, fsl, AFNI, and Python. Since all of these tools can be mostly handled via the terminal, writing a general bash-pipeline would have been possible. But this comes with certain restrictions and hence I used Nipype [Gorgolewski et al., 2011] – but why?

An advantage of *Nipype* is that only processing steps are rerun if their input or their code changes. This way, testing of different parameters can be performed quickly and with the minimum amount of recomputing. Many functions of *freesurfer* and *fsl* are already included in *Nipype*. For not missing functions it is easy to write own function-nodes. The retinotopy workflow itself is a sub-workflow of the hyperalignment pipeline and is used whenever retinotopy data are included. If only small and few datasets need to be analyzed,

the effort-cost to learn these two technologies is too high. A disadvantage is the need to get deeper into the used tools than if using them directly as their tutorials suppose. Bug fixing with *Nipype* often needs the deeper understanding which parameters are allowed, necessary or overwrite other parameters. The documentation and the nodes to the functions, as *bbregister* or *flirt* etc. get better but still bug fixing a *Nipype* pipeline can lead to a lot of work since the layer of the written pipeline, the class of the node, and the referenced function need to be deeply understood; errors can exist on all of these layers. It is important to note that an increasing number of tried-and-true, tested pipelines can be downloaded from the *Nipype* web page. Also, the neurostars forum can be helpful `https://neurostars.org/`.

4.2.1 Which Retinotopic Mapping Software Package

For retinotopic mapping there are different toolboxes available. Next to MATLAB with Vistasoft [Dougherty, 2010] and the AFNI package [Cox, 1996], there are other big software packages or suites capable of retinotopic mapping analysis: Freesurfer with FsFast [`https://surfer.nmr.mgh.harvard.edu/fswiki/FsFastIndividualRetinotopyAnalysis` [Dale et al., 1999]] and Brainvoyager (commercial software [`http://www.brainvoyager.com/pricelist_overview.htm`]).

For Chapter *Visual Pathway Abnormality* mrVista package and for Chapter *Functional Alignment: Hyperalignment* AFNI were used. The major aim for Chapter *Visual Pathway Abnormality* was to gain a retinotopic mapping based comparison and validation, for visual field representations with albinism and achiasma.

Chapter *Functional Alignment: Hyperalignment* focused on the extension of analysis methods to examination of atypical visual fields and their cortical representation using the approach via hyperalignment [Haxby et al., 2011]. The dependence on commercial licences would hinder the distribution and progress for this part. Also parallel processing with MATLAB needs a high number of licences for the used toolboxes.

The resulting retinotopic mapping processing pipeline from Chapter *Functional Alignment: Hyperalignment* is included in the second dataset release [Sengupta et al., 2016](shared first-authorship). This offers a completely working tool to reproduce contributed phase maps from the data given in the released dataset.

Chapter 5

Application and Outlook

As mentioned in part *General Discussion*, hyperalignment could be used for objective retinotopic mapping of visual impaired, and also using different stimuli as training datasets. Accordingly it could be possible to transfer not only the phase maps from subject to subject, as different functional localizer data or activation pattern, too This should depend on the ROI transfered. Besides visual areas, audio or motor area localizers could be transfered. Ideally, one complex stimulus is possible to be used as a training dataset for all transfered localizers. The initial idea was to use the audio-movie to generate transformation matrices to transfer retinotopic phase maps — and thus being able to obtain the cortical visual field representations for visual impaired. This did not work as intended, but it did provide insight about the capabilities of hyperalignment: *i.e.*, the usage of audio-visual movie data led to good results. This stimulus is less fixation dependent and therefore would be able to be used with visual impaired to acquire their visual field representations: Since the subjects phase maps are quite similar (see 3.5.1) the resulting average phase map could be used as a reference map to transfer onto patient brains to achieve that. But further experiments are needed.

This leads to the connection to Chapter *Visual Pathway Abnormality*: the visual field representations under the influence of an atypical optic chiasm, as in albinism and achiasma. Using hyperalignment with movie data achieved from these groups would give further insight into the capabilities of hyperalignment to transfer alternative visual field representations. As shown in [**Kaule** et al., 2014], the retinotopy and structure of the (higher) visual areas can give an insight about the hard-wired and soft-wired structural organization of the human visual cortex. I.e. retinotopic mapping shows which areas are affected by which visual pathway abnormalities and which are not, therefore which anatomical structure of the human brain forms the structure of which cortical (visual) area.

Further analyses, comparing the already collected audio data and audio data with albinism participants, would be necessary before using hyperalignment for a clinical application. A side-note here about the hearing in albinism:

"Albino mammals are not hearing impaired, per se. The auditory and visual deficits in albino mammals are connected in that similar anomalies are present in processing the highest-level integration of spatial localization" [Creel et al., 1995].

This could be of interest if audio data should be used to generate the standard mapper dataset which is in common with the standard participants for hyperalignment. Since audio processing might not be completely the same for albinism and controls, this could hinder the usage of a pure audio stimulus to project the atypical phase map representations.

In general, hyperalignment could give an objective tool to validate visual field representations of visual impaired, or it could be used to gain the localization of certain brain areas before brain surgeries. In the ideal case with a simple localizer can be run with the patient. This localizer could be used as a training dataset and as a result, to transform different kinds of other localizers from a pool of localizer experiments onto the patients brain. Hyperalignment also seems to be superior to anatomical alignment because it keeps subject-specific (pathological) features, while anatomical alignment loses these information (see Figure 3.6: difference of target vs. anatomical). Further testing non-vision stimuli to project visual conditions is needed. Also, the testing with participants with changes in the visual system is needed to verify the outcome of the hyperaligned projections, *i.e.*, the comparison of original target-subject's phase maps with transfered phase maps in participants with changed visual systems.

Chapter 6

Summary

Congenital malformations of the optic chiasm, such as enhanced and reduced crossing of the optic nerve fibers, are evident in albinism and achiasma, respectively: In early visual cortex the resulting additional visual input from the ipsilateral visual hemifield is superimposed onto the normal retinotopic representation of the contralateral visual field, which is likely due to conservative geniculo-striate projections. Counter-intuitively, this organization in early visual cortex does not have profound consequences on visual function. In albinism and achiasma, the mirror-symmetrical superposition of the ipsilateral and contralateral visual fields was evident not only in early visual cortex, but also in the higher areas of the ventral processing stream. Specifically, in the visual areas VO1/2 and PHC1/2 no differences in the extent, the degree of superposition, nor the magnitude of the responses were evident in comparison to the early visual areas. Consequently, the highly atypical organization of the primary visual cortex was propagated downstream to highly specialized processing stages in an undiminished and unchanged manner. This indicates largely unaltered cortico-cortical connections in both types of misrouting, *i.e.*, enhanced and reduced crossing of the optic nerves. It is concluded that main aspects of visual function are preserved despite sizable representation abnormalities in the ventral visual processing stream.

To establish a new technique of visual field testing, functional alignment (Hyperalignment) was introduced. It was shown that using functional alignment could be a viable option to gather visual field maps. Due to its flexibility, it could be applied using a audio-visual movie as a basis to obtain visual filed maps transfered between subjects' brain. Using a (audio-)movie as a stimulus also makes it less fixation-dependent and easier to maintain with elderly or visual impaired patients — compared to standard retinotopic mapping paradigms or clinical tests which rely on the subject fixating screens or objects and asking for feedback about perception of those.

Chapter 7

Zusammenfassung

Der experimentelle Teil eins (Visual Pathway Abnormality) behandelt als zentrales Thema die Auswirkung von atypischen Sehnervenkreuzungen, bei Albinismus und Achiasmie, und deren Auswirkungen auf die Repräsentation des Gesichtsfeldes im visuellen Kortex. Dazu wurden Kontrollprobanden, Probanden mit Albinismus und ein Proband mit Achiasmie mittels fMRT gemessen.

Angeborene Veränderungen der Sehnervenkreuzung, wie zum Beispiel verstärktes oder reduziertes Kreuzen der Sehnerven, liegen entsprechend in Albinismus und Achiasmie vor. In den frühen visuellen Arealen überlagert der daraus resultierende zusätzliche visuelle Input vom ipsilateralen Gesichtsfeld die normale retinotope Repräsentation des kontralateralen Gesichtsfeldes. Dies liegt wahrscheinlich an der konservativen genikulo-striaten Projektion. Kontraintuitiv ist hierbei, dass diese Organisationsweise der frühen visuellen Areale keine profunden Konsequenzen für die visuellen Funktionen hat. In Albinismus und Achiasmie konnte gezeigt werden, dass die spiegel-symmetrische Überlagerung des kontra- und ipsilateralen Gesichtsfeldes sich nicht nur in den frühen visuellen Arealen zeigt, sondern auch in den höheren visuellen Arealen des ventralen Verarbeitungsweges. Speziell in den visuellen Arealen des Ventralen Okzipitalen (VO1/2) und Para-Hippocampalen Cortex (PHC1/2) zeigten sich keine Unterschiede zu den frühen visuellen Arealen in Abgrenzung, Grad der Überlagerung oder der Aktivierungsamplituden. Daraus resultiert, dass sich die atypische Organisation des primären visuellen Kortex auch in nachgeschalteten Verarbeitungsareale unverändert fortsetzt. Dies führt zu der Annahme einer überwiegend unveränderten kortiko-kortikalen Verbindung in beiden Typen der Sehnervenkreuzungsveränderung, hier verstärkte und verringerte Kreuzung der Sehnerven. Es lässt sich also folgern, dass die Hauptaspekte der visuellen Funktionen, auch bei erheblicher atypischer Repräsentation im ventralen Verarbeitungsweg, konserviert bleiben.

Der experimentelle Teil zwei (Functional Alignment: Hyperalignment) behandelt als zentrales Thema eine Technik des funktionellen Alignments, genannt Hyperalignment, und dessen Anwendung zum Transfer von Gesichtsfeldkarten zwischen Probanden bzw. Patienten: Um eine neue Technik zur Gesichtsfeldtestung anzuführen wurde funktionelles Alignment (Hyperalignment) eingeführt.

Zur Untersuchung der Einsetzbarkeit des Hyperalignment wurden fMRT-Daten von gesunden Probanden genutzt. Es wurde gezeigt, dass funktionelles Alignment eine realisierbare Option ist um Gesichtsfeldkarten zu transferieren. Da diese Technik sehr flexibel einsetzbar ist, könnten zum Beispiel audio-visuelle Filme als Basis genutzt werden um Gesichtsfeldkarten zwischen Probandengehirnen zu transferieren. Standard Retinotopie-Kartierungsparadigmen und aktuell benutzte klinische Tests sind angewiesen auf das Patientenfeedback und die richtige Fixation des Bildschirms: (Audio-)Visuelle Filme bieten dagegen den Vorteil weniger fixationsabhängig und einfacher durchführbar zu sein, speziell bei älteren oder sehbehinderten Patienten.

Bibliography

Al-Araimi, M., Pal, B., Poulter, J., van Genderen, M., Carr, I., Cudrnak, T., Brown, L., Sheridan, E., Mohamed, M., Bradbury, J., Ali, M., Inglehearn, C., and Toomes, C. (2013). A new recessively inherited disorder composed of foveal hypoplasia, optic nerve decussation defects and anterior segment dysgenesis maps to chromosome 16q23.3-24.1. *Molecular Vision*, 19:2165–2172. cited By 5.

Ali, R. R., Sarra, G. M., Stephens, C., Alwis, M. D., Bainbridge, J. W., Munro, P. M., Fauser, S., Reichel, M. B., Kinnon, C., Hunt, D. M., Bhattacharya, S. S., and Thrasher, A. J. (2000). Restoration of photoreceptor ultrastructure and function in retinal degeneration slow mice by gene therapy. *Nat Genet*, 25(3):306–310.

Apkarian, P., Bour, L., Barth, P., Wenniger-Prick, L., and Verbeeten, B. (1995). Non-decussating retinal-fugal fibre syndrome an inborn achiasmatic malformation associated with visuotopic misrouting, visual evoked potential ipsilateral asymmetry and nystagmus. *Brain*, 118(5):1195–1216.

Apkarian, P., Bour, L., and Barth, P. G. (1994). A unique achiasmatic anomaly detected in non-albinos with misrouted retinal-fugal projections. *European Journal of Neuroscience*, 6(3):501–507.

Apkarian, P., Reits, D., Spekreijse, H., and Van Dorp, D. (1983). A decisive electrophysiological test for human albinism. *Electroencephalography and clinical neurophysiology*, 55(5):513–531.

Arcaro, M. J., Honey, C. J., Mruczek, R. E., Kastner, S., and Hasson, U. (2015). Widespread correlation patterns of fmri signal across visual cortex reflect eccentricity organization. *eLife*, 4:e03952.

Arcaro, M. J., McMains, S. A., Singer, B. D., and Kastner, S. (2009). Retinotopic organization of human ventral visual cortex. *The Journal of Neuroscience*, 29(34):10638–10652.

Audacity developers (2012). Audacity (Version 2.0.1) [computer program]. `http://audacity.sourceforge.net`. Retrieved from the Debian archive at version 2.0.1-1.

Bao, P., Purington, C. J., and Tjan, B. S. (2015). Using an achiasmic human visual system to quantify the relationship between the fmri bold signal and neural response. *Elife*, 4.

Baseler, H. A., Gouws, A., Haak, K. V., Racey, C., Crossland, M. D., Tufail, A., Rubin, G. S., Cornelissen, F. W., and Morland, A. B. (2011). Large-scale remapping of visual cortex is absent in adult humans with macular degeneration. *Nature neuroscience*, 14(5):649–655.

Benson, N., Butt, O., Datta, R., Radoeva, P., Brainard, D., and Aguirre, G. (2012). The retinotopic organization of striate cortex is well predicted by surface topology. *Current Biology*, 22(21):2081–2085.

Benson, N. C., Butt, O. H., Brainard, D. H., and Aguirre, G. K. (2014). Correction of distortion in flattened representations of the cortical surface allows prediction of v1-V3 Functional organization from anatomy. *PLoS Comput Biol*, 10(3):e1003538.

Berens, P. (2009). Circstat: A matlab toolbox for circular statistics. *Journal of Statistical Software*.

Bock, A. S., Binda, P., Benson, N. C., Bridge, H., Watkins, K. E., and Fine, I. (2015). Resting-state retinotopic organization in the absence of retinal input and visual experience. *The Journal of Neuroscience*, 35(36):12366–12382.

Bressler, D. W. and Silver, M. A. (2010). Spatial attention improves reliability of fmri retinotopic mapping signals in occipital and parietal cortex. *Neuroimage*, 53(2):526–533.

Brewer, A. A., Liu, J., Wade, A. R., and Wandell, B. A. (2005). Visual field maps and stimulus selectivity in human ventral occipital cortex. *Nature neuroscience*, 8(8):1102–1109.

Bridge, H., von dem Hagen, E. A., Davies, G., Chambers, C., Gouws, A., Hoffmann, M., and Morland, A. (2014). Changes in brain morphology in albinism reflect reduced visual acuity. *Cortex*, 56:64–72.

Brown, H. D. H., Woodall, R. L., Kitching, R. E., Baseler, H. A., and Morland, A. B. (2016). Using magnetic resonance imaging to assess visual deficits: a review. *Ophthalmic and Physiological Optics*, 36(3):240–265.

Coalson, J. (2007). Free Lossless Audio Codec (version 1.2.1) [computer program]. `http://flac.sourceforge.net`. Retrieved from the Debian archive at version 1.2.1-6.

Cooper, M. L. and Blasdel, G. G. (1980). Regional variation in the representation of the visual field in the visual cortex of the siamese cat. *Journal of Comparative Neurology*, 193(1):237–253.

Cox, R. W. (1996). AFNI: Software for analysis and visualization of functional magnetic resonance neuroimages. *Computers and Biomedical Research*, 29(3):162–173.

Creel, D., Conlee, J. W., and Parks, T. N. (1995). Auditory brainstem anomalies in albino cats. i. evoked potential studies. *Brain Res*, 260(1):1–9.

Creel, D., Spekreijse, H., and Reits, D. (1981). Evoked potentials in albinos: efficacy of pattern stimuli in detecting misrouted optic fibers. *Electroencephalography and clinical neurophysiology*, 52(6):595–603.

Crossland, M., Culham, L., Kabanarou, S., and Rubin, G. (2005). Preferred retinal locus development in patients with macular disease. *Ophthalmology*, 112(9):1579–1585. cited By 110.

Dale, A., Fischl, B., and Sereno, M. (1999). Cortical surface-based analysis. i. segmentation and surface reconstruction. *Neuroimage*, 9:179–194.

Davidson, B. L. and McCray, Jr, P. B. (2011). Current prospects for rna interference-based therapies. *Nat Rev Genet*, 12(5):329–340.

Davies-Thompson, J., Scheel, M., Lanyon, L. J., and Barton, J. J. S. (2013). Functional organisation of visual pathways in a patient with no optic chiasm. *Neuropsychologia*, 51(7):1260–1272.

DeYoe, E. A., Carman, G. J., Bandettini, P., Glickman, S., Wieser, J., Cox, R., Miller, D., and Neitz, J. (1996). Mapping striate and extrastriate visual areas in human cerebral cortex. *Proceedings of the National Academy of Sciences*, 93(6):2382–2386.

Dougherty, B. (2010). Vistasoft.

Dougherty, R. F., Koch, V. M., Brewer, A. A., Fischer, B., Modersitzki, J., and Wandell, B. A. (2003). Visual field representations and locations of visual areas v1/2/3 in human visual cortex. *Journal of Vision*, 3(10):1.

Downing, P. E., Jiang, Y., Shuman, M., and Kanwisher, N. (2001). A cortical area selective for visual processing of the human body. *Science*, 293(5539):2470–2473.

Dubois, J. and Adolphs, R. (2016). Building a science of individual differences from fmri. *Trends in cognitive sciences*, 20(6):425–443.

Dumoulin, S. O. and Wandell, B. A. (2008). Population receptive field estimates in human visual cortex. *Neuroimage*, 39(2):647–660.

Eglen, S., Marwick, B., Halchenko, Y., Hanke, M., Sufi, S., Gleeson, P., Silver, R. A., Davison, A., Lanyon, L., Abrams, M., et al. (2016). Towards standard practices for sharing computer code and programs in neuroscience. *bioRxiv*, page 045104.

Elekessy, E. I., Campion, J. E., and Henry, G. H. (1973). Differences between the visual fields of siamese and common cats. *Vision research*, 13(12):2533–IN11.

Engel, S. A., Glover, G. H., and Wandell, B. A. (1997). Retinotopic organization in human visual cortex and the spatial precision of functional mri. *Cerebral cortex*, 7(2):181–192.

Engel, S. A., Rumelhart, D. E., Wandell, B. A., Lee, A. T., Glover, G. H., Chichilnisky, E.-J., and Shadlen, M. N. (1994). fmri of human visual cortex. *Nature*.

Epstein, R. and Kanwisher, N. (1998). A cortical representation of the local visual environment. *Nature*, 392(6676):598–601.

Felleman, D. J. and Van Essen, D. C. (1987). Receptive field properties of neurons in area v3 of macaque monkey extrastriate cortex. *Journal of Neurophysiology*, 57(4):889–920.

Garipis, N. and Hoffmann, K.-P. (2003). Visual field defects in albino ferrets (mustela putorius furo). *Vision research*, 43(7):793–800.

Gattass, R., Sousa, A., and Gross, C. (1988). Visuotopic organization and extent of v3 and v4 of the macaque. *The Journal of neuroscience*, 8(6):1831–1845.

Gorgolewski, K., Burns, C. D., Madison, C., Clark, D., Halchenko, Y. O., Waskom, M. L., and Ghosh, S. S. (2011). Nipype: a flexible, lightweight and extensible neuroimaging data processing framework in Python. *Frontiers in Neuroinformatics*, 5(13).

Gorgolewski, K. J., Auer, T., Calhoun, V. D., Craddock, R. C., Das, S., Duff, E. P., Flandin, G., Ghosh, S. S., Glatard, T., Halchenko, Y. O., Handwerker, D. A., Hanke, M., Keator, D., Li, X., Michael, Z., Maumet, C., Nichols, B. N., Nichols, T. E., Poline, J.-B., Rokem, A., Schaefer, G., Sochat, V., Turner, J. A., Varoquaux, G., and Poldrack, R. A. (2016). The brain imaging data structure: a standard for organizing and describing outputs of neuroimaging experiments. *Scientific Data*.

Gravel, N., Harvey, B., Nordhjem, B., Haak, K. V., Dumoulin, S. O., Renken, R., Ćurčić-Blake, B., and Cornelissen, F. W. (2014). Cortical connective field estimates from resting state fmri activity. *Frontiers in neuroscience*, 8:339.

Guillery, R. (1986). Neural abnormalities of albinos. *Trends in neurosciences*, 9:364–367.

Guillery, R., Hickey, T., Kaas, J., Felleman, D., Debruyn, E., and Sparks, D. L. (1984). Abnormal central visual pathways in the brain of an albino green monkey (cercopithecus aethiops). *Journal of Comparative Neurology*, 226(2):165–183.

Guntupalli, J. S., Hanke, M., Halchenko, Y. O., Connolly, A. C., Ramadge, P. J., and Haxby, J. V. (2016). A model of representational spaces in human cortex. *Cerebral Cortex*, page bhw068.

Halchenko, Y. O. and Hanke, M. (2012). Open is not enough. Let's take the next step: An integrated, community-driven computing platform for neuroscience. *Frontiers in Neuroinformatics*, 6(00022).

Halchenko, Y. O. and Hanke, M. (2015). Four aspects to make science open "by design" and not as an after-thought. *GigaScience*, 4(1):1–4.

Handbreak team (2012). Handbreak (version 0.9.8) [computer program]. `http://handbrake.fr`. Retrieved from `http://www.deb-multimedia.org` at version 0.9.8+git20121007-dmo5.

Hanke, M., Adelhöfer, N., Kottke, D., Iacovella, V., Sengupta, A., **Kaule**, F. R., Nigbur, R., Waite, A. Q., Baumgartner, F. J., and Stadler, J. (2016). A studyforrest extension, simultaneous fMRI and eye gaze recordings during prolonged natural stimulation. *Scientific Data*, 3.

Hanke, M., Baumgartner, F. J., Ibe, P., **Kaule**, F. R., Pollmann, S., Speck, O., Zinke, W., and Stadler, J. (2014). A high-resolution 7-Tesla fmri dataset from complex natural stimulation with an audio movie. *Scientific Data*, 1.

Hanke, M., Dinga, R., Häusler, C., Guntupalli, J., Casey, M., **Kaule**, F., and Stadler, J. (2015). High-resolution 7-tesla fmri data on the perception of musical genres - an extension to the studyforrest dataset [version 1; referees: 2 approved with reservations]. *F1000Research*, 4(174).

Hanke, M., Halchenko, Y. O., Sederberg, P. B., Olivetti, E., Fründ, I., Rieger, J. W., Herrmann, C. S., Haxby, J. V., Hanson, S. J., and Pollmann, S. (2009). PyMVPA: A unifying approach to the analysis of neuroscientific data. *Frontiers in Neuroinformatics*, 3(3). PMC2638552.

Haxby, J., Guntupalli, J., Connolly, A., Halchenko, Y., Conroy, B., Gobbini, M., Hanke, M., and Ramadge, P. (2011). A common, high-dimensional model of the representational space in human ventral temporal cortex. *Neuron*, 72(2):404–416.

Haxby, J. V. (2012). Multivariate pattern analysis of fmri: The early beginnings. *NeuroImage*, 62(2):852–855.

Henriksson, L., Karvonen, J., Salminen-Vaparanta, N., Railo, H., and Vanni, S. (2012). Retinotopic maps, spatial tuning, and locations of human visual areas in surface coordinates characterized with multifocal and blocked fmri designs. *PLoS ONE*, 7(5):e36859.

Hertle, R. W., Dell'Osso, L. F., FitzGibbon, E. J., Caruso, R. C., Butman, J. A., Yang, D., and Mellow, S. D. (2001). Clinical, radiographic, and electrophysiologic findings in patients with achiasma or hypochiasma. *Neuro-Ophthalmology*, 26(1):43–57.

Hoffmann, M., Schmidtborn, L., and Morland, A. (2007a). Abnormale repräsentationen im visuellen kortex von albinismus-patienten. *Der Ophthalmologe*, 104(8):666–673.

Hoffmann, M., **Kaule**, F., Grzeschik, R., Behrens-Baumann, W., and Wolynski, B. (2011). Retinotope kartierung des menschlichen visuellen kortex mit funktioneller magnetresonanztomographie - grundlagen, aktuelle entwicklungen & perspektiven für die ophthal-

mologie. (retinotopic mapping of the human visual cortex with functional magnetic resonance imaging - principles, current developments & ophthalmological perspectives). *Klinische Monatsblätter für Augenheilkunde*, 228:613–620.

Hoffmann, M., **Kaule**, F., Levin, N., Masuda, Y., Kumar, A., Gottlob, I., Horiguchi, H., Dougherty, R., Stadler, J., Wolynski, B., and et al. (2012). Plasticity and stability of the visual system in human achiasma. *Neuron*, 75(3):393–401.

Hoffmann, M. B. and Dumoulin, S. O. (2015). Congenital visual pathway abnormalities: a window onto cortical stability and plasticity. *Trends in neurosciences*, 38(1):55–65.

Hoffmann, M. B., Lorenz, B., Morland, A. B., and Schmidtborn, L. C. (2005). Misrouting of the optic nerves in albinism: estimation of the extent with visual evoked potentials. *Investigative ophthalmology & visual science*, 46(10):3892–3898.

Hoffmann, M. B., Seufert, P. S., and Schmidtborn, L. C. (2007b). Perceptual relevance of abnormal visual field representations: static visual field perimetry in human albinism. *British journal of ophthalmology*, 91(4):509–513.

Hoffmann, M. B., Stadler, J., Kanowski, M., and Speck, O. (2009). Retinotopic mapping of the human visual cortex at a magnetic field strength of 7t. *Clinical Neurophysiology*, 120(1):108–116.

Hoffmann, M. B., Tolhurst, D. J., Moore, A. T., and Morland, A. B. (2003). Organization of the visual cortex in human albinism. *The Journal of neuroscience*, 23(26):8921–8930.

Hubel, D. H. (1989). *Auge und Gehirn: Neurobiologie des Sehens*. Spektrum-d.-Wiss.-Verlag-Ges.

Jansonius, N. M., van der Vliet, T. A. M., Cornelissen, F. W., Pott, J. W. R., and Kooijman, A. C. (2001). A girl without a chiasm: electrophysiologic and mri evidence for the absence of crossing optic nerve fibers in a girl with a congenital nystagmus. *Journal of neuro-ophthalmology*, 21(1):26–29.

Kanowski, M., Rieger, J. W., Noesselt, T., Tempelmann, C., and Hinrichs, H. (2007). Endoscopic eye tracking system for fmri. *Journal of neuroscience methods*, 160(1):10–15.

Kanwisher, N., McDermott, J., and Chun, M. M. (1997). The fusiform face area: a module in human extrastriate cortex specialized for face perception. *The Journal of Neuroscience*, 17(11):4302–4311.

Klemen, J. and Chambers, C. D. (2012). Current perspectives and methods in studying neural mechanisms of multisensory interactions. *Neuroscience & Biobehavioral Reviews*, 36(1):111–133.

Klemen, J., Hoffmann, M. B., and Chambers, C. D. (2012). Cortical plasticity in the face of congenitally altered input into {V1}. *Cortex*, 48(10):1362 – 1365.

Kolster, H., Peeters, R., and Orban, G. A. (2010). The retinotopic organization of the human middle temporal area mt/v5 and its cortical neighbors. *The Journal of Neuroscience*, 30(29):9801–9820.

Konen, C. S., Behrmann, M., Nishimura, M., and Kastner, S. (2011). The functional neuroanatomy of object agnosia: a case study. *Neuron*, 71(1):49–60.

Konen, C. S. and Kastner, S. (2008). Representation of eye movements and stimulus motion in topographically organized areas of human posterior parietal cortex. *The Journal of Neuroscience*, 28(33):8361–8375.

Korff, C., Apkarian, P., Bour, L., Meuli, R., Verrey, J., and Roulet Perez, E. (2003). Isolated absence of optic chiasm revealed by congenital nystagmus, mri and veps. *Neuropediatrics*, 34(4):219.

Kravitz, D. J., Saleem, K. S., Baker, C. I., Ungerleider, L. G., and Mishkin, M. (2013). The ventral visual pathway: an expanded neural framework for the processing of object quality. *Trends in cognitive sciences*, 17(1):26–49.

Kwong, K. K., Belliveau, J. W., Chesler, D. A., Goldberg, I. E., Weisskoff, R. M., Poncelet, B. P., Kennedy, D. N., Hoppel, B. E., Cohen, M. S., and Turner, R. (1992). Dynamic magnetic resonance imaging of human brain activity during primary sensory stimulation. *Proceedings of the National Academy of Sciences*, 89(12):5675–5679.

Leventhal, A. G. and Creel, D. J. (1985). Retinal projections and functional architecture of cortical areas 17 and 18 in the tyrosinase-negative albino cat. *The Journal of neuroscience*, 5(3):795–807.

Levin, A. V. and Stroh, E. (2011). Albinism for the busy clinician. *Journal of American Association for Pediatric Ophthalmology and Strabismus*, 15(1):59–66.

Levin, N., Dumoulin, S. O., Winawer, J., Dougherty, R. F., and Wandell, B. A. (2010). Cortical maps and white matter tracts following long period of visual deprivation and retinal image restoration. *Neuron*, 65(1):21–31.

Logothetis, N. K. and Wandell, B. A. (2004). Interpreting the bold signal. *Annu. Rev. Physiol.*, 66:735–769.

Maunsell, J. H. and Van Essen, D. C. (1983). Functional properties of neurons in middle temporal visual area of the macaque monkey. i. selectivity for stimulus direction, speed, and orientation. *Journal of neurophysiology*, 49(5):1127–1147.

Muckli, L., Naumer, M. J., and Singer, W. (2009). Bilateral visual field maps in a patient with only one hemisphere. *Proceedings of the National Academy of Sciences*, 106(31):13034–13039.

Nishimoto, S. and Nishida, S. (2016). Lining up brains via a common representational space. *Trends in Cognitive Sciences.*

Ogawa, S., Lee, T.-M., Kay, A. R., and Tank, D. W. (1990). Brain magnetic resonance imaging with contrast dependent on blood oxygenation. *Proceedings of the National Academy of Sciences*, 87(24):9868–9872.

Ogawa, S., Tank, D. W., Menon, R., Ellermann, J. M., Kim, S. G., Merkle, H., and Ugurbil, K. (1992). Intrinsic signal changes accompanying sensory stimulation: functional brain mapping with magnetic resonance imaging. *Proceedings of the National Academy of Sciences*, 89(13):5951–5955.

Peelen, M. V. and Downing, P. E. (2005). Selectivity for the human body in the fusiform gyrus. *Journal of neurophysiology*, 93(1):603–608.

Peirce, J. W. (2007). Psychopy—psychophysics software in python. *Journal of Neuroscience Methods*, 162:8–13.

Poldrack, R. A., Barch, D. M., Mitchell, J., Wager, T., Wagner, A. D., Devlin, J. T., Cumba, C., Koyejo, O., and Milham, M. (2013). Towards open sharing of task-based fmri data: The openfmri project. *Frontiers in Neuroinformatics*, 7(12).

Pomeranz, H. D., Agadzi, A. K., and Eksten, B. (2006). Achiasmia and unilateral optic nerve hypoplasia in an otherwise healthy infant. *Acta Ophthalmologica Scandinavica*, 84(1):140–144.

Prakash, S., Dumoulin, S., Fischbein, N., Wandell, B. A., and Liao, Y. J. (2010). Congenital achiasma and see-saw nystagmus in vacterl syndrome. *Journal of neuro-ophthalmology: the official journal of the North American Neuro-Ophthalmology Society*, 30(1):45.

Raemaekers, M., Schellekens, W., van Wezel, R. J., Petridou, N., Kristo, G., and Ramsey, N. F. (2014). Patterns of resting state connectivity in human primary visual cortical areas: A 7T fmri study. *NeuroImage*, 84:911–921.

Sami, D., Saunders, D., Thompson, D., Russell-Eggitt, I., Nischal, K., Jeffery, G., Dattani, M., Clement, R., Liassis, A., and Taylor, D. (2005). The achiasmia spectrum: congenitally reduced chiasmal decussation. *British journal of ophthalmology*, 89(10):1311–1317.

Schmolesky, M. T., Wang, Y., Creel, D. J., and Leventhal, A. G. (2000). Abnormal retinotopic organization of the dorsal lateral geniculate nucleus of the tyrosinase-negative albino cat. *Journal of Comparative Neurology*, 427(2):209–219.

Sengupta, A., **Kaule**, F. R., Guntupalli, J. S., Hoffmann, M. B., Häusler, C., Stadler, J., and Hanke, M. (2016). A studyforrest extension, retinotopic mapping and localization of higher visual areas. *Scientific Data*, 3.

Sereno, M., Pitzalis, S., and Martinez, A. (2001). Mapping of contralateral space in retinotopic coordinates by a parietal cortical area in humans. *Science*, 294(5545):1350–1354.

Sereno, M. I., Dale, A., Reppas, J., Kwong, K., Belliveau, J., Brady, T., Rosen, B., and Tootell, R. (1995). Borders of multiple visual areas in humans revealed by functional magnetic resonance imaging. *Science*, 268(5212):889–893.

Sereno, M. I., Lutti, A., Weiskopf, N., and Dick, F. (2012). Mapping the human cortical surface by combining quantitative T1 with retinotopy. *Cerebral Cortex*, 23(9):2261–2268.

Sheremata, S. L. and Silver, M. A. (2015). Hemisphere-dependent attentional modulation of human parietal visual field representations. *The Journal of Neuroscience*, 35(2):508–517.

Shmuel, A., Augath, M., Oeltermann, A., and Logothetis, N. K. (2006). Negative functional mri response correlates with decreases in neuronal activity in monkey visual area v1. *Nature neuroscience*, 9(4):569–577.

Silver, M. A. and Kastner, S. (2009). Topographic maps in human frontal and parietal cortex. *Trends in cognitive sciences*, 13(11):488–495.

Silver, M. A., Ress, D., and Heeger, D. J. (2005). Topographic maps of visual spatial attention in human parietal cortex. *Journal of neurophysiology*, 94(2):1358–1371.

Sinha, P. and Meng, M. (2012). Superimposed hemifields in primary visual cortex of achiasmic individuals. *Neuron*, 75(3):353–355.

Smith, A. T., Singh, K. D., and Greenlee, M. W. (2000). Attentional suppression of activity in the human visual cortex. *Neuroreport*, 11(2):271–278.

Smith, A. T., Williams, A. L., and Singh, K. D. (2004). Negative bold in the visual cortex: evidence against blood stealing. *Human brain mapping*, 21(4):213–220.

Striem-Amit, E., Ovadia-Caro, S., Caramazza, A., Margulies, D. S., Villringer, A., and Amedi, A. (2015). Functional connectivity of visual cortex in the blind follows retinotopic organization principles. *Brain*, page awv083.

Tanabe, S., Doi, T., Umeda, K., and Fujita, I. (2005). Disparity-tuning characteristics of neuronal responses to dynamic random-dot stereograms in macaque visual area v4. *Journal of neurophysiology*, 94(4):2683–2699.

Teo, P. C., Sapiro, G., and Wandell, B. A. (1997). Creating connected representations of cortical gray matter for functional mri visualization. *Medical Imaging, IEEE Transactions on*, 16(6):852–863.

Kaule, F., Wolynski, B., Kumar, A., Gottlob, I., Stadler, J., Speck, O., Kanowski, M., Meltendorf, S., and Hoffmann, M. (2012). Consequences of chiasmatic abnormalities on the organisation of the ventral processing stream. *Perception*, 41(1 suppl):1–269.

Kaule, F. R., Wolynski, B., Gottlob, I., Stadler, J., Speck, O., Kanowski, M., Meltendorf, S., Behrens-Baumann, W., and Hoffmann, M. B. (2014). Impact of chiasma opticum malformations on the organization of the human ventral visual cortex. *Hum. Brain Mapp.*, pages 5093–5105.

Thain, D., Tannenbaum, T., and Livny, M. (2005). Distributed computing in practice: the condor experience. *Concurrency - Practice and Experience*, 17(2-4):323–356.

Tootell, R. B., Mendola, J. D., Hadjikhani, N. K., Liu, A. K., and Dale, A. M. (1998). The representation of the ipsilateral visual field in human cerebral cortex. *Proceedings of the National Academy of Sciences*, 95(3):818–824.

Uludağ, K., Uğurbil, K., and Berliner, L. (2015). *fMRI: From Nuclear Spins to Brain Functions*, volume 30. Springer.

Van de Moortele, P.-F., Auerbach, E. J., Olman, C., Yacoub, E., Uğurbil, K., and Moeller, S. (2009). T 1 weighted brain images at 7 tesla unbiased for proton density, t 2 contrast and rf coil receive b 1 sensitivity with simultaneous vessel visualization. *Neuroimage*, 46(2):432–446.

Van Essen, D. C., Lewis, J. W., Drury, H. A., Hadjikhani, N., Tootell, R. B., Bakircioglu, M., and Miller, M. I. (2001). Mapping visual cortex in monkeys and humans using surface-based atlases. *Vision research*, 41(10):1359–1378.

Victor, J. D., Apkarian, P., Hirsch, J., Conte, M. M., Packard, M., Relkin, N. R., Kim, K. H., and Shapley, R. M. (2000). Visual function and brain organization in non-decussating retinal–fugal fibre syndrome. *Cerebral Cortex*, 10(1):2–22.

Von Dem Hagen, E. A., Houston, G. C., Hoffmann, M. B., and Morland, A. B. (2007). Pigmentation predicts the shift in the line of decussation in humans with albinism. *European Journal of Neuroscience*, 25(2):503–511.

von dem Hagen, E. A. H., Hoffmann, M. B., and Morland, A. B. (2008). Identifying human albinism: A comparison of vep and fmri. *Investigative Ophthalmology & Visual Science*, 49(1):238.

Wade, A. R., Brewer, A. A., Rieger, J. W., and Wandell, B. A. (2002). Functional measurements of human ventral occipital cortex: retinotopy and colour. *Philosophical Transactions of the Royal Society of London. Series B: Biological Sciences*, 357(1424):963–973.

Wandell, B. A., Chial, S., and Backus, B. T. (2000). Visualization and measurement of the cortical surface. *Journal of cognitive neuroscience*, 12(5):739–752.

Wandell, B. A., Dumoulin, S. O., and Brewer, A. A. (2007). Visual field maps in human cortex. *Neuron*, 56(2):366–383.

Wandell, B. A. and Winawer, J. (2015). Computational neuroimaging and population receptive fields. *Trends in cognitive sciences*.

Wang, L., Mruczek, R. E., Arcaro, M. J., and Kastner, S. (2014). Probabilistic maps of visual topography in human cortex. *Cerebral Cortex*, page bhu277.

Warnking, J., Dojat, M., Guérin-Dugué, A., Delon-Martin, C., Olympieff, S., Richard, N., Chéhikian, A., and Segebarth, C. (2002). fmri retinotopic mapping–step by step. *Neuroimage*, 17(4):1665–1683.

Williams, R. W., Hogan, D., and Garraghty, P. E. (1994). Target recognition and visual maps in the thalamus of achiasmatic dogs. *Nature*, 367(6464):637–639.

Winawer, J., Horiguchi, H., Sayres, R. A., Amano, K., and Wandell, B. A. (2010). Mapping hv4 and ventral occipital cortex: the venous eclipse. *Journal of vision*, 10(5):1–1.

Wolynski, B., Kanowski, M., Meltendorf, S., Behrens-Baumann, W., and Hoffmann, M. B. (2010). Self-organisation in the human visual system - visuo-motor processing with congenitally abnormal v1 input. *Neuropsychologia*, 48(13):3834–3845.

Yates, C. and Dennedy, D. (2012). MLT Multimedia Framework (Version 0.8.0) [computer program]. `http://www.mltframework.org`. Retrieved from the Debian archive at version 0.8.0-4.

Zaitsev, M., Hennig, J., and Speck, O. (2004). Point spread function mapping with parallel imaging techniques and high acceleration factors: Fast, robust, and flexible method for echo-planar imaging distortion correction. *Magnetic Resonance in Medicine*, 52(5):1156–1166.

Abbreviations

AFNI	Analysis of Functional NeuroImages
fMRI	functional MRI
FOV	Field Of View
fwhm	full width half maximum
MRI	Magnetic Resonance Imaging
OC	Optic Chiasm
PHC	Para-Hippocampal Cortex
pRF	population Receptive Field
PRL	Preferred Retinal Locus
ROI	Region Of Interest
V1/2/3/3ab/4	Visual areas 1-4
VEP	Visual Evoked Potential
VO	Ventral Occipital (visual cortex)

Appendix
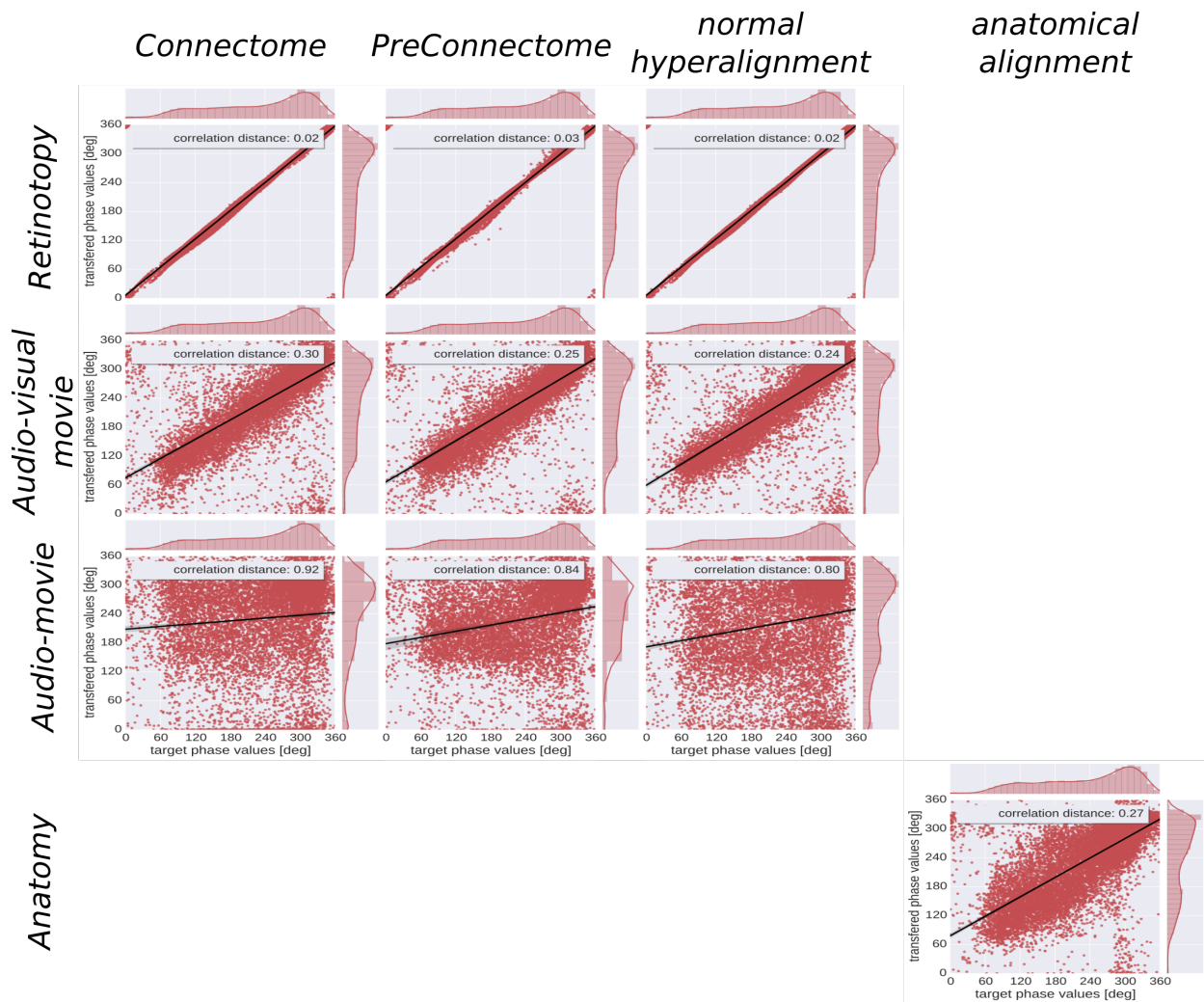
Figure 7.1: Eccentricity phase representations for for different methods and used datasets, as in Figure 3.4, shown also for the left hemisphere. rows: different origins (training datasets) of the transformation matrix; columns: methods used to generate the transformation matrix.
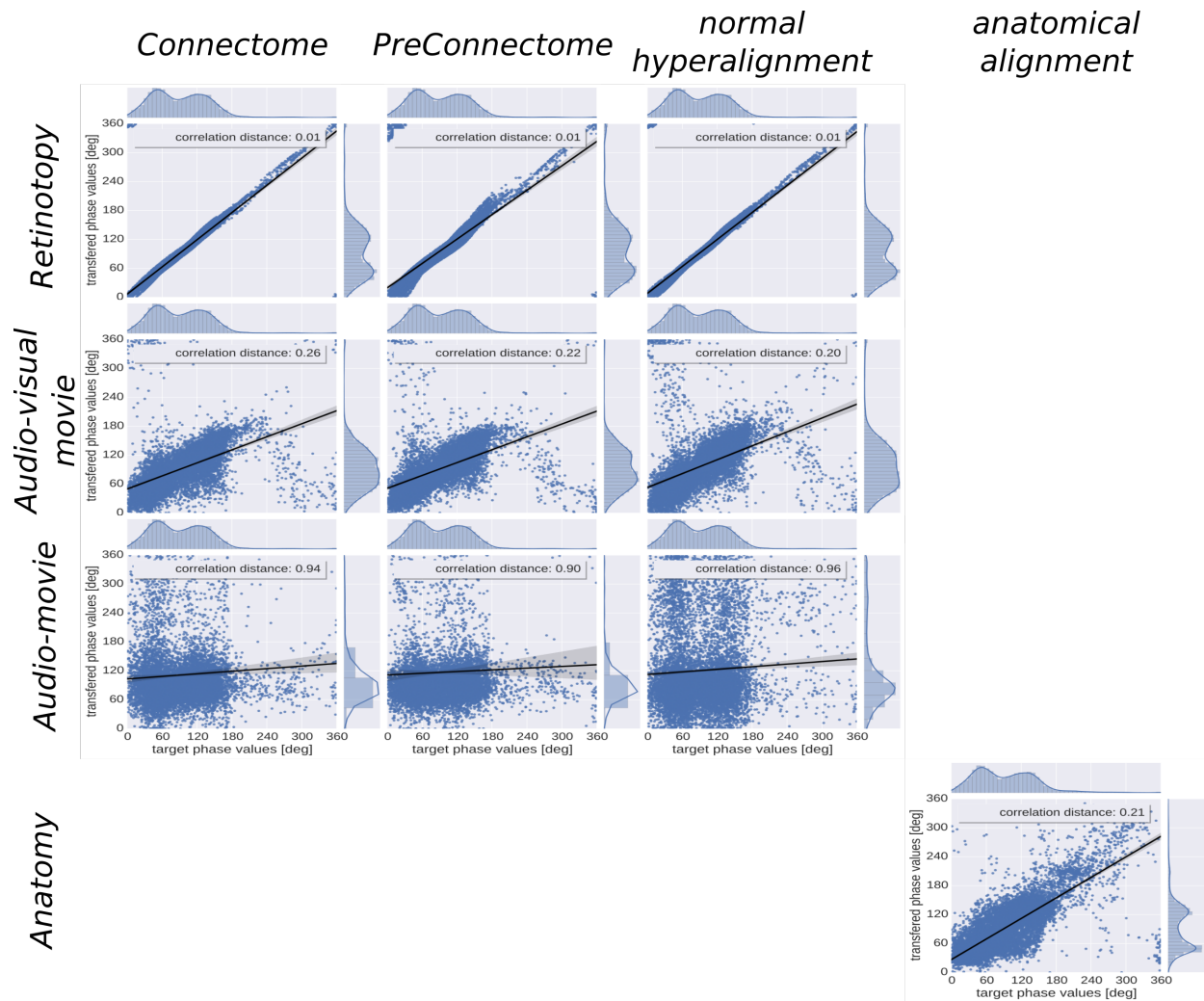
Figure 7.2: Polar angle phase representations for different methods and used datasets, as in Figure 3.4, shown also for the left hemisphere, accordingly polar angle mostly for 180 to 360° (see additionally Figure 3.2B). rows: different origins (training datasets) of the transformation matrix; columns: methods used to generate the transformation matrix.

subj	overall_left	overall_right	lV1 mask fit	lV2/3 mask fit	rV1 mask fit	rV2/3 mask fit	comments	known_issues	left hemisphere	right hemisphere
1	4	5	3	2	3	2			4: PHC2 hole	5
2	3	5	2	2	2	2			3: higher than V3 very patchy	5
3	5	3	3	2	2	2			5	3: PHC very patchy (good in ccw)
4	4	5	3	3	1	2			4: PHC2 hard	5: PHC2 hard (better in ccw)
5	3	4	1	1	2	1			3: small holes, dorsal patchy	4: PHC2 hole
6	4	3	3	3	2	2		FoV (for retmap, objectCat,movieLocalizer,lH	4: Sqaure holes from missing FoV; small holes, clear dorsal boarders	3: many small holes but good boarders
9	2	2	1	1	1	1			2: dorsal smeared: dV3 very hard,vague PHC , small holes	2: ventral smeared, vague PHC
10	4	3	3	2	3	2			4: outer PHC border hard	3: from VO hard (better in ccw)
14	2	3	2	2	1	1			2: very patchy, above V3 hard (ccw helps)	3: no PHC, patchy
15	2	2	2	2	1	2			2: small holes, no PHC covered	2: patchy, holes, hard PHC (clw helps)
16	3	4	3	1	3	2			3: no PHC2, dorsal small holes	4: PHC hard (clw helps)
17	2	3	2	2	3	2	lh: HM quite short		2: no PHC2, hard VO (ccw helps)	3: PHC hard, peripheral holes
18	3	2	3	2	2	3			3: PHC hard (ccw helps)	2: ventral smeared: hard PHC, VO
19	3	5	2	1	2	2			3: no PHC2	5: small holes
20	1	4	2	2	2	2	L: very clear restrition of FoV; Rclw: blue phase missing		1: bad coverage, patchy, holes	4: hard PHC
Avera	3	3.5333333	2.333333		2.5	2.071428571		2		

Range (phasemap quality)

best: 9	1, 4	
age: 7	5, 10, 16	
orst: 4	9, 15	

what checked?		Range (FS ma How it fits borders
pfd, if needed also efd	1	badly; much too big in certain areas
checked for borders: V123, PHC complex	2	approximately
Range (Phasemaps):	3	good
1 (worst) to 5 (best)		

Figure 7.3: Overview on subjects' quality from retinotopic mapping

Publications

Content from papers marked with * is represented in this thesis:

- Sengupta, A., **Kaule**, F. R., Guntupalli, J. S., Hoffmann, M. B., Häusler, C., Stadler, J., and Hanke, M. (2016). A studyforrest extension, retinotopic mapping and localization of higher visual areas. *Scientific Data*, 3,*(shared first-author)***

- Hanke, M., Adelhöfer, N., Kottke, D., Iacovella, V., Sengupta, A., **Kaule**, F. R., Nigbur, R., Waite, A. Q., Baumgartner, F. J., and Stadler, J. (2016). A studyforrest extension, simultaneous fMRI and eye gaze recordings during prolonged natural stimulation. *Scientific Data*, 3***

- Hanke, M., Dinga, R., Häusler, C., Guntupalli, J., Casey, M., **Kaule**, F., and Stadler, J. (2015). High-resolution 7-tesla fmri data on the perception of musical genres - an extension to the studyforrest dataset [version 1; referees: 2 approved with reservations]. *F1000Research*, 4(174)

- **Kaule**, F. R., Wolynski, B., Gottlob, I., Stadler, J., Speck, O., Kanowski, M., Meltendorf, S., Behrens-Baumann, W., and Hoffmann, M. B. (2014). Impact of chiasma opticum malformations on the organization of the human ventral visual cortex. *Hum. Brain Mapp.*, pages 5093–5105***

- Hanke, M., Baumgartner, F. J., Ibe, P., **Kaule**, F. R., Pollmann, S., Speck, O., Zinke, W., and Stadler, J. (2014). A high-resolution 7-Tesla fmri dataset from complex natural stimulation with an audio movie. *Scientific Data*, 1***

- Hoffmann, M., **Kaule**, F., Levin, N., Masuda, Y., Kumar, A., Gottlob, I., Horiguchi, H., Dougherty, R., Stadler, J., Wolynski, B., and et al. (2012). Plasticity and stability of the visual system in human achiasma. *Neuron*, 75(3):393–401

- Hoffmann, M., **Kaule**, F., Grzeschik, R., Behrens-Baumann, W., and Wolynski, B. (2011). Retinotope kartierung des menschlichen visuellen kortex mit funktioneller magnetresonanztomographie - grundlagen, aktuelle entwicklungen & perspektiven für die ophthalmologie. (retinotopic mapping of the human visual cortex with functional magnetic resonance imaging - principles, current developments & ophthalmological perspectives). *Klinische Monatsblätter für Augenheilkunde*, 228:613–620

Acknowledgements

Erklärung

Hiermit erkläre ich, dass ich die von mir eingereichte Dissertation zum dem Thema

Examination of Physiology and Pathophysiology of the Human Visual Cortex using Functional Magnetic Resonance Imaging

selbständig verfasst, nicht schon als Dissertation verwendet habe und die benutzten Hilfsmittel und Quellen vollständig angegeben wurden.

Weiterhin erkläre ich, dass ich weder diese noch eine andere Arbeit zur Erlangung des akademischen Grades doctor rerum naturalium (Dr. rer. nat.) an anderen Einrichtungen eingereicht habe und weiterhin, dass mir die geltende Promotionsordnung (Version vom 19.01.2006) bekannt ist.

Magdeburg,

Dipl.-Neurowiss. Falko R. Kaule